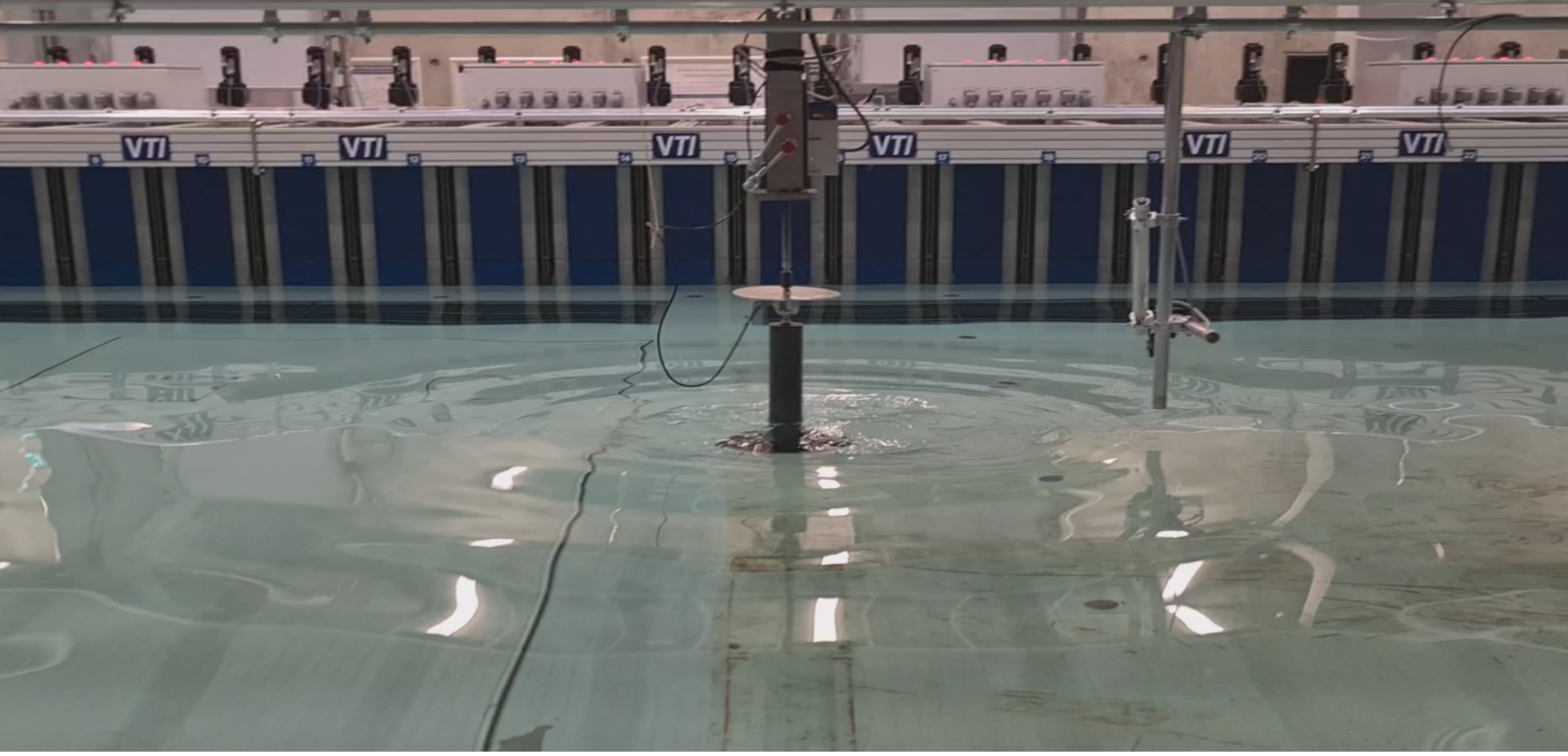

Hydrodynamic Effects of Heave Plates

Hans Lindenchrone Dueholm and Lars Kristensen

Structural and Civil Engineering, 2021-06

Master's Project

AALBORG UNIVERSITY
STUDENT REPORT

Department of Civil Engineering
Thomas Manns Vej 23
9220 Aalborg Øst
http://www.civil.aau.dk

Title:

Hydrodynamic Effects of Heave Plates

Project:

Master's Project

Period:

Oktober 2020 - June 2021

Authors:

Hans Dueholm
Lars Kristensen

Supervisor(s):

Jonas Bjerg Thomsen
Mads Røge Eldrup

Full document: 126 pages
Main paper: 84 pages
Appendix: 31 pages
Finish date: June 10, 2021

Synopsis:

A downsized model of a circular heave plate attached to the bottom of a cylinder is modelled for a variety of oscillatory motions and disc radii, by means of theoretical calculations, Smoothed Particle Hydrodynamcis (SPH) simulations, and physical experiments. The resultant time series of the three models are analysed and the force amplitudes, added mass and drag coefficient are found and used as points of comparison.
From the comparison it is evident that both the theoretical and SPH models do not simulate the hydrodynamics of the heave plate very well. The theoretical calculations does not yield results with consistent margins of error as the parameters of the model is changed. The SPH simulations has large margins of error for the tested cases with lower velocities and smaller heave plates, and in turn smaller margins of error for cases with higher velocities and larger heave plates.
Plausible reasons for the errors of the two models where discussed and looked into. No concrete reasoning for the error of the theoretical calculations were found. The correlation of the margin of error, heave plate radius and velocity for the SPH simulations were presumed to be caused by the choice of viscosity scheme used in the simulations, although no clear solution to this problem is found.
Lastly it is concluded that the theoretical model should only be used for very rough estimations, and SPH simulations can be used to find hydrodynamic constants given that the velocity related errors are solved.

Preface

The following paper was produced by Hans Dueholm and Lars Kristensen of the Master's programme of Structural and Civil Engineering at Aalborg University. The project was supervised and helped along by associate professors Jonas Bjerg Thomsen and Mads Røge Eldrup.

The paper describes the efforts and results of the project group throughout the masters project, and seeks to combine theoretical, numerical, and experimental methods to model the hydrodynamics of a heave plate.

Aalborg University, June 10, 2021

Hans Lindenchrone Dueholm
<hdueho16@student.aau.dk>

Lars Kristensen
<lkr16@student.aau.dk>

For the reader

Sources and external references mentioned are listed according to the Harvard method [Author, Year] and may be found under the section "Bibliography". For undated internet sources, a date is stated for the time of the last visit.

Figure and table numbering follows the current chapter number in order. Mathematical equations and expressions may be numbered, and these are referenced in the format: "... is determined by (1.1)", where the parentheses refer to the equation in (chapter, equation number). Table columns will, when necessary, contain the unit(s) of the below indexes in a square bracket [kg]. For appendices, the above are assigned letters instead of chapter numbers, e.g. 'Figure A.1', 'Table C.2' and equation '(E.14)'.

Contents

Introduction 1

As society has progressed the need for electricity to power everyday life has increased as well. Most of that power has traditionally come from fossil fuels. The problem is that these fossil fuels produce greenhouse gasses which in turn heat up the planet. The planet average temperature has risen 1.11 °C since the 1850's. This rise in temperature has caused glaciers and icecaps to melt at an increased rate, and as a result sea levels has risen. If the temperature continues to rise we can expect more intense heat waves, more violent storms and even higher sea levels. [NASA, 2021]

If the effects of climate change is not enough to deter our civilisation from the use of fossil fuels there is another limit which should be considered. Nature produces fossil fuels much slower than the speed of our consumption, which simply means that we will run out. With the consumption levels of 2015 and the, at the time, known reserves, we are expected to run out of oil, gas and coal by the years 2066, 2068 and 2129 respectively. Since our energy consumption is not expected to diminish, we need renewable energy to gradually take over the energy production from the fossil fuels. In 2019 16,5 % of Europe's power production came from renewable energy sources. The two biggest contributors being hydropower at 6,73% and wind at 4,91%. See figure 1.1 [Our World in Data, 2020]

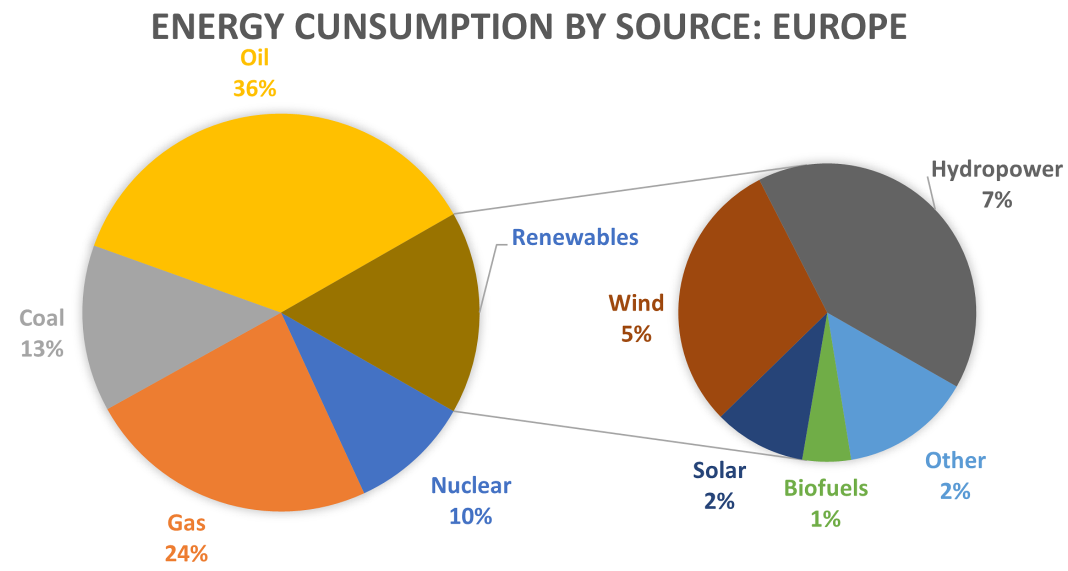

Figure 1.1: Energy consumption by source 2019 [Our World in Data, 2020].

Wind energy

One of the biggest contributors to the European renewable energy sector is wind energy, with a total capacity of 205 GW in 2019. In addition there is substantial growth in this sector, with an additional 15.4 GW installed in 2019 alone. Figure 1.2 shows the increase in wind energy, where notably there is an emerging sector of offshore wind energy on the rise. Though offshore wind is still around 50% more expensive than traditional onshore wind, there are still plenty of motives for moving into the oceans. Some of these motives are aesthetic as the larger and larger wind turbines, visual and audible perceived nuisances is reduced when moving them out to sea. There is also logistical benefits, as transportation of larger turbines on land are more limited by weight, width and length of the nacelle and blades. The main drive however is the larger wind fetches and the low shear surface of the open sea, which results in higher and more stable wind speeds.

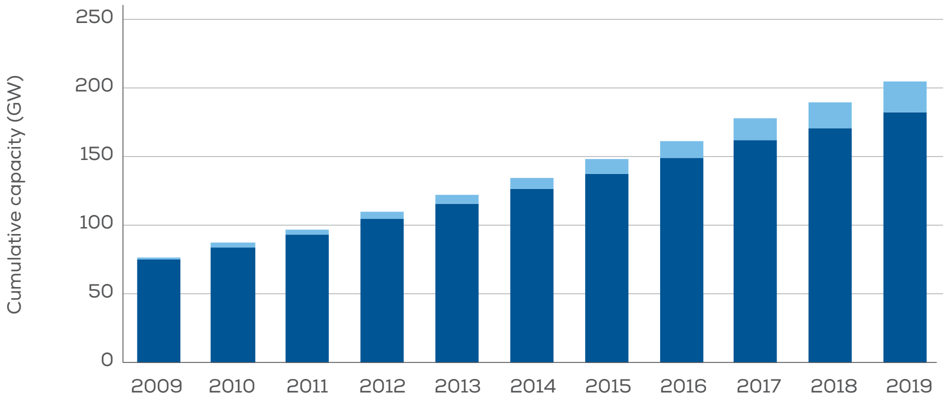

	2009	2010	2011	2012	2013	2014	2015	2016	2017	2018	2019
Offshore	2	3	4	5	7	8	11	13	16	18	22
Onshore	75	84	93	105	115	127	137	149	162	171	183
Total	**77**	**87**	**97**	**110**	**122**	**135**	**148**	**162**	**178**	**189**	**205**

Figure 1.2: Total installed wind power capacity in Europe [Wind Europe, 2020].

The offshore wind industry have been thriving with the accessibility of suitable locations in the North Sea, where there is a combination of good wind resources, shallow water depths and short distance to the shore. The shallow water have resulted in the mono pile being the preferred foundation type for offshore wind, with 81% of the the cumulative share. However a great share of the offshore wind energy is in deep water, where conventional bottom-fixed designs are infeasible. Estimations of the share of offshore wind resource with > 60 m water depth for USA, Japan and Europe are 60%, 80% and 80% respectively [Wind Europe, 2017]. For reference wind resource- and bathymetry maps of Europe are shown on figure 1.3 and 1.4 respectively.

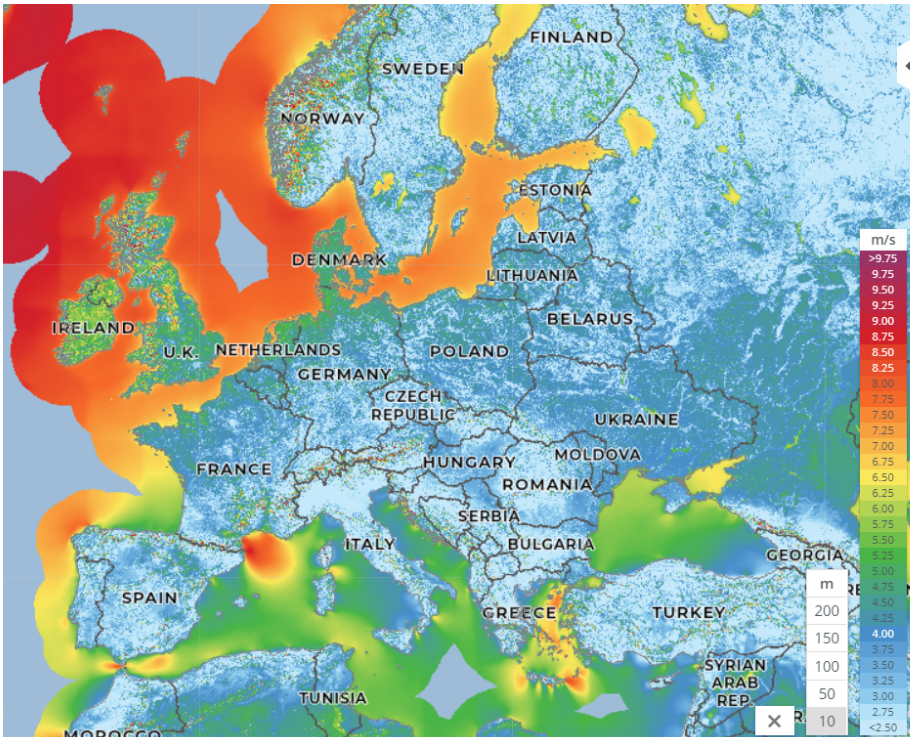

Figure 1.3: Offshore wind resource measured as mean wind speeds [m/s] [Global Wind Atlas, 2021].

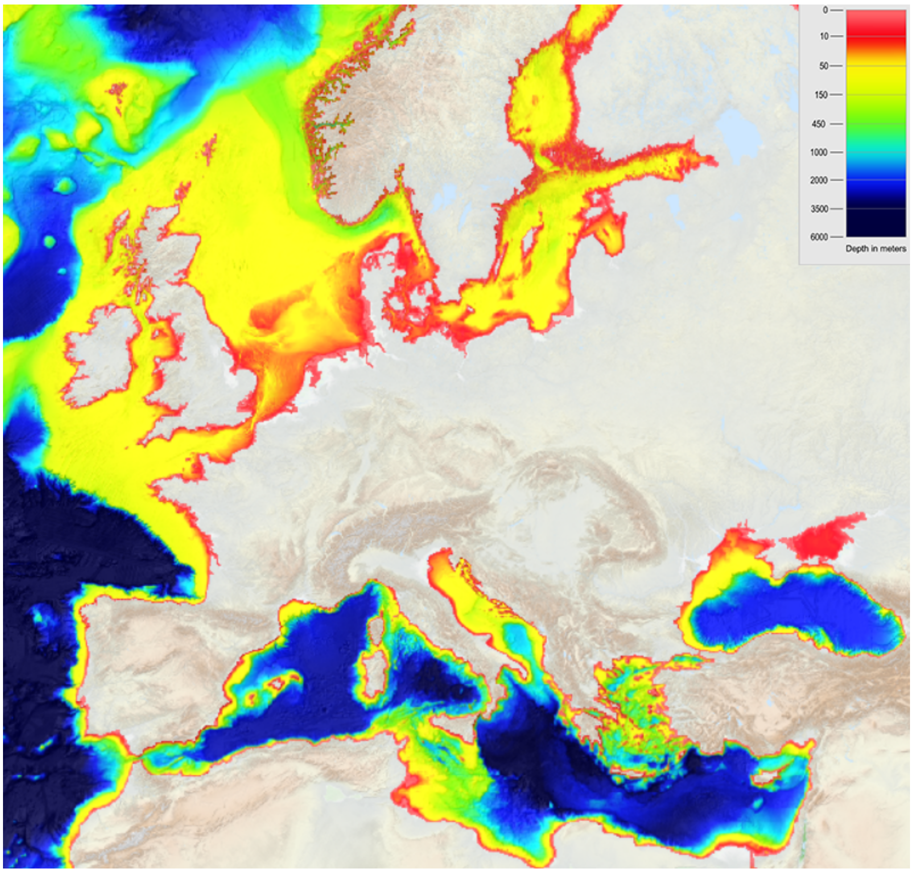

Figure 1.4: Bathymetry map of the seas around Europe [EMODnet, 2021].

Floating wind turbines

The traditional offshore wind turbines, with monopile foundations, get more expensive as the water depth increases. As a result there is a natural limit for depths in which they are profitable. Considering that locations with large areas of sufficiently shallow sea, and large wind resources are scarce. A logical solution would be to engineer a floating offshore wind turbine (FOWT), solving the price problem by minimising the increased cost at greater depth.

A multitude of floating wind turbine concepts have been created and tested. Although three archetypes seem dominant in terms of the foundation. The spar buoy-, the semi submersible-, and the tension leg platform (TLP) designs. see figure 1.5.

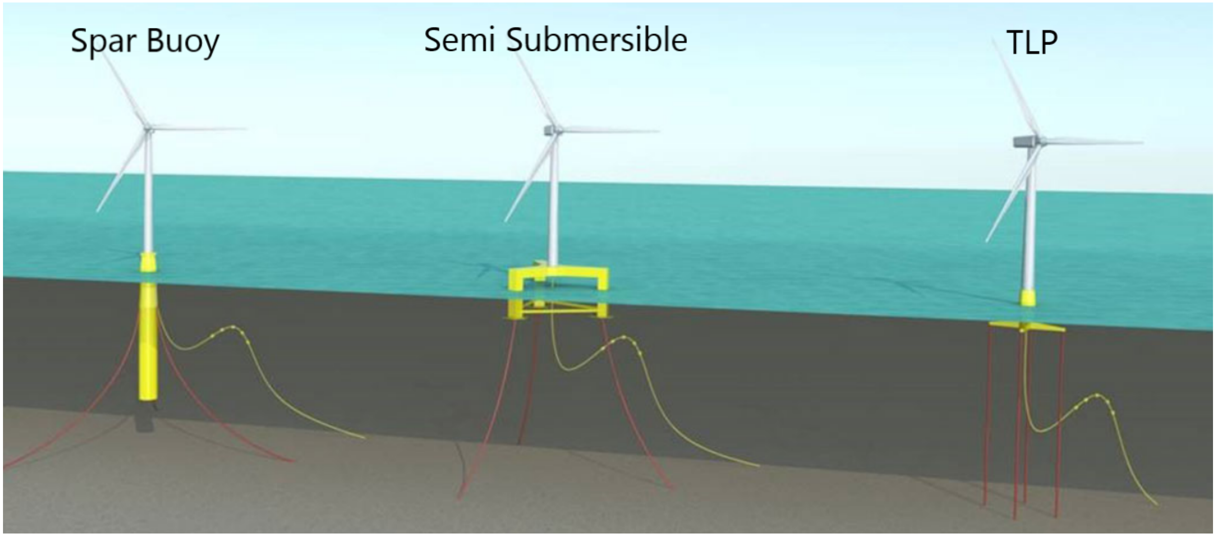

Figure 1.5: Three archetypes of the floating wind turbines [Rambøll, 2021].

The spar buoy design is a ballast stabilised concept. The mass of the spar lowers the construction's centre off mass, and thereby keeps the wind turbine stabilised by the same concept as a regular sea buoy. While promising in terms of stabilising the wind turbine, the design is limited by the depth at which the ballast is located. As an example, the ballast stabilised concept developed by Stiesdahl A/S, the TetraSpar, has a lower depth limit of 100 m [Stiesdal, 2021]. This is not the case for the two other design archetypes. The TLP is stabilised by the tensioned anchoring lines, making the anchoring the main stabilising feature. This is one of the main deficits of the TLP as well, since it increases the requirements of the foundation substantially. The semi submersible design is stabilised by concept of a wide area and the hydrodynamics of the structure. The advantages being that it is mostly self stabilised and has almost no lower depth limit.

One of the stabilising hydrodynamic choice features of the semi submersible design is the heave plates, a horizontal circular plate mounted on the floaters in each corner of the structure. These plates stabilise the wind turbine by essentially working as a free form of viscous damper, requiring a mass of water to be moved around the plates every time the wind turbine rotates around its centre of mass, and thereby inducing heave-like motions on the plates.

Wave induced loads on large volume structures are often predicted based on potential theory, which means that the loads are deduced from a velocity potential of the irrotational motion of an in-compressible fluid. The most common numerical method for solving the potential flow is a Boundary Element Method (BEM) where the velocity potential in the fluid is represented by a distribution of sources over the mean wetted body surface. The mean wetted surface is then discretized into flat or curved panels. However for this method to give valid results some assumptions have to be made. One of the assumptions is that the oscillation amplitude of the fluid and the body are small relative to the cross-sectional dimensions of the body [C.-H. Lee, 1995]. This means that this method is not well suited for constructions with a high dynamic range which is often the case for FOWT. However a promising solution to this problem could be Smoothed Particle Hydrodynamics (SPH) which does not face the same limitations as the traditional BEM. SPH solves the problem by simulating a large amount of particles, where the particles represent the flow and can interact with structures. However SPH does face some problems, the main problem for its application to real engineering problems is the excessively long computational runtimes, meaning that SPH is rarely applied to large domains. As both BEM and SPH faces problems when predicting the hydrodynamic effecs, the most common method of defining these effects are trough physical experiments.

1.1 Objective

Asses the hydrodynamic effects of heave plates via a theoretical approach, SPH modeling and physical tests. Ascertain whether the theoretical approach and SPH model are valid for predicting the hydrodynamics of a heave plate.

1.2 Approach

The hydrodynamic effects of the heave plate, can be described by the resulting force induced by the water on the heave plate as it moves. This force is the result of two components. Namely the inertia force induced by the water being displaced around the heave plate, also referred to as added mass, and the drag forces based on the dampening effect of the plate.

In this project three models are set up to produce a time series of the forces induced on the heave plate as it moves: A theoretical approach based on the Morison equation, a numerical SPH model, and an experimental model. Results of the models are compared, by their resultant force amplitudes, added mass and drag coefficients. Eventual differences and trends are discussed, and the viability of the models are assessed.

To facilitate comparisons between the modelling methods a common simplification of the general heave plate problem is made.

1.3 Simplification of the problem

The general problem of a floating semi submersed wind turbine is a complex case with effects from both wind and waves influencing the hydrodynamics of the floating foundation, and thereby the heave plates. A simpler model is created for general use in all three methods of investigating the heave plate effects.

Heave plates work as a form of viscous damper. When the effects of wind and waves cause the tower to rotate around its centre of mass, it causes the heave plates to move with it, pushing them either up or down depending on the direction of the rotation. To better fit a modeling situation the effects of the wind turbine is excluded, and the rotational movement is simplified to a sinusoidal rectilinear motion. A visual representation of the simplification is sketched figure 1.6. Additionally the simplified model shows the isolated effects of the heave plate, reduces computational time of the SPH simulations and reduce the complexity of the experiments.

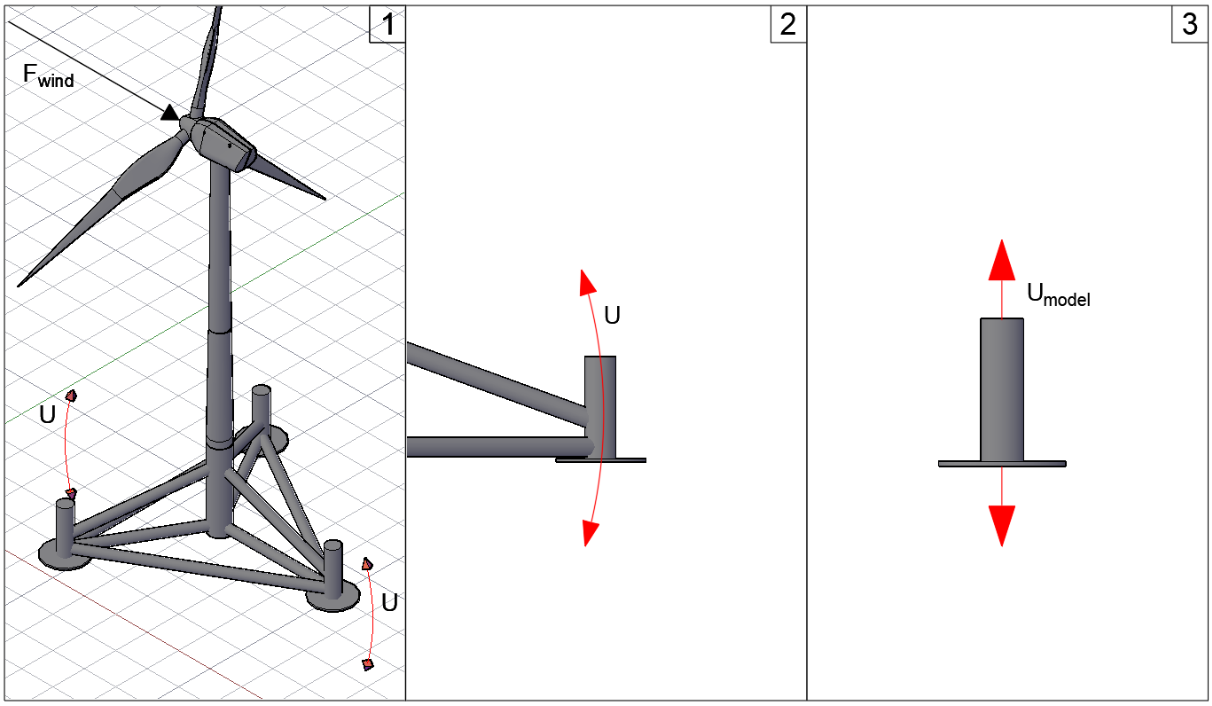

Figure 1.6: [1] represents the general problem of a floating wind turbine with the movement of the heave plates denoted U. [2] Represents a simplification where only one heave plate is considered, still with the real motion U. [3] The simplified model excluding rotational effects resulting in the model movement U_{model}.

With these simplifications the basis for the models of this project can be viewed in figure 1.7. In the theoretical approach effects from the proximity of the boundaries, thereby walls, bottom, and to a certain degree the surface are not taken into account, since the theory is based on the assumption that the body is submerged in an infinite body of water. The SPH model and experiment will on the other hand have boundaries as described, though dimensions may vary.

The model movement U_{model} is assumed to be a sinusoidal oscillatory motion following:

$$U_{model}(t) = a \cdot sin(2\pi f t + \phi) \tag{1.1}$$

Where:

a	The amplitude of the motion.
f	Frequency of the oscilation in [Hz]
ϕ	Phase shift.
t	Time.

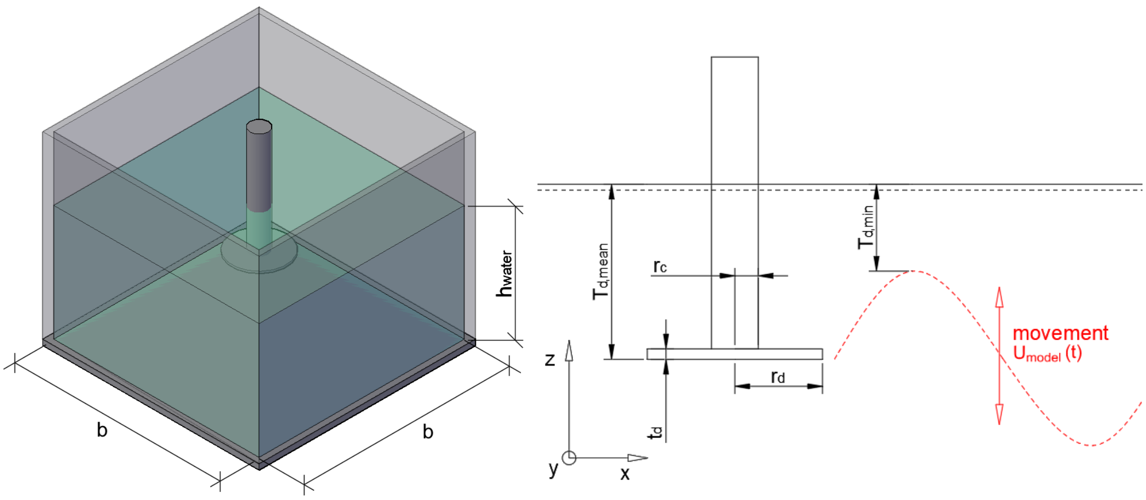

Domain dimensions	
h_{water}	Water depth from bottom to SWL
b	Width of the domain
Heave plate and cylinder	
$T_{d,mean}$	Mean draft from SWL to the bottom of the disc
$T_{d,min}$	Minimum draft from SWL to the bottom of the disc
r_d	Radius of the disc
r_c	Radius of the cylinder
t_d	Thickness of the disc
$U_{model}(t)$	Movement of the disc and cylinder

Figure 1.7: Basis for most models used in this project.

Theoretical Approach 2

This chapter describes a model of the problem based mainly on Morisons equation, used as a point of reference for SPH simulations and experimantal results

2.1 Morison equation

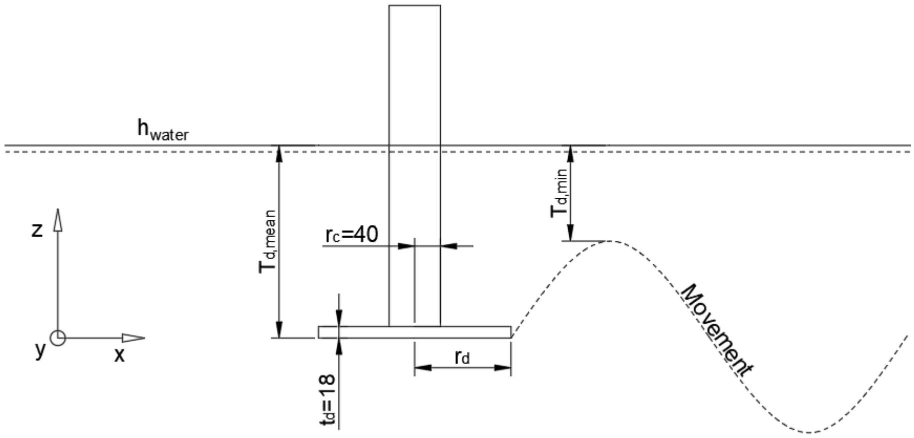

Figure 2.1: Visualisation of the basis for the theoretical approach.

A theoretical approach is set up based on the model basis displayed in figure 2.1. The approach is based mainly on the Morison equation, which is the presented standard of which to calculate forces on objects subjected to moving water by [DNV GL A/S, 2011]. The Morison equation defines the force acting on an object submerged in a fluid based on the velocity and acceleration of the fluid particles, and the shape of the object. The equation is build from the assumption that the total force acting an object is the the sum of inertia and drag forces on said object:

$$F = \underbrace{(1 + C_a)\ V_R\ \rho\ \alpha_f}_{inertia} + \underbrace{1/2\ \rho\ C_d\ A\ \left|v_f\right|\ v_f}_{drag} \tag{2.1}$$

Where:

F	Fluid force acting on the body.
C_a	Added mass coefficient for the body.
V_R	Reference volume of fluid displaced by the body.
α_f	Fluid particle acceleration.
ρ	Density of water.
C_d	Drag coefficient for the body.
A	Drag area.
v_f	Fluid particle velocity.

Since the heave plate is submerged in still water and subjected to motion, it is assumed that the particle velocity and accelerations relative to the plate is equal to, but opposite the velocity and accelerations of the plate:

$$U_f = -U_{model} \rightarrow v_f = -U'_{model} \rightarrow \alpha_f = -U''_{model} \tag{2.2}$$

The added mass coefficient for the body is found as the ratio of the added mass to the displaced mass. [DNV GL A/S, 2011]

$$C_a = \frac{m_{added}}{\rho\, V_R} \tag{2.3}$$

The added mass for a cylinder with a circular disc attached to the bottom is not standardised. And multiple choices exist. [Tao et al., 2007] defines the added mass of the body as the mass of an elliptoid surrounding the disc, minus the volume of the cylinder where it overlaps. The ellipsoid has semi axes a, b, c defined as $a = b = D_d/2$, $c = D_d/\pi$, with the body oscillating in the direction of semi axes c. The added mass can be found as:

$$m_{added} = \frac{1}{12}\rho(2D_d^3 + 3\pi D_d^2 z - \pi^3 z^3 - 3\pi D_c^2 z) \tag{2.4}$$

Where D_d and D_c is the diameter of the disc and cylinder respectively, and z is defined as:

$$z = \frac{1}{\pi}\sqrt{D_d^2 - D_c^2} \tag{2.5}$$

Alternatively the added mass of a circular disc without the cylinder can be used, as defined in [DNV GL A/S, 2011]:

$$m_{added} = \frac{8}{3}\rho\, r_d^3 \tag{2.6}$$

With r_d being the radius of the disc.

The reference volume V_R takes into account the volume of water being displaced by the movement of the body. As for m_{added} the specific shape of a cylinder with a disc attached at the bottom is not standardised and multiple definitions are considered. [Tao et al., 2007] defines the reference volume as the volume of the whole body:

$$V_{R,Tao} = V = \frac{1}{4}\pi(D_c^2\, T_c + D_d^2\, t_d) \tag{2.7}$$

Taking into account both the thickness of the disc t_d and the draft of the cylinder T_c. In contrast [DNV GL A/S, 2011] defines the reference volume of a circular disc as the volume of the sphere corresponding to the disc radius.

$$V_{R,DNV} = \frac{4}{3}\pi\, r_d^3 \tag{2.8}$$

Since the DNV approach only takes the disc into account it is constant, and independent of the draft of the heave plate. Where in comparison the volume used by [Tao et al., 2007] is highly dependant on the draft. With the assumption that the body is submerged in an infinite body of water, the draft would be infinite as well resulting in an infinitely large volume and thereby an infinitely small value of C_a. Therefore two additional options of our design are added for comparison. The first of the two is equal to the volume of the sphere used by DNV minus the volume of the cylinder where it intersects the sphere:

$$V_{R,Sphere} = \frac{4}{3}\pi\, r_d^3 - \pi\, r_c^2\, r_d \tag{2.9}$$

The second assumes that the reference volume is roughly equal to the volume of water in the ellipsoid which induces the added mass of a disc:

$$V_{R,Ellipse} = \frac{1}{3} D_d^3 - \pi\, r_c^2\, r_d \tag{2.10}$$

A visualisation of the different reference volumes are given in figure 2.2

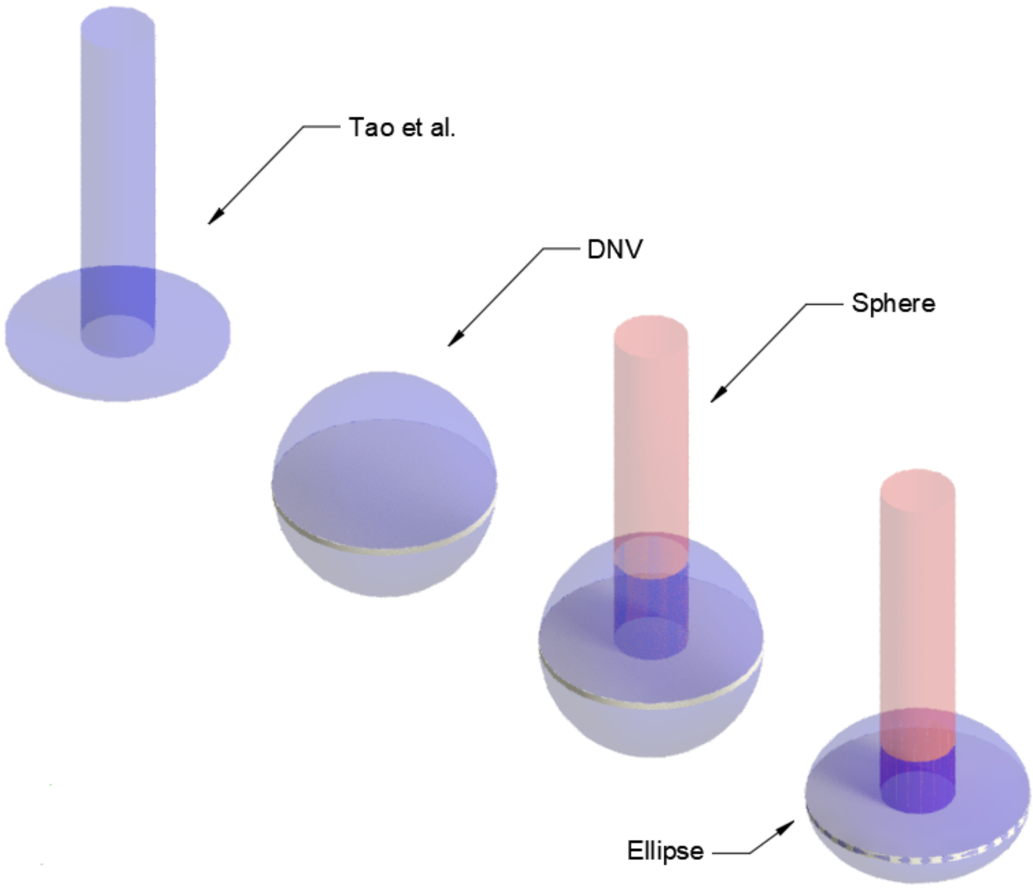

Figure 2.2: A visual representation of the different reference volumes used. Blue represents the reference volume, red represent volumes that has been subtracted.

As for the values of the drag coefficient C_d and drag area A_d is concerned, the drag coefficient of a circular disc is used ($C_d = 1.12$) as well as the drag area of the disc. This is deemed a good assumption since the maximum velocities present in the simulations induce low KC numbers ($KC < 5$) insinuating that the simulation is in inertia regime, resulting in the drag contributions from Morison's equation being small. As an example for an oscillating frequency of $f = 0.2\,\text{Hz}$ $KC = 2.09$. For reference the drag coefficient is found from the following relation: [DNV GL A/S, 2011]

$$C_d = \frac{2B}{\rho\, A_p} \tag{2.11}$$

With B being the linearised damping.

2.2 Results

The calculation is run for each of the possibilities of m_{added} and V_R. Here results will be shown for the four variations with input parameters shown in table 2.1. The movement input is plotted in figure 2.3, and resultant forces are plotted in figure 2.4. Additionally the calculation is run for variations of the movement amplitude a, frequency f and disc radius r_d. Result of these variations are shown for the DNV approach in Appendix D

	r_d [mm]	r_c [mm]	t_d [mm]	$T_{d,mean}$ [mm]	a [mm]	f [Hz]	m_a [kg]	V_R [m^3]	C_a [-]
Tao	150	40	18	300	100	0.2	8.27	0.0031	2.70
DNV disc	150	40	18	300	100	0.2	9.00	0.0141	0.64
Tao $V_{R,Sphere}$	150	40	18	300	100	0.2	7.90	0.0138	0.60
Tao $V_{R,Ellipse}$	150	40	18	300	100	0.2	7.90	0.0090	0.92

Table 2.1: Input parameters for the four variations of the calculation.

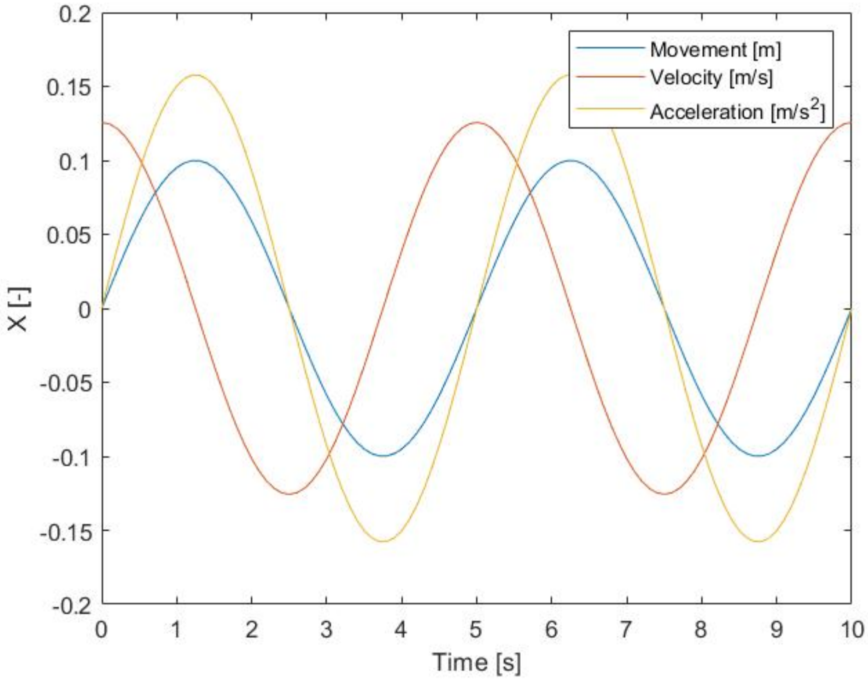

Figure 2.3: Movement, velocity and acceleration for the calculation with input parameters of 2.1.

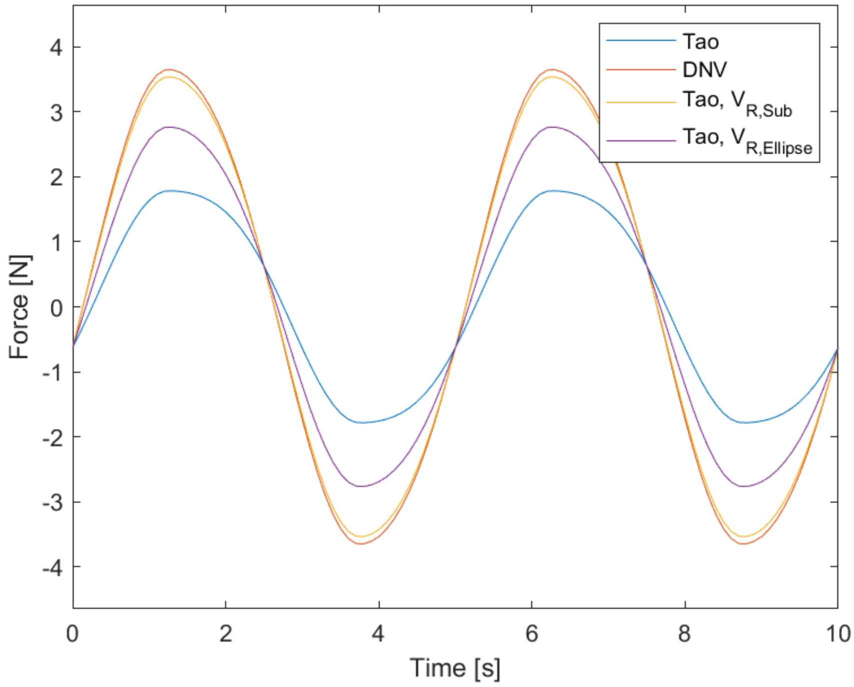

Figure 2.4: Resultant Morison force acting on the heave plate for the four settings.

As expected, results for input parameters of the method presented in [Tao et al., 2007] yields the smallest loads this is mainly due to the reference volume being small compared to the other choices. This is a direct result of the chosen draft $T_{d,mean}$ of the method. The calculations for the isolated disc according to [DNV GL A/S, 2011] results in the largest forces due, to the larger added mass and reference volume.

The two setting with improvised volume $V_{R,Sphere}$ and $V_{R,Ellipse}$ yields results that are in the intermediate range of the formulations by Tao and DNV, with $V_{R,Sphere}$ yielding the larger forces. The results are not surprising as, they scale with the value of V_R.

Experiments 3

This chapter describes the conducted experiments, processing of the experimental data and results.

As the theory described in chapter 2.1 comes with certain limitations in terms of the geometric shape of moving bodies in water. A more accurate way of observing hydrodynamic effects on moving bodies in water, is an experiment performed in a controlled environment.

Experiments in this project have been conducted to identify the hydrodynamic- forces and dampening effects of a circular heave plate. For this purpose heave plates with different radii are tested at variations of amplitude, frequency and distance to the surface. These experiments are used as a point of comparison alongside the theory and SPH simulations in chapter 5.

3.1 Experimental setup

The experiments are conducted in the wave basin in The Ocean and Coastal Engineering Laboratory at Aalborg University. A plan of the wave basin is displayed on figure 3.1, with a corresponding photo of the setup in figure 3.2.

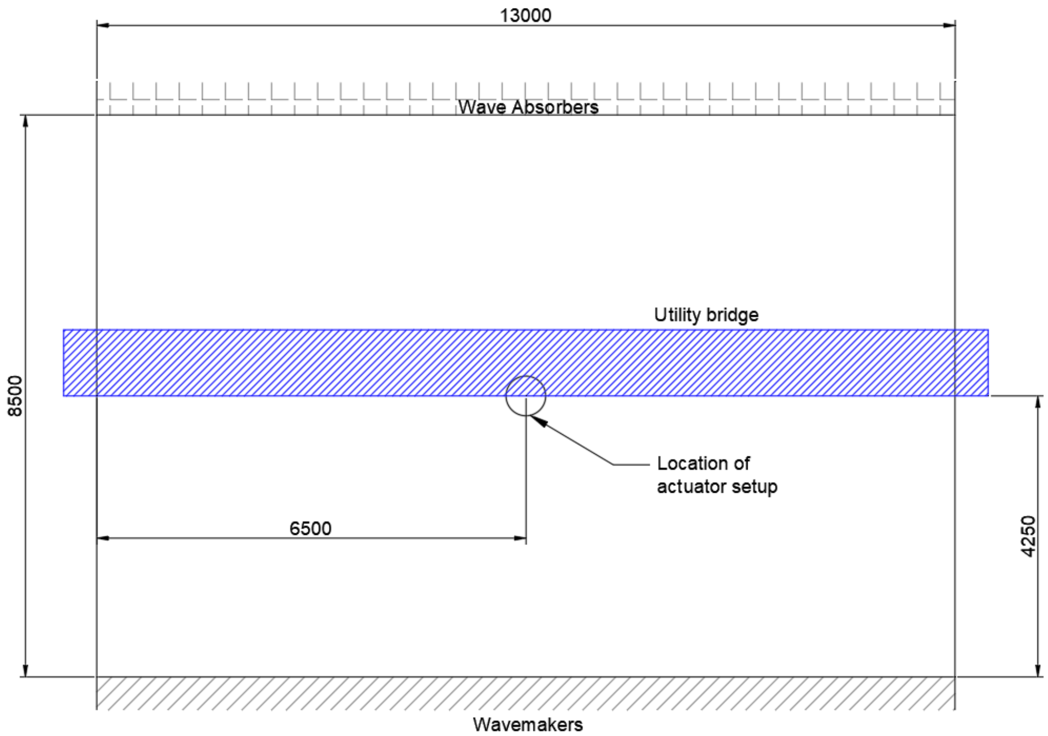

Figure 3.1: Top-down view of the wave basin with the location of the actuator setup. All measurements are in [mm].

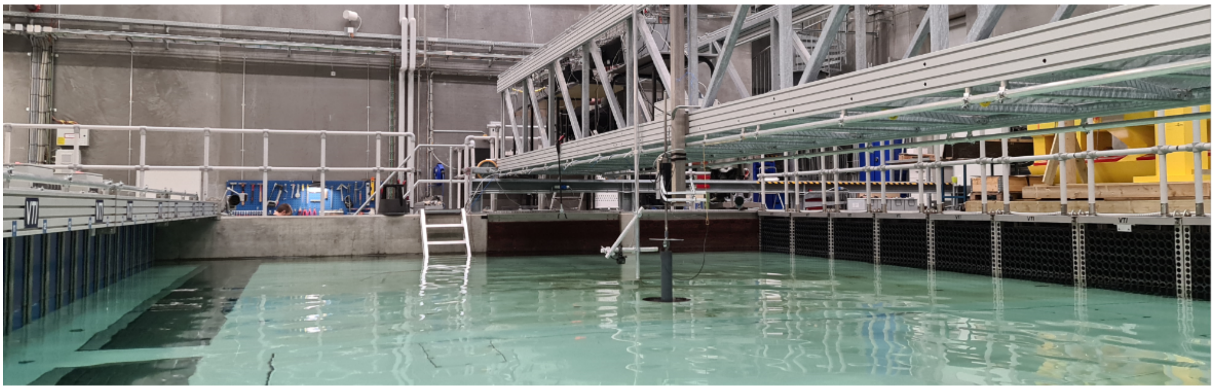

Figure 3.2: Photo overlooking the experimental setup in the wave basin.

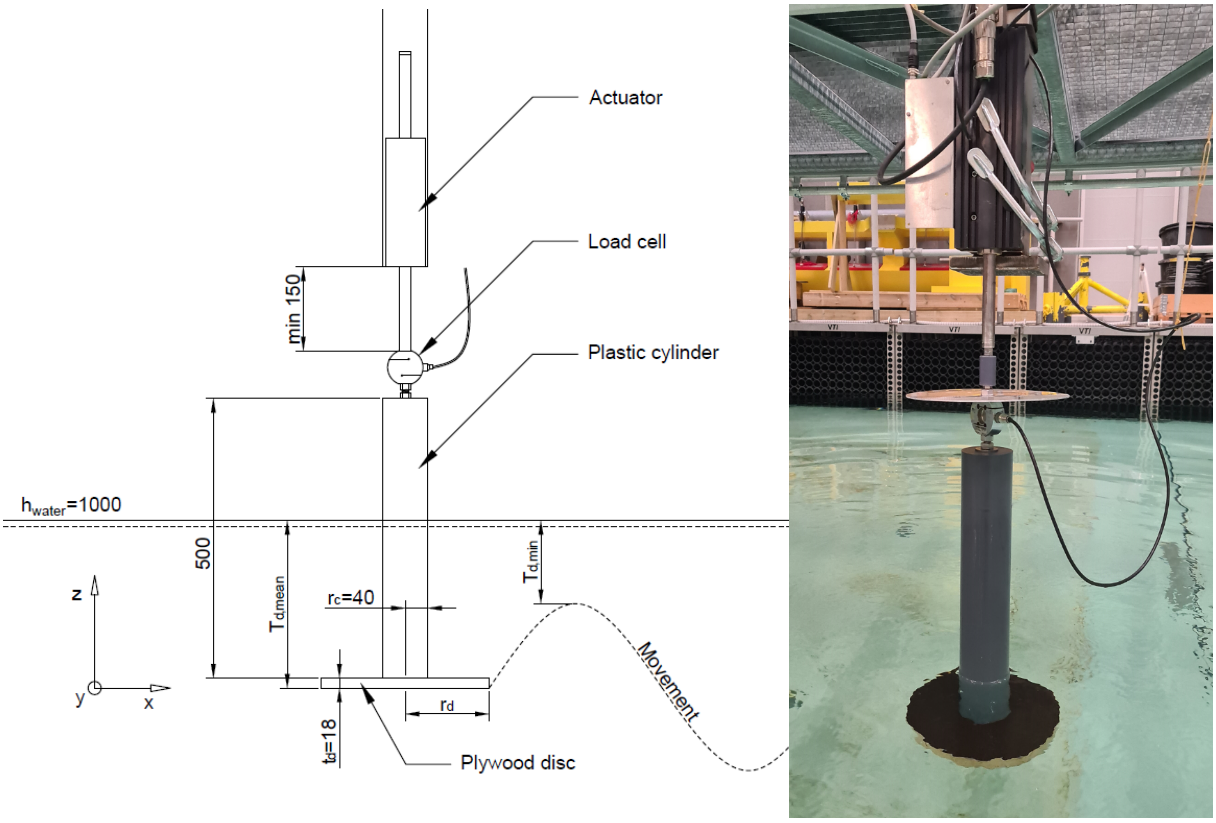

Figure 3.3: The experimental setup used. All measurements are in [mm].

The experimental setup is based on the same simplification of the problem as both the SPH model and theoretical approach, explained in section 1.3.

The model is build from a plastic cylinder with a length of 500 mm and $r_c = 40$ mm, plywood discs with $t_d = 18$ mm and varying values of r_d are mounted to the bottom of the cylinder with five 5.6 mm bolts. The movement of the heave plate is induced by a LinMot HS01-37x286 actuator, which the cylinder is attached to. The output of the experiments comes from a VETEK TS-100kg load cell mounted between the actuator and the cylinder with an M12 threaded rod and nuts. See figure 3.3. This setup is mounted to the utility bridge as shown on figure 3.1.

3.1.1 Instrumentation

HS01-37x286 actuator Induces movement on the heave plate setup based on the input movement function. The actuator has maximum specified force and velocity 308 N and 3.8 m/s respectively. The peak velocity for the maximum amplitude and frequency, $a = 150$ mm and $f = 1$ Hz is 0.94 m/s.

VETEK TS-100kg load cell The output of the experiment comes from the load cell, which outputs a certain voltage based on the load it is subjected to. The voltage is lowered in tension and increases in compression, due to the changes in resistance from the load cells internal strain gauges. The load cell is calibrated to yield results that are never outside the limits of -10 and 10 V for the load sizes expected in the experiment, as voltages outside the limits are not recorded. The calibration resulted in the translation function, where x is the output of the load cell in volts:

$$F(x) = (-16.654x + 29.967) \text{ [N]} \tag{3.1}$$

A second calibration is performed after the experiments are conducted, resulting in a translation function which differed from the one used during experiments by 0.11 % on the slope and −2.07 % on the offset. Details on the performed calibration procedure can be found in appendix C.

3.2 Tested parameters

The experiments conducted are chosen to represent a variety of hydrodynamic cases for the heave plate. By varying the parameters of the test, the effects of the individual parameters might be interpreted from the experimental results. The parameters chosen to be varied are: Movement amplitude a, movement frequency f, disc radius r_d and disc draft $T_{d,mean}$.

The movement parameter variations, are made to give insight to the effects of different velocities and accelerations, and ensure that any connections found between parameters and results are not exclusive to certain sizes of movement. The disc radius is varied to see the effects on the resultant force, induced added mass and the dampening factor of the heave plate. Varying the mean draft alongside the variation of a is expected to give insight into the influence of proximity to the surface.

The parameter variations tested are

- Movement amplitude a is is tested at $a = 25$, 50, 100 and 150 mm.
- Movement frequency is tested in the interval of $f = 0.2$ to 1 Hz with steps of 0.2 Hz.
- The heave plate radius r_d is tested in the interval $r_d = 100$ to 200 mm with steps of 25 mm.
- The mean draft for all combinations of the previously mentioned variables is set to $T_{d,mean} =$ 300 mm. Additionally a set of tests for certain combinations of amplitude and frequency for $r_d = 150$ mm at the minimum draft of the movement $T_{d,min} = 150$ mm, 100 mm and 50 mm is conducted.

An overview of the experiments performed are shown in tables 3.1 and 3.2.

	$r_d = 100\,\mathrm{mm}$	a [mm] 25	50	100	150
	0.2	-	-	-	-
	0.4	-	-	-	-
f [Hz]	0.6	-	-	-	-
	0.8	-	-	-	-
	1	-	-	-	-

Table 3.1: Experiments performed for the experiments with $T_{d,mean} = 300\,\mathrm{mm}$, the displayed tests are performed for the variations of radius from $r_d = 100$ to $200\,\mathrm{mm}$

$T_{d,min}$ [mm]	15		10		5	
a [mm]	0.05	0.1	0.05	0.1	0.05	0.1
0.2	-	-	-	-	-	-
0.4	-	-	-	-	-	-
0.6	-	-	-	-	-	-
0.8	-	-	-	-	-	-
1	-	-	-	-	-	-

Table 3.2: Experiments performed for the variation of minimum draft. All experiments are performed with $r_d = 150\,\mathrm{mm}$

3.3 Raw data

Most of the combinations described in section 3.2 are tested in the basin for a movement duration of 60 s and yielded a time series of loads. Certain combinations were not tested or cut short due to the structural instability of the experimental setup. Those were combinations with high frequencies and large amplitudes specifically. Time series for 10 seconds of some choice combinations of amplitude and frequency are shown in figures 3.4 to 3.7.

It is evident that there is a lot of scatter in the data, and some filtration are required. Figure 3.4 represents a situation where the actuator did not perform the movement very well, causing the actuator to shake at a certain frequency. This is a general problem which was visible in mainly the tests at small amplitudes and low frequencies.

Figures 3.5 and 3.6 represents experiments that did not evidently suffer from the previously mentioned problems. Although data scatter are still present.

Figure 3.7 represent a case where the experiment was stopped due to structural instability of the setup. The heave plate started to move horizontally in the water, and the experiment was stopped due to fear of the setup breaking. This was the cause of some experiments not being performed.

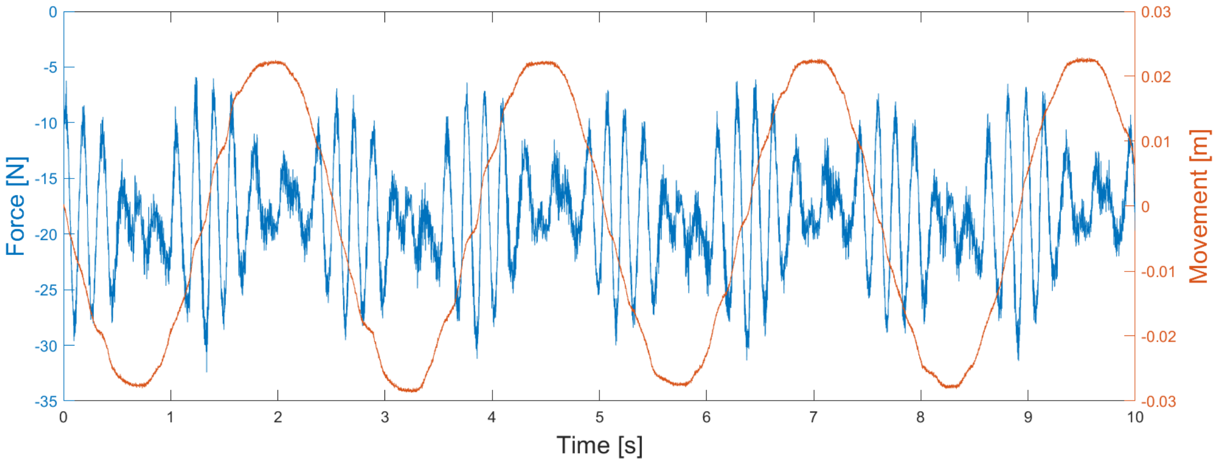

Figure 3.4: Load time series for $r_d = 150\,\mathrm{mm}$, $a = 25\,\mathrm{mm}$, $f = 0.4\,\mathrm{Hz}$.

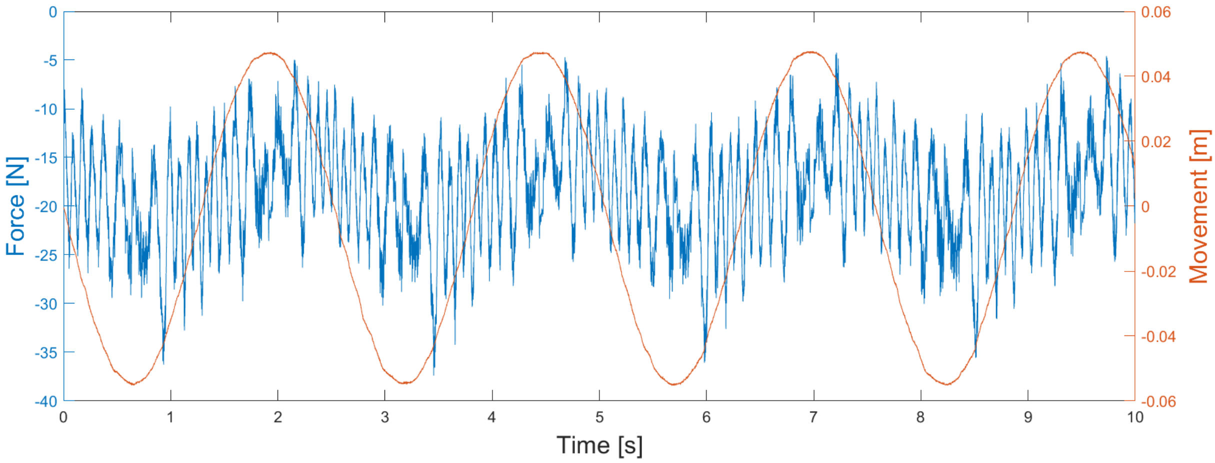

Figure 3.5: Load time series for $r_d = 150\,\mathrm{mm}$, $a = 50\,\mathrm{mm}$, $f = 0.4\,\mathrm{Hz}$.

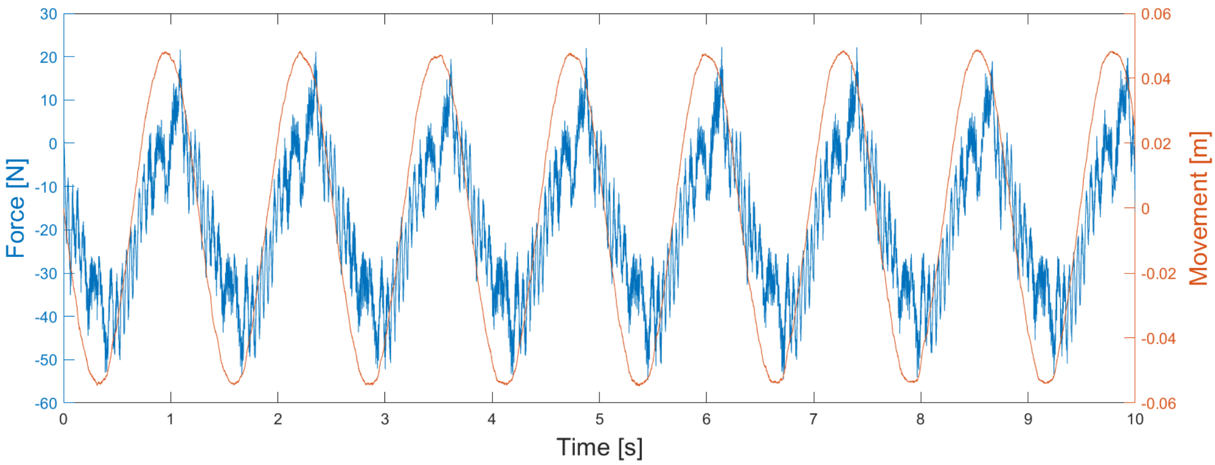

Figure 3.6: Load time series for $r_d = 150\,\mathrm{mm}$, $a = 50\,\mathrm{mm}$, $f = 0.8\,\mathrm{Hz}$.

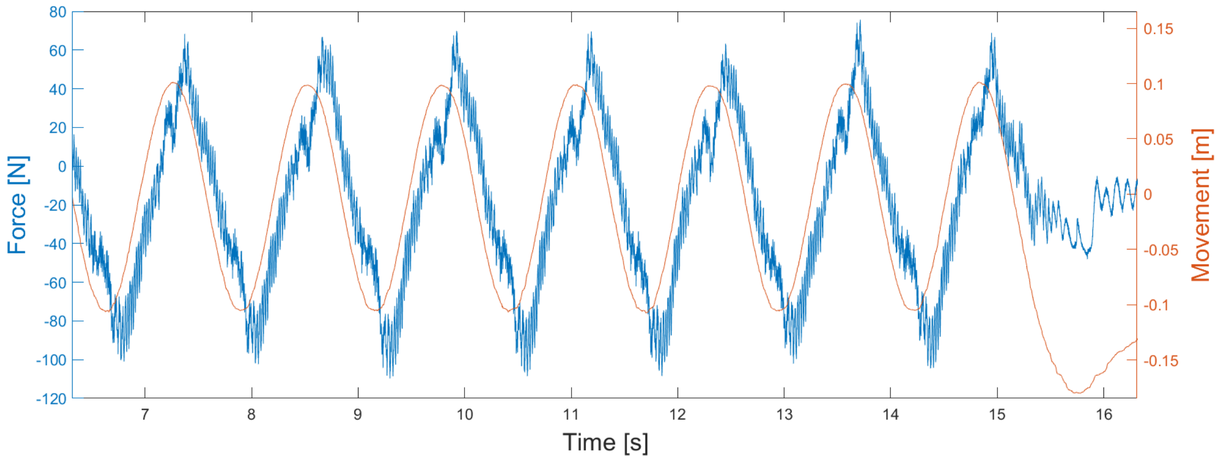

Figure 3.7: Load time series for $r_d = 150\,\text{mm}$, $a = 100\,\text{mm}$, $f = 0.8\,\text{Hz}$.

3.4 Data processing

As the raw data includes effects from the weight and buoyancy of the setup and noise from, presumably the actuator motor, some data processing is required before the time series are comparable to both the theoretical results and the results from the SPH simulations.

3.4.1 Weight and buoyancy

Since the setup is suspended by the load cell, the resultant loads includes the weight of a part of the setup, and since the movement varies the draft of the setup, buoyancy effects changes with the movement. The effects of this weight, and the counteracting buoyancy needs to be subtracted from the results if they are to only reflect the effects of the heave plate. The weight of the experimental setup suspended by the load cell is given in table 3.3

Configuration with r_d	100 mm	125 mm	150 mm	175 mm	200 mm
Weight m_{model} [kg]	4.02	4.21	4.44	4.69	5.02
Load (stationary) [N]	-39.44	-41.29	-43.55	-45.99	-49.25

Table 3.3: Weight and corresponding static load of the different setup configurations used in the experiment.

The buoyancy is found as a function of the draft:

$$F_{buoy}(t) = (r_d^2\,\pi\,t_d + T_d(t)\,r_c^2\,\pi)\rho\,(-g) \tag{3.2}$$

With $g = -9.81\,\text{N/kg}$ being the gravitational acceleration. The contribution from the weight of the setup is following Newtons second law:

$$F_N(t) = m_{model}\,(g + \alpha(t)) \tag{3.3}$$

With α being the acceleration of the movement. Since the actuator cannot reproduce the specified movement perfectly, there is a small difference in the frequency of the specified movement and the frequency of the specified movement function. This small difference accumulates over each oscillation resulting in the sine curves being out of sync when the experiment have been running for some time. This is illustrated in figure 3.8. Because of this, the input acceleration and the actual acceleration are different at the different time steps, and the input acceleration can not be used as input to calculate the contribution from Newtons second law.

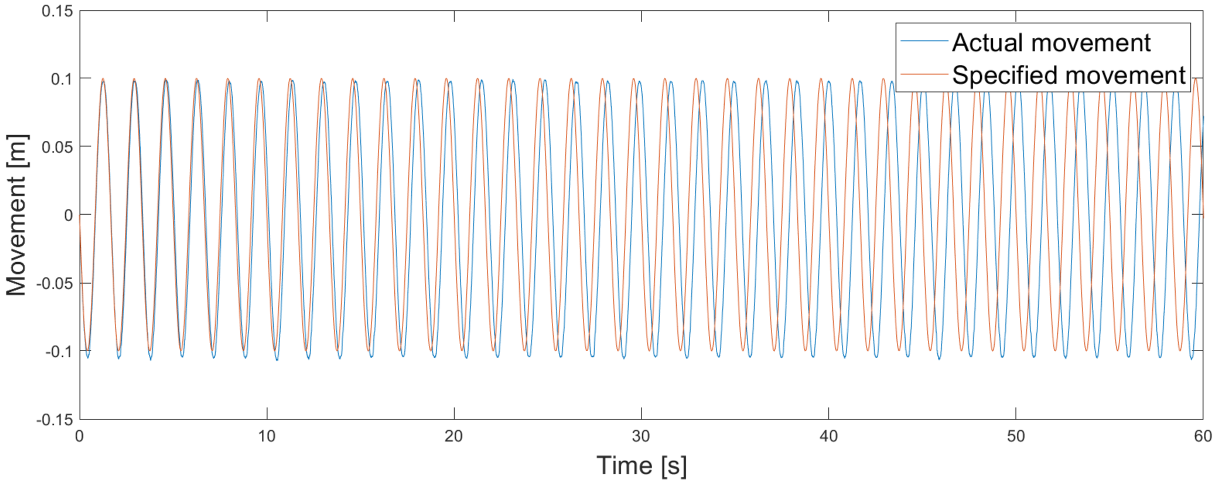

Figure 3.8: Plot of the actual and specified movement functions for: $r_d = 150\,\text{mm}$, $a = 100\,\text{mm}$ and $f = 0.6\,\text{Hz}$.

The acceleration of the actual movement are found by fitting a sine function to the actual movement data points, using the least squares method. The real acceleration are then the 2nd derivative of this function. For reference the difference in amplitude and frequency for the the case with $r_d = 150\,\text{mm}$, $a = 100\,\text{mm}$ and $f = 0.6\,\text{Hz}$ is $2.6\,\text{mm}$ for the amplitude and $0.0062\,\text{Hz}$ for the frequency.

The isolated effects of the heave plates can then be found by equation (3.4).

$$F_{heave}(t) = F_{loadcell} - F_N - F_{buoy} \tag{3.4}$$

As an example the first 10 s of raw output data, and data corrected for buoyancy/Newtons law for the case with $r_d = 150\,\text{mm}$, $a = 100\,\text{mm}$ and $f = 0.6\,\text{Hz}$, and $r_d = 125\,\text{mm}$, $a = 150\,\text{mm}$ and $f = 0.2\,\text{Hz}$ is shown in figures 3.9, and 3.10.

Notably the the force fluctuations in figure 3.10 changes where they are positive and negative. This happens because the raw data represent mostly the variation in buoyancy following the movement of the heave plate. In the case represented on figure 3.9 the force is amplified at the peaks, where the buoyancy counteract the results. It should here be emphasised that it is possible that the variation in buoyancy is slightly different for the experiment cases with higher frequencies and amplitudes. This difference is presumably caused by the disruption of the surface as the water cannot immediately enclose the setup and level out the surface as the heave plates moves up and down.

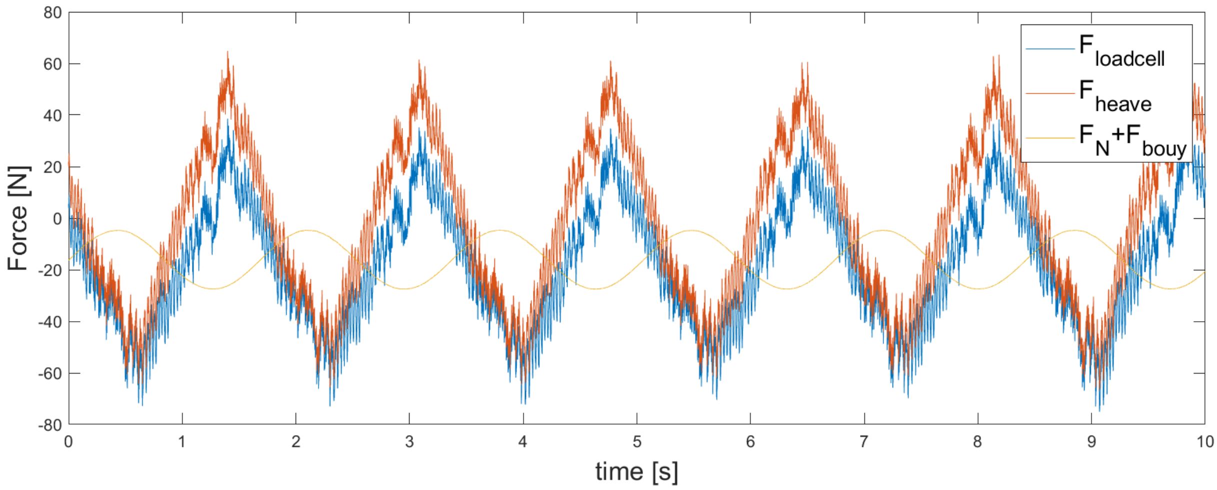

Figure 3.9: The first 10 s of both the raw output data and the bouyancy corrected data for: $r_d = 150\,\mathrm{mm},\ a = 100\,\mathrm{mm}$ and $f = 0.6\,\mathrm{Hz}$.

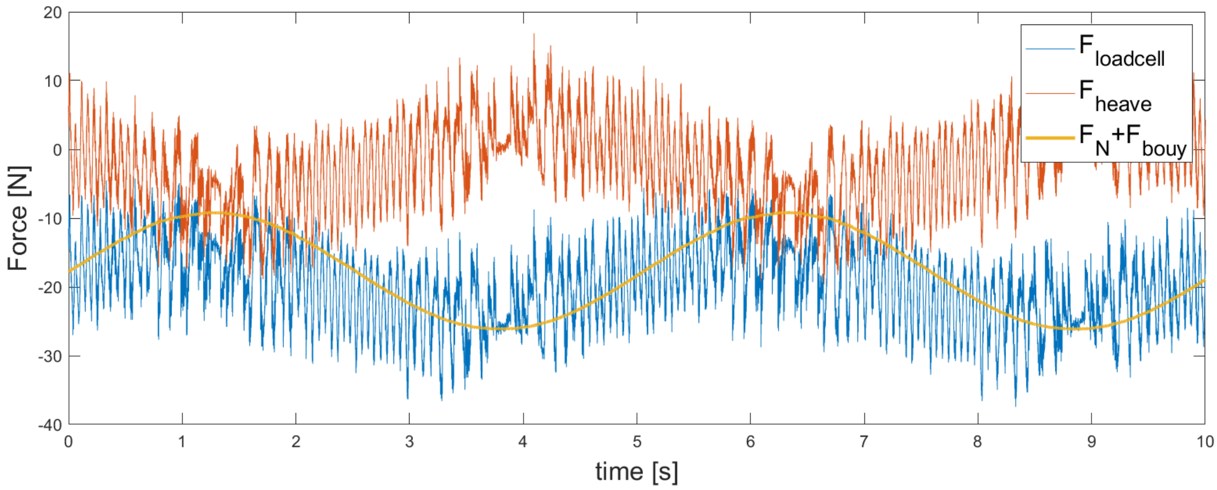

Figure 3.10: The first 10 s of both the raw output data and the bouyancy corrected data for: $r_d = 125\,\mathrm{mm},\ a = 150\,\mathrm{mm}$ and $f = 0.2\,\mathrm{Hz}$.

3.4.2 Filtering

To filter out the data scatter, the time series was filtered using the software Wavelab 3 [Aalborg University, 2021]. The setting used is a low-pass brick wall filter. This is a filter that passes signal frequencies below a certain threshold and completely attenuates frequencies above the threshold.

A fast Fourier transformation (FFT) is performed on the data to calculate which frequencies the forces in the time series is allocated at. In figures 3.11 and 3.12, the results of the FFT are displayed for the two cases of data showed on figures 3.6 and 3.4. The first figure representing the case where the actuator performed the movement relatively well, the second one where it didn't. The frequencies above 30 Hz did not have any, significant contributions.

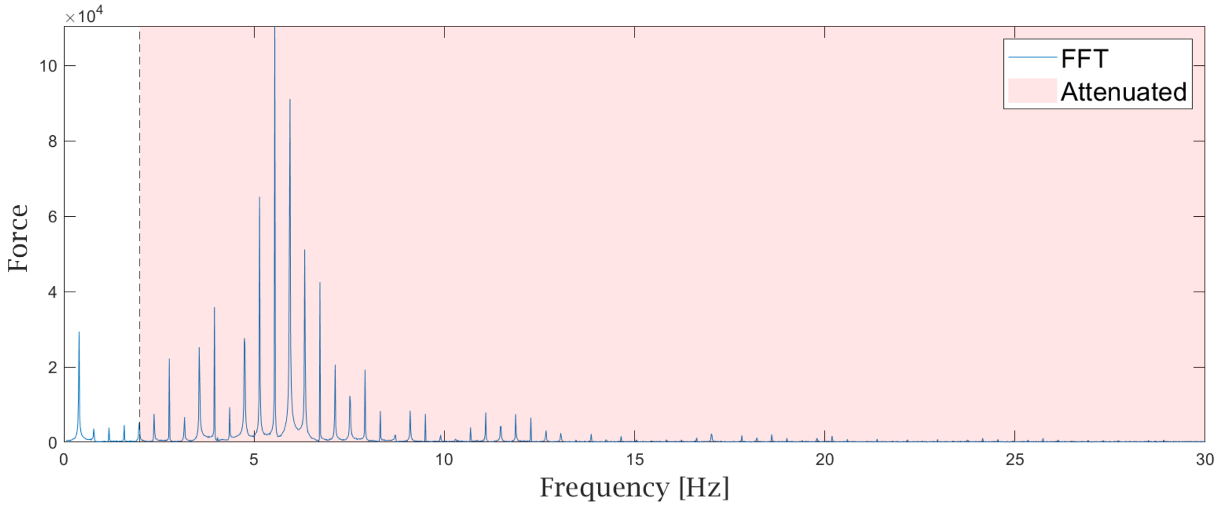

Figure 3.11: FFT analysis of the data for: $r_d = 150\,\text{mm}$, $a = 25\,\text{mm}$ and $f = 0.4\,\text{Hz}$, including the chosen filtering frequency.

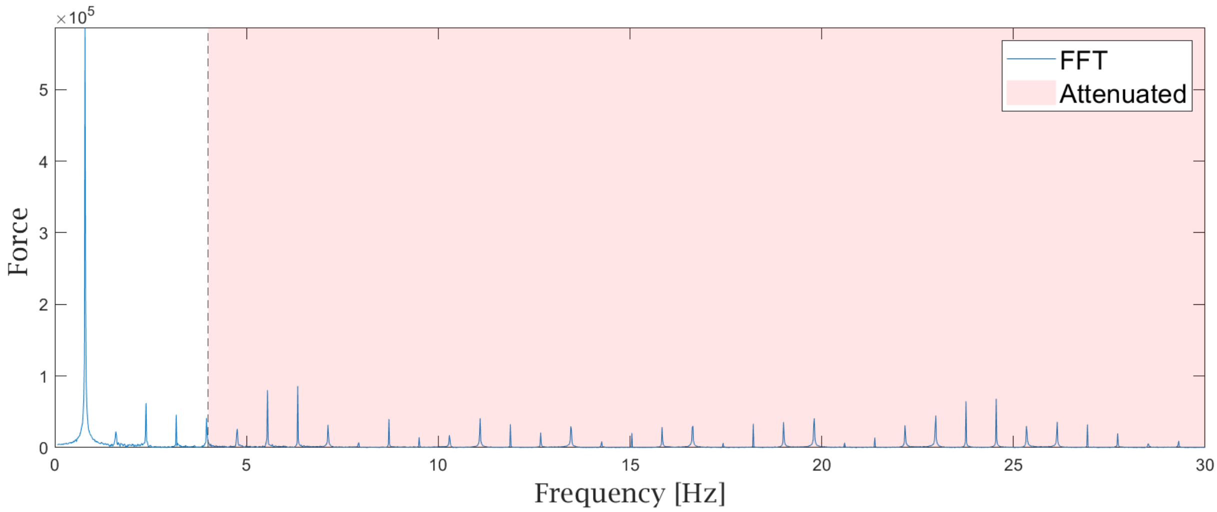

Figure 3.12: FFT analysis of the data for: $r_d = 150\,\text{mm}$, $a = 50\,\text{mm}$ and $f = 0.8\,\text{Hz}$, including the chosen filtering frequency.

For the case displayed in figure 3.12 it is evident that most of the energy is allocated around the oscillation frequency of 0.8 Hz. On the contrary in figure 3.11 most of the energy is allocated in frequencies around 6 Hz which is well above the oscillation frequency of 0.4 Hz.

Since it is improbable for vortex, and turbulence effects in the experiment to induce significant effects at more than five times the oscillatory frequency, the contributions above $5 \times f$ must then be a results of external factors affecting the setup. Most likely they are caused by the actuator motor inducing vibrations.

To exclude effects above five times the oscillatory frequency the filter frequency is set to $1, 2 \ldots 5\,\text{Hz}$ for experiment cases with $0.2, 0.4 \ldots 1\,\text{Hz}$. Results of the two cases after filtering is shown on figures 3.13 and 3.14. The filtering does not filter away all of the scatter in the cases where the actuator did not perform movement very well, but lowering the filter frequency further might cause hydrodynamic effects to be attenuated.

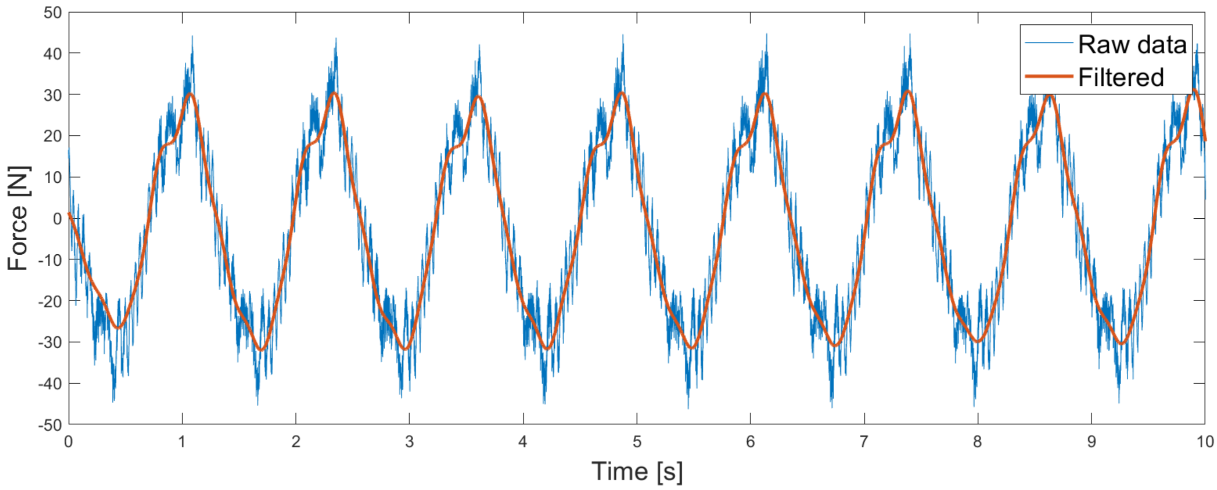

Figure 3.13: Filtered data for: $r_d = 150\,\text{mm},\ a = 50\,\text{mm}$ and $f = 0.8\,\text{Hz}$.

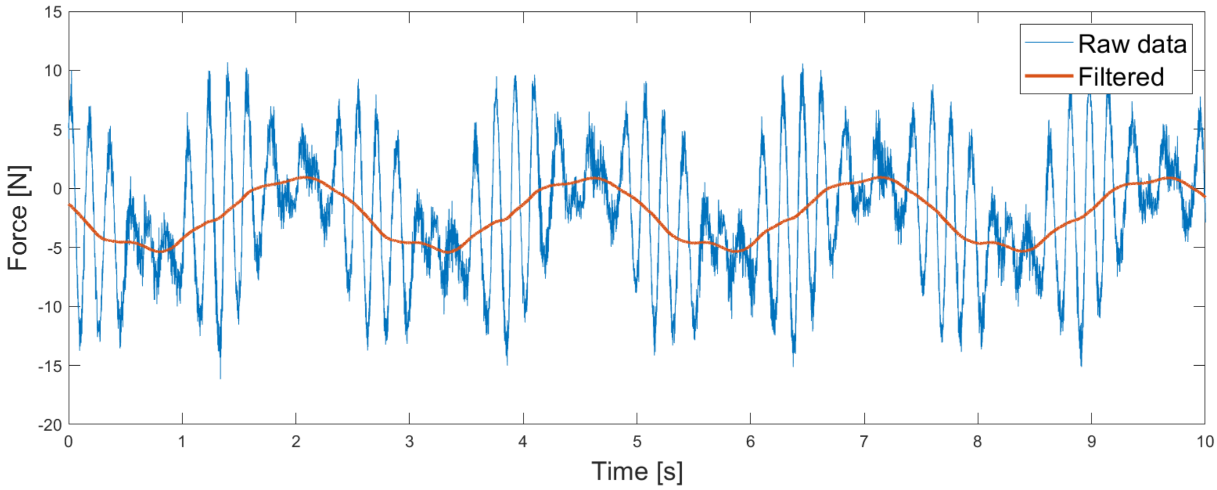

Figure 3.14: Filtered data for: $r_d = 150\,\text{mm},\ a = 25\,\text{mm}$ and $f = 0.4\,\text{Hz}$.

3.5 Observed sources of error

Several sources of error were clear from conducting the experiment: Vibration of the actuator motor, actuator inability to induce correct motion, structural instability and surface disruption. Video examples where the last three effects are clearly visible are available through scanning the QR-codes, or following the links given in figure 3.15.

Actuator inability to induce correct motion.

Structural instability.

Surface disruption.

Figure 3.15: Qr-codes for video examples of the observed sources of error. Hyperlinks for the videos are: `https://youtu.be/SSfeqKsq9iU`, `https://youtu.be/LzR0m05nr6s` and `https://youtu.be/ViAX-REyJ9s` respectively.

Structural instability

When the experimental setup was introduced to combinations of the largest radii, frequencies and amplitudes, the setup started to move horizontally alongside the induced vertical movement. An example of this is shown in the video linked in figure 3.15. The consequence of this being that some experiment cases were not run, or cut short for fear of destroying the setup. This likely happens for one of two reasons. Either because the setup does not have the structural stability to handle the large vertical forces causing some variation of buckling effects, as the actuator pushes the heave plate into the water, initialising a horizontal oscillation. Or because the vertical load is slightly asymmetrical, causing the initiation of the same horizontal oscillation. The main structural weakness off the setup, which might very well be the main cause of this effect, is the piece of plastic with threaded holes at each end, mounted between the actuator rod and the load cell. It was added to the setup to isolate the load cell from most of the vibration coming from the actuator motor. See figure 3.16. An overview of which experiments where stopped short, and which were not performed are shown in tables 3.4 and 3.5.

Figure 3.16: Position of the isolation plastic.

Surface disruption

When performing the experiments with smaller minimum draft, $T_{d,min}$, the surface becomes increasingly more disturbed, the closer to the surface the heave plate moves. Even during the experiments with $T_{d,mean} = 300\,\text{mm}$ disruption of the surface were prominent in the experiments with higher values of r_d, a, and f. Although none of those were as extreme as the experiments where $T_{d,min}$ was reduced. An example of this with $T_{d,mean} = 300\,\text{mm}$ is shown in the video linked in figure 3.15.

Actuator vibration

Very obvious in the data, is the vibration induced by the actuator. It is presumably the source of most of the data scatter, and the main reason filtration of the data is needed. The filtration process in itself is also a source of error. While the filter is chosen as to not exclude eventual important hydraulic effects, there are no guarantee that this is the case.

Actuators inability to induce correct motion

The cases where the actuator did not perform the movement very well induces a major error on those experiment cases. Seemingly this effects occurred only in the cases with low values of f and a, and had a very prominent effect on cases with $a = 25\,\text{mm}$ and $f = 0.4\,\text{Hz}$ in particular. The cases where this effect was noticed visually, are shown in tables 3.4 and 3.5. An example of this is shown in the video linked in figure 3.15. The case showed in the video is worse than what was experienced during data collection, but the principle of the heave plate "shaking" is the same.

To quantify whether this effect is prominent in more cases than what was visually observed, a study of the difference between the target motion and the motion performed by the actuator is carried out.

The actuator has an error on both vertical movement and frequency. In figure 3.17 and 3.18 the specified movement and actual movement are displayed for a case with a lot of shake, and a case with little shake respectively. The error in frequency, as described in section 3.4.1, is small for all the experiments, and does not seem to have a noticeable influence on the results. When comparing vertical movement there are several errors to take into account. According to both figure 3.17 and 3.18 the actual motion is offset below the specified motion for most of the time series. Although this difference seems substantial, especially for 3.17, the difference in amplitude of the specified movement and a sinusoidal function fitted to the actual movement is only 0.5 mm. In addition this difference in offset is not what creates the scatter in the data. It is the variation in the movement at a higher frequency, especially visible between peaks and valleys of the motion.

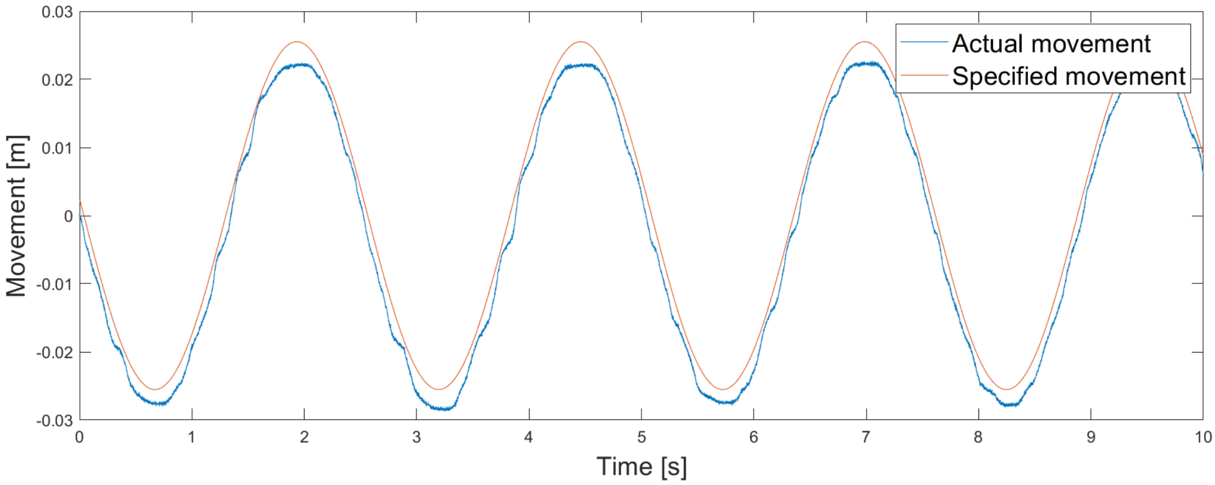

Figure 3.17: The target motion corrected to the performed frequency and the motion performed by the actuator. For the case with $r_d = 150\,\mathrm{mm}$, $a = 25\,\mathrm{mm}$ and $f = 0.4\,\mathrm{Hz}$. The actual movement are off by $a = 2.12\,\%$ and $f = -1.01\,\%$.

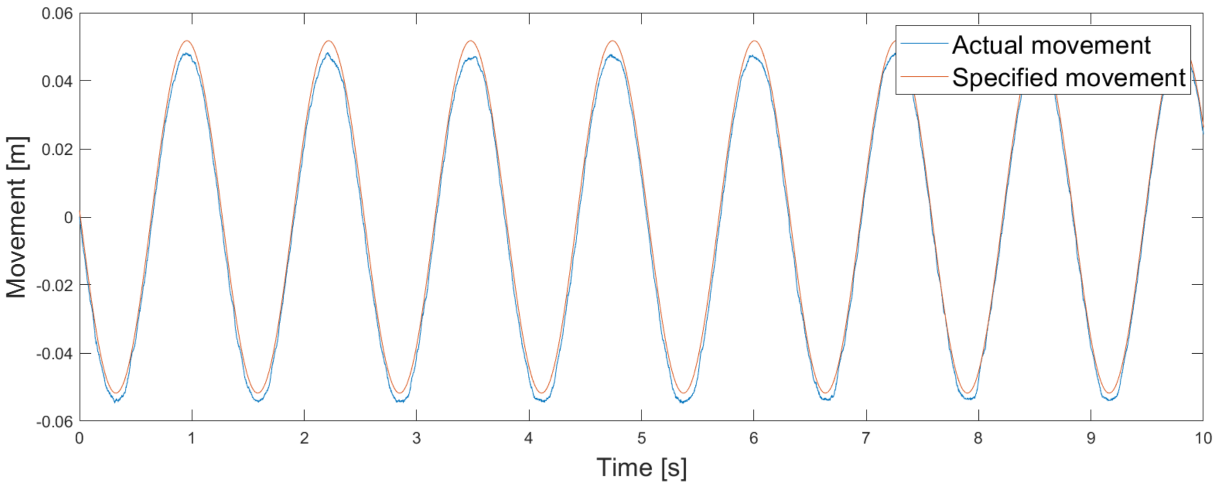

Figure 3.18: The target motion corrected to the performed frequency and the motion performed by the actuator. For the case with $r_d = 150\,\mathrm{mm}$, $a = 50\,\mathrm{mm}$ and $f = 0.8\,\mathrm{Hz}$ The actual movement are off by $a = 3.52\,\%$ and $f = -1.00\,\%$.

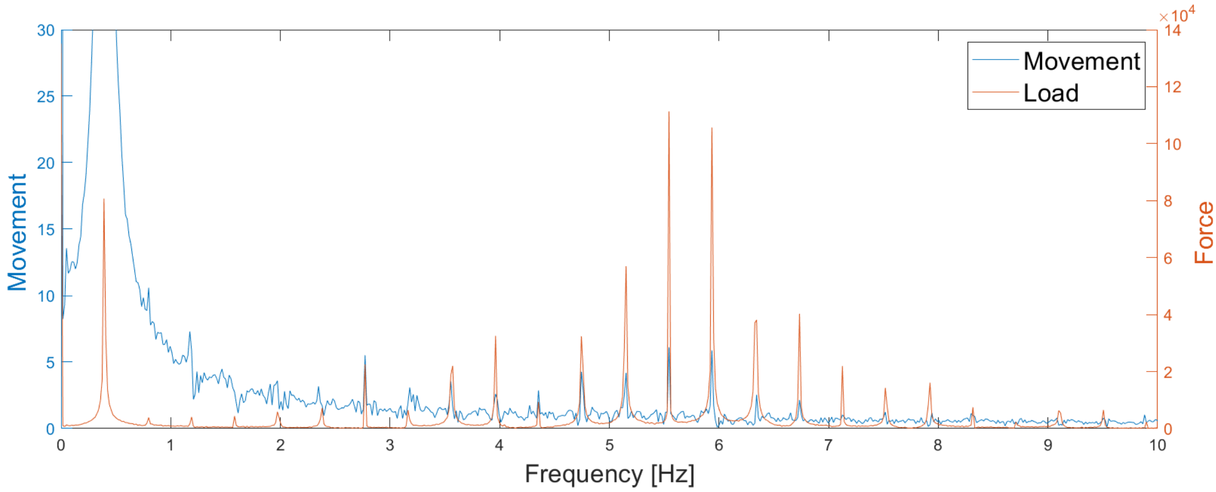

Figure 3.19: FFT of the movement and force output for the case with $r_d = 150\,\mathrm{mm}$, $a = 25\,\mathrm{mm}$ and $f = 0.4\,\mathrm{Hz}$. Movement was not well performed.

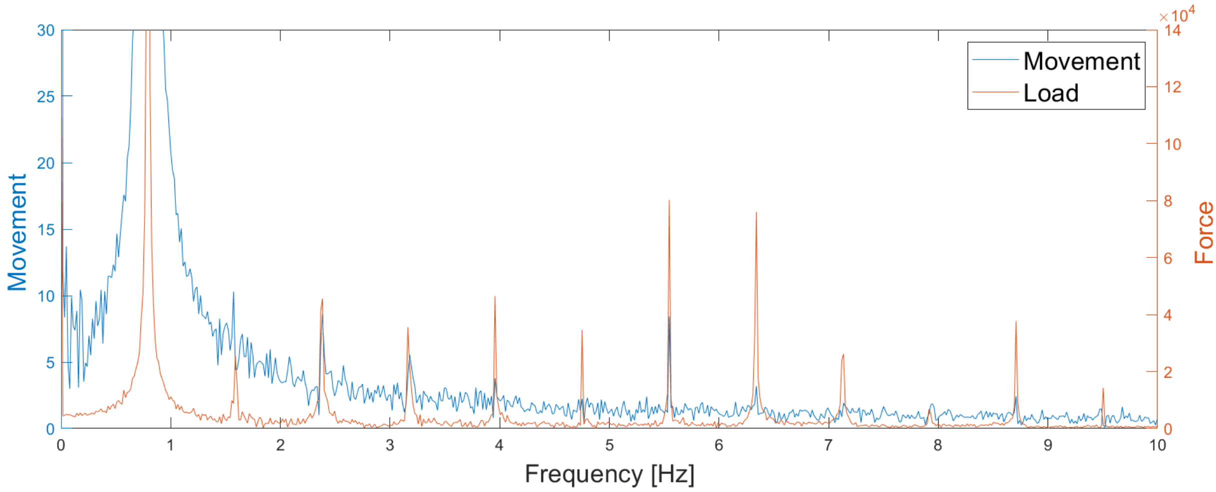

Figure 3.20: FFT of the movement and force output for the case with $r_d = 150\,\mathrm{mm}$, $a = 50\,\mathrm{mm}$ and $f = 0.8\,\mathrm{Hz}$. Movement were performed well.

A more distinct way over observing these motions, and effects, alone are through an FFT analysis of the movement and corresponding force. Such analyses are displayed on figures 3.19 and 3.20 for the two experiment cases.

It is apparent that these relatively small contributions in the movement spectre induces much larger effects in the force spectre. This effect is clearly seen on figure 3.19 where the effects of the "shaking" are larger than that of the oscillation frequency. In figure 3.20, which is a case where the actuator seemingly performed the movement well, the effects are also present. Even though the peaks representing the "shake" are almost the same size, numerically, as the the ones in figure 3.19, the tallest is only 9.3% of the size of the oscillatory frequency peak.

The data from experiments where the "shake" was visibly present are dominated by the forces at frequencies above the oscillatory frequency, and does therefore not show much of the hydraulic effects of the target motion. Even though these effects could be filtered out, the hydraulic effects are for a different motion entirely and there is no way of knowing if the data is reasonably accurate or not. Therefore we have chosen to exclude all data where any peak, in the force FFT, outside the oscillatory frequency, is larger than 50% of the oscillatory frequency peak. The experiments where this is the case is marked with X on tables 3.4 and 3.5.

	$r_d = 100\,\text{mm}$	a [mm] 25	50	100	150
	0.2		X	X	
	0.4	X	X	X	
f [Hz]	0.6	X	X		
	0.8	X			
	1				

	$r_d = 125\,\text{mm}$	a [mm] 25	50	100	150
	0.2	X	X	X	
	0.4	X	X		
f [Hz]	0.6	X			
	0.8				
	1				

	$r_d = 150\,\text{mm}$	a [mm] 25	50	100	150
	0.2	X	X	X	
	0.4	X	X		
f [Hz]	0.6	X			
	0.8				
	1				

	$r_d = 175\,\text{mm}$	a [mm] 25	50	100	150
	0.2	X	X	X	
	0.4	X			
f [Hz]	0.6				
	0.8				
	1				

	$r_d = 200\,\text{mm}$	a [mm] 25	50	100	150
	0.2	X	X	X	
	0.4	X			
f [Hz]	0.6	X			
	0.8				
	1				

Table 3.4: Overview of the observed sources of error, for experiment cases with $T_{D,mean} = 300\,\text{mm}$. Blue denoting experiments where visually it seemed like the actuator did not perform the movement very well. Yellow denoting experiments stopped short due to risk of structural failure. Red denoting experiments not performed due to risk of structural failure. Green denoting experiments without any visual implications. Experiments marked with X denotes experiment data which will not be used because of the actuators inability to induce the correct motion.

	$T_{d,min}$ [mm]	15		10		5	
	a [mm]	0.05	0.1	0.05	0.1	0.05	0.1
	0.2	X	X	X	X	X	X
	0.4	X		X		X	
f [Hz]	0.6						
	0.8						
	1						

Table 3.5: Overview of the observed sources of error, for experiment cases with varying values of $T_{D,min}$ and $r_d = 150\,\text{mm}$. Blue denoting experiments where the actuator did not perform the movement very well. Red denoting experiments not performed due to risk of structural failure. Green denoting experiments without any visual implications. Experiments marked with X denotes experiment data which will not be used because of the actuators inability to induce the correct motion.

3.6 Added mass, drag coefficient and force amplitudes for experiment

Force amplitude, drag coefficients and added mass are found for the force time series. Added mass and drag coefficients are found following the method described in Appendix B. The force amplitude, F_{Amp}, of each configuration of the experiment is found as:

$$F_{Amp} = \frac{F^{+}_{mean} - F^{-}_{mean}}{2} \tag{3.5}$$

With F^{+}_{mean} and F^{-}_{mean} being the mean values of the positive and negative peaks respectively, a visual representation is shown on figure 3.21.

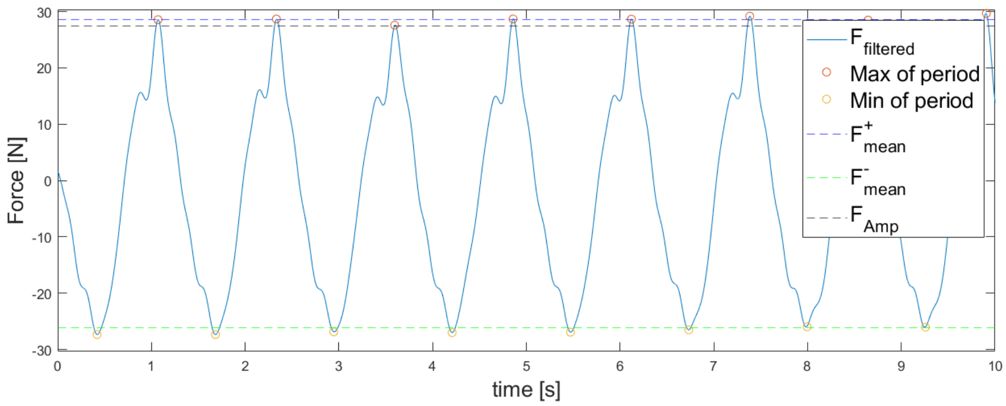

Figure 3.21: Force amplitudes for the case with $r_d = 150\,\text{mm}$, $a = 50\,\text{mm}$ and $f = 0.8\,\text{Hz}$.

The resultant added mass, drag coefficient and force amplitude for the ordinary experiments with $T_{d,mean} = 300\,\text{mm}$ is shown in section 3.6.1. Likewise the results for the experiments with varying minimum draft is shown in section 3.6.2.

3.6.1 Results for ordinary experiments

Added mass, linearised damping and the force amplitude F_{Amp} is displayed for the conducted experiments with $T_{d,mean} = 300\,\text{mm}$ in figures: 3.22, 3.23 and 3.24 respectively.

Following the theory described in chapter 2.1. Added mass is uncorrelated to changes in frequency and amplitude, as it is solely dependant on the geometry of the object, and thereby how the fluid is attached to the object as it moves. In figure 3.22 the added mass for each experiment configuration is shown. r_d is kept constant and each amplitude is shown as a function of the frequency. According to the results from the discs with radius 100 and 125 mm it could seem like the added mass might indeed be constant with changes in both amplitude and frequency, but as the radius increases the data become more scattered. Looking at the cases with larger radii, it would seem, that rather than being constant with both a and f, the added mass is only constant with changes in frequency.

Since changing the amplitude of motion, in the experiment, also changes the minimum draft, there is no excluding this as a cause of the change in added mass. In addition to the change in draft, the experiments with larger radii are are naturally subject to more turbulent effects which might have influenced the added mass as well.

As for the added and mass the drag coefficients of the experiment are more scattered than expected. The theory states that the drag coefficient is constant for the shape of the object, and do not depend on either radius, amplitude or frequency. Even though the coefficients are relatively stable with the changing parameters the results for larger amplitudes seem to be consistently lower than for smaller amplitudes. Likewise to the added mass, these inconsistencies might be caused by proximity to the surface, as well as turbulence effects.

The force amplitudes, behave very much as one would expect, larger- radii, oscillation amplitudes and higher frequencies all induces larger loads.

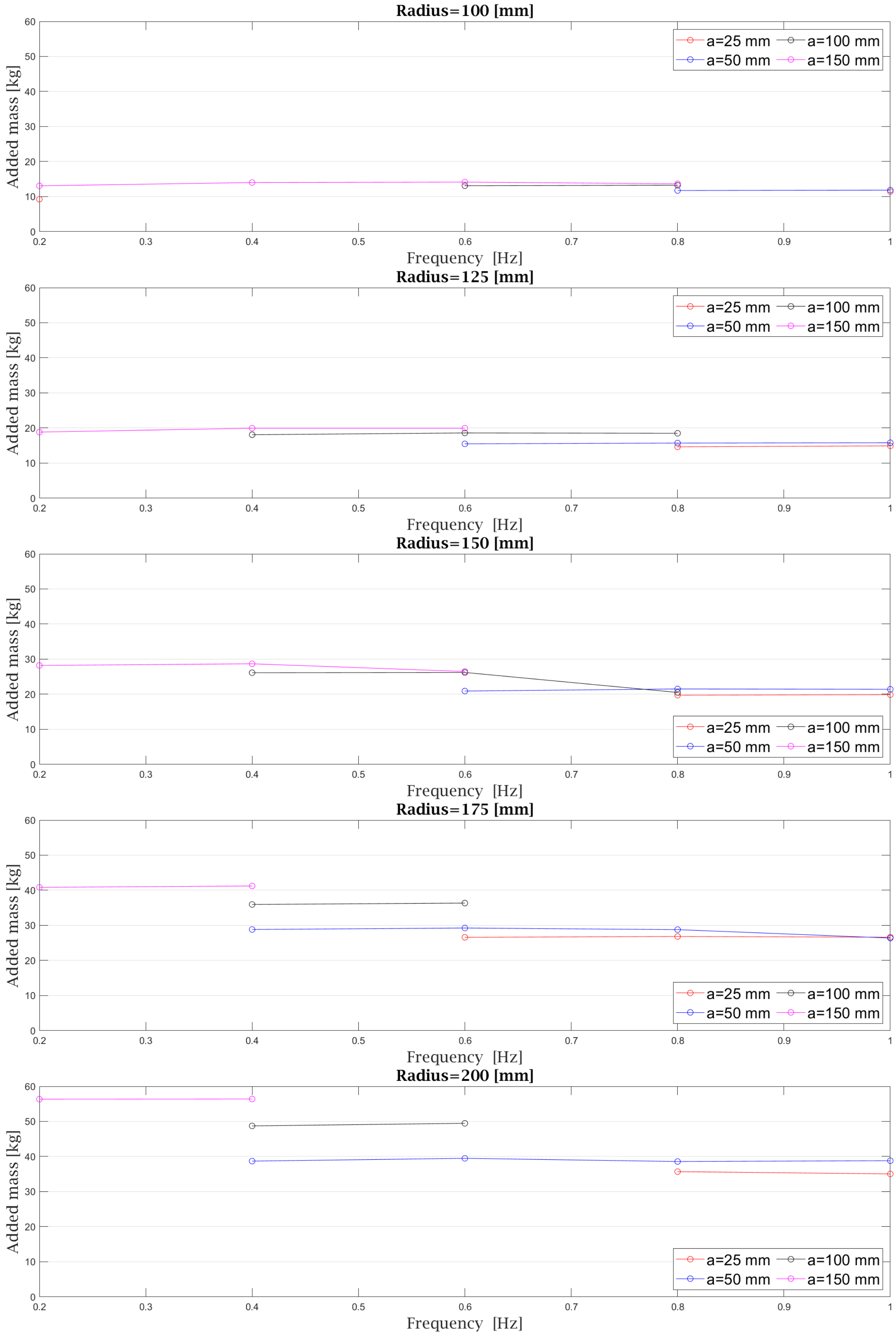

Figure 3.22: Added mass for the conducted experiments with $T_{d,mean} = 300\,\mathrm{mm}$.

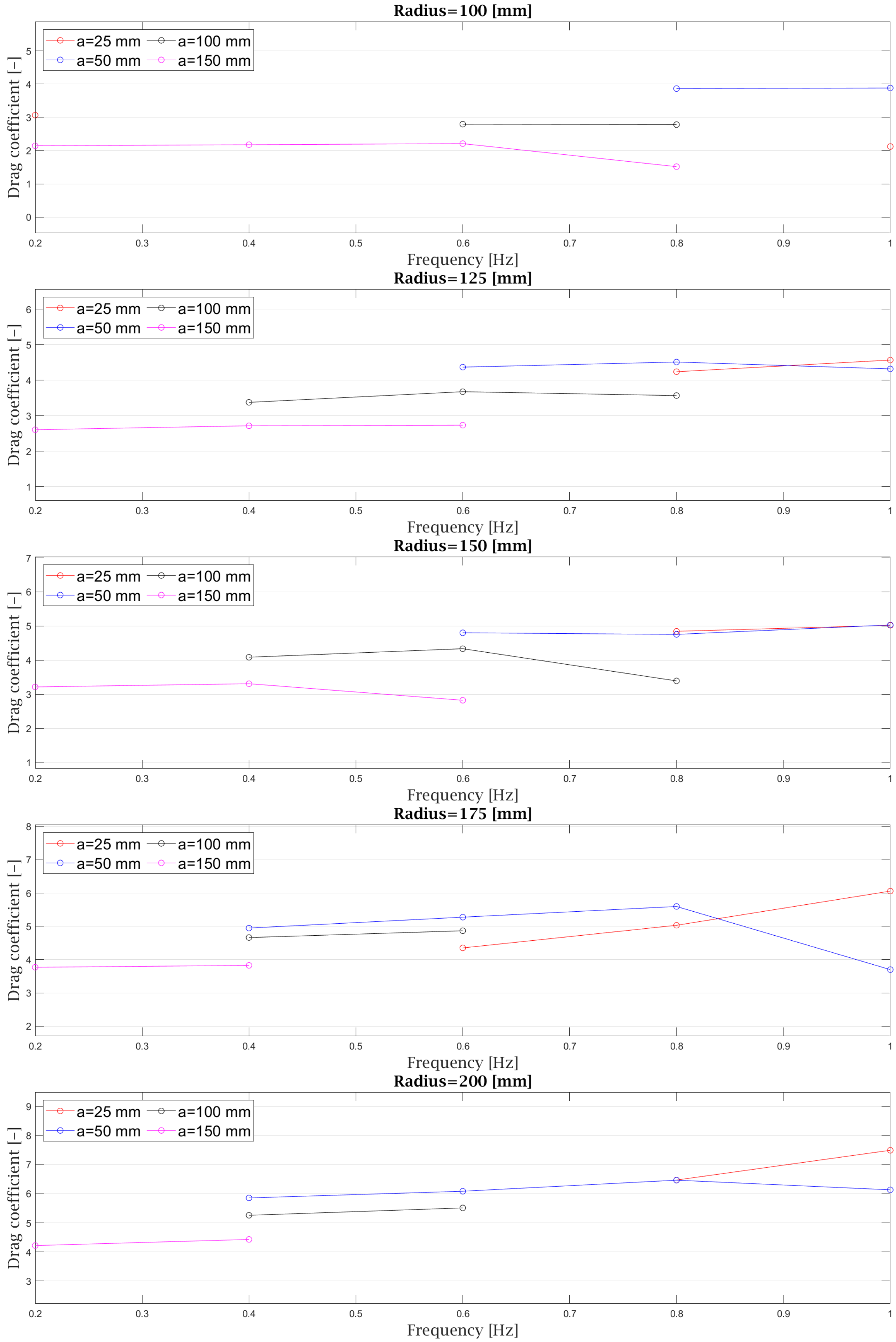

Figure 3.23: Drag coefficients for the conducted experiments with $T_{d,mean} = 300\,\text{mm}$.

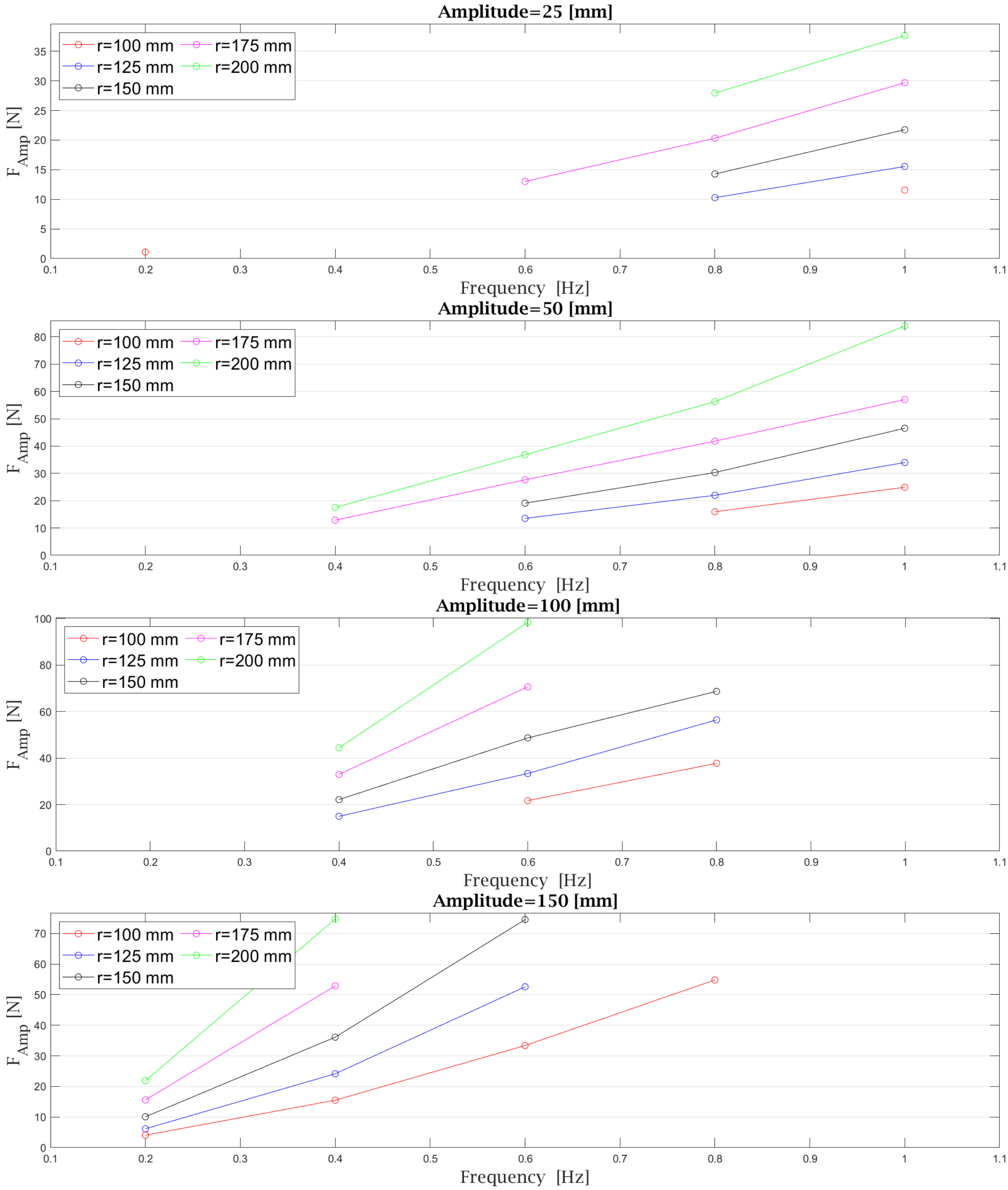

Figure 3.24: Force amplitudes F_{Amp} for the conducted experiments with $T_{d,mean} = 300\,\mathrm{mm}$.

3.6.2 Results for varying minimum draft

Figure 3.25 shows the force amplitude as a function of frequency for the second experimental setup for a disc radius of 150 mm. In the figure two different heave amplitudes are shown, namely an amplitude of 50 mm and 100 mm. Furthermore are three different minimum draft shown, $T_{d,min} = 50$ mm, $T_{d,min} = 100$ mm and $T_{d,min} = 150$ mm. Similar results as for the first experimental setup can be seen in the second experimental setup. Where for the force amplitudes a larger- radii, oscillation amplitudes and higher frequencies all induces larger loads.

Figure 3.26 and 3.27 shows the added mass and and drag coefficient. Here they both seem to be uncorrelated with frequency and the distance to the surface. However as the amplitude increases the added mass and drag coefficient also increases, which again would indicate that there is some correlation.

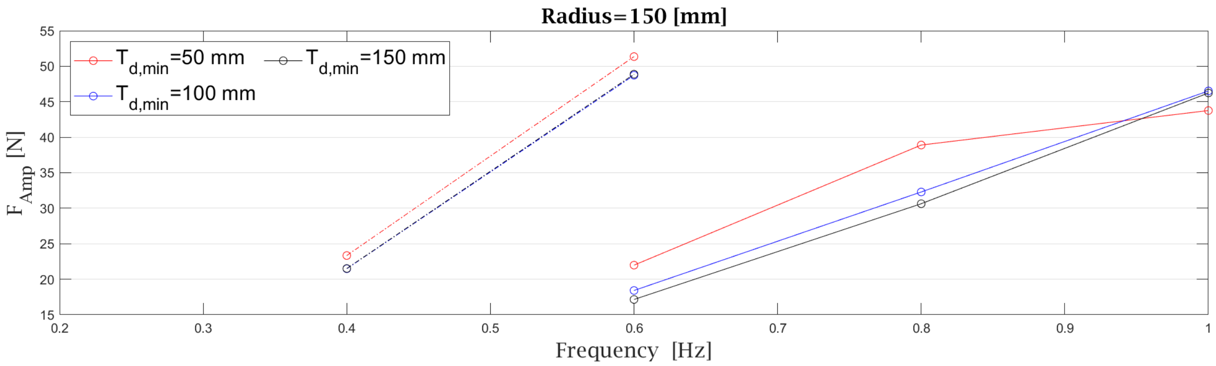

Figure 3.25: Force amplitudes F_{amp} for the conducted experiments with variations of $T_{d,min}$. Solid lines represent $a = 50$ mm dash-dotted lines represent $a = 100$ mm.

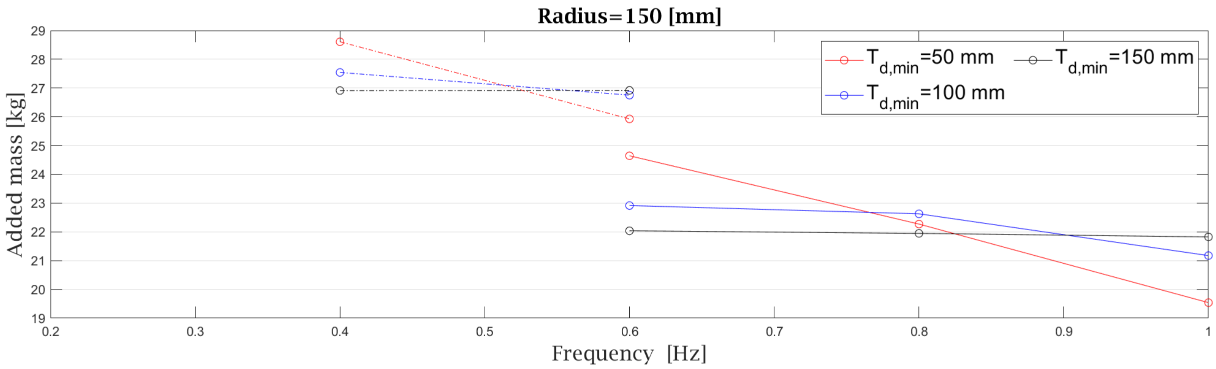

Figure 3.26: Added mass for the conducted experiments with variations of $T_{d,min}$. Solid lines represent $a = 50$ mm dash-dotted lines represent $a = 100$ mm.

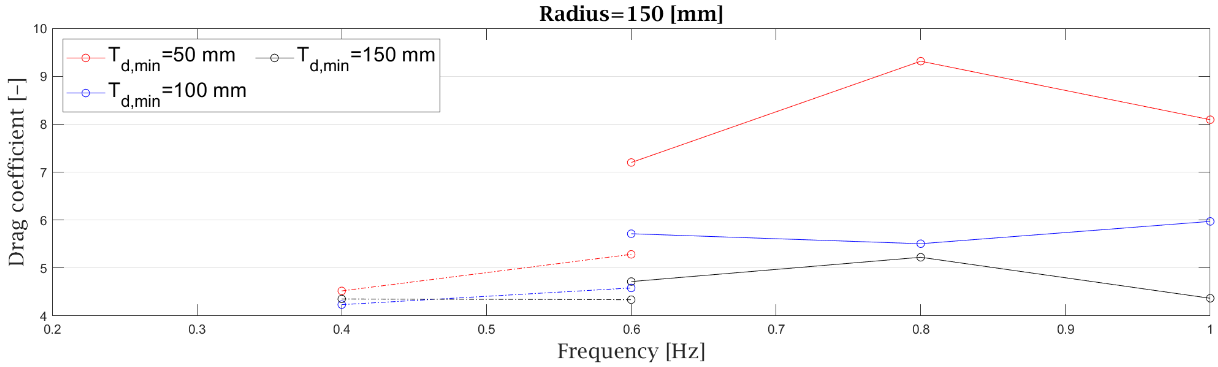

Figure 3.27: Damping coefficient for the conducted experiments with variations of $T_{d,min}$. Solid lines represent $a = 50$ mm dash-dotted lines represent $a = 100$ mm.

SPH Modelling 4

In this chapter the basic principles of SPH modelling are described. A more in-depth explanation of the principles of SPH modeling is given in Appendix A. Furthermore the development process of a representative model for the problem is described and results are shown.

4.1 Principles of SPH modelling

In this project DualSPHysics 5.0 has been used for all instances of computation of SPH models. DualSPHysics is an open-source SPH model solver developed by researchers at the Johns Hopkins University (US), the University of Vigo (Spain), the University of Manchester (UK) and the University of Rome, La Sapienza. Smoothed particle hydrodynamics (SPH) is a method of modelling hydrodynamics. The method discretizes a continuum of fluid at certain interpolation points, also denounced as particles. Each particle has its own set of physical properties: mass, density, velocity and pressure. The discretized Navier Stokes equation is integrated at each particle location according to the physical properties of the surrounding particles. This is done for each time step, and the movement of each particle is found from the updated physical properties of the surrounding particles. DualSPHysics have already proved that its cable of handling advanced applications within the field of Computation Fluid Dynamics. Such as interaction for waves approaching a rubble mound breakwater, where the fluid-structure interaction is modelled with SPH particles between armour blocks that are representative of the real structure [Altomare et al., 2014]. Where the results from the simulation were used to model the armorblocks.

An SPH model is governed by three central equations: The continuity equation, Navier Stokes momentum equation, and the equation of state. The first two are discretized to fit the SPH formulation by a general interpolation function.

A central part of this interpolation function is the smoothing kernel. This kernel is what takes into account the effects of the surrounding particles, and the choice of which kernel function to use is central to results and computation time of the model. The workings of the kernel function is shown on figure 4.1.

The equation of state is the term which relates pressure and density of the particles, taking into account the speed of sound. Although by artificially lowering the speed of sound, the hydrodynamic model becomes weakly compressible resulting in a model which requires less processing power. The incompressibility criterion of the fluid is no longer fulfilled which could impact the accuracy of results. Although as long as the speed of sound is kept above 10 times the largest velocity in the model, density fluctuations are below 1% and the model yields reasonable results.

A visual representation of change in geometry and effect induced from the change of a model defined from solid 3D objects to the particle form can be seen on figure 4.2.

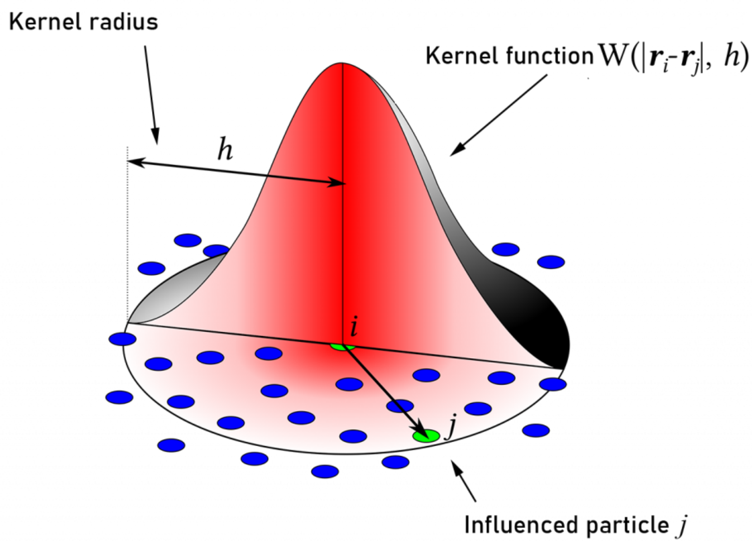

Figure 4.1: Principle the kernel function shown in a 2D environment [Truong et al., 2021].

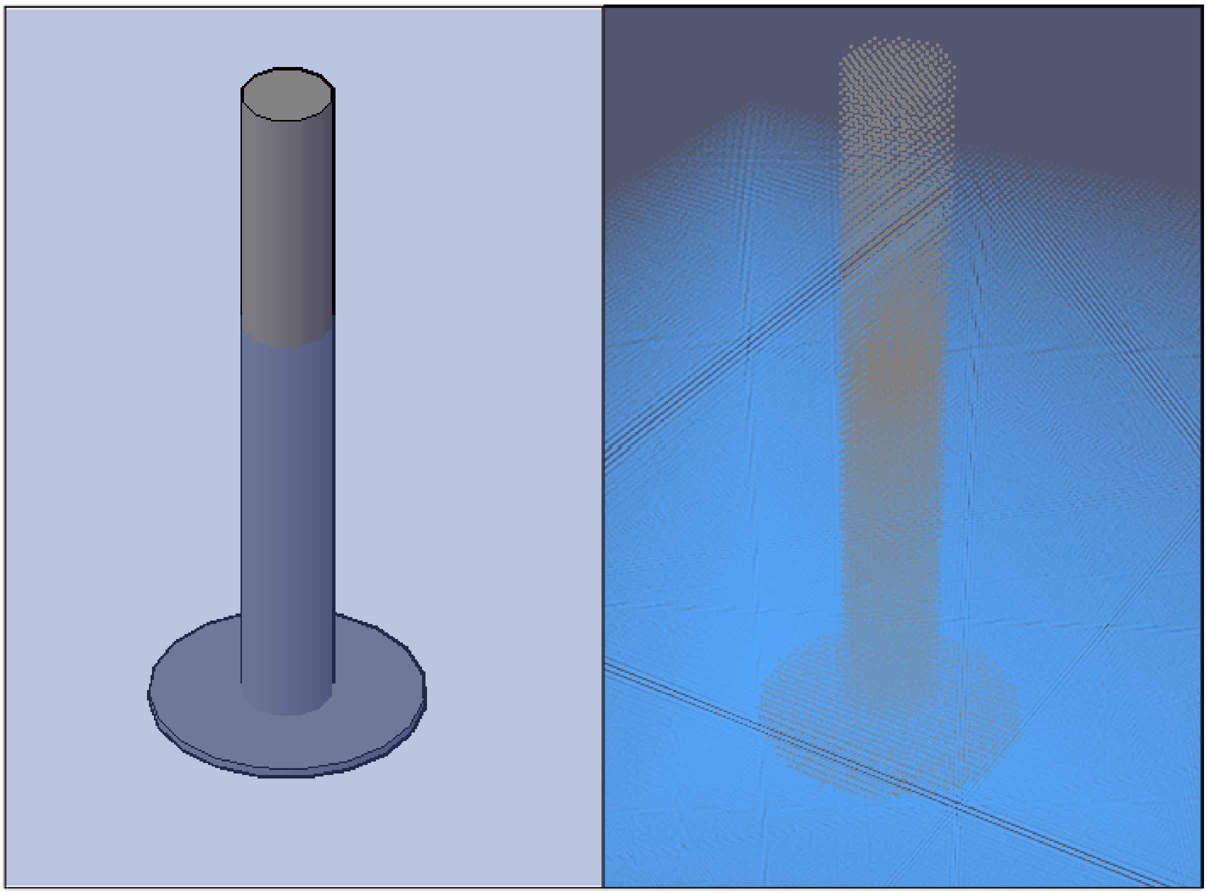

Figure 4.2: On the left is a 3D representation of the constructed model described in section 1.3. On the right is the same model discretized into particles by DualSPHysics. The model has $r_d = 150$mm, $r_c = 50$ mm and a particle size of 10 mm.

4.1.1 SPH Parameters

To run a SPH simulations, values of certain constants and parameters have to be chosen. These constants and parameters are summarised in tables 4.1 and 4.2 respectively. Here values in the source column defines whether the setting was changed from the default value or not. All instances with "Changed" have been modified.

Constants

- g, is the gravitational acceleration and is chosen as the standard value.
- ρ_{p0}, is the reference density of the simulated fluid and is chosen as the density of fresh water. This is done as the experiments was conducted indoors in a freshwater basin.
- h_{swl}, is the maximum still water level in the simulation and is used to calculate the speed of sound, which is needed in the equation of state. This is found by an automated function in DualSPHysics.
- γ, is a poly tropic constant for water used in the state of equation and is normally set to 7 for water as recommended in [Domínguez et al., 2021]. And is also the case for this simulation.
- $speedsystem$, maximum speed of the system is auto estimated based on the maximum velocity of a dam break scenario.
- $coefsound$, A sound coefficient used when artificially lowering the speed of sound. It is multiplied with the maximum velocity of the system $speedsystem$ to attain $speedsound$. The value of $coeffsound$ is what makes sure that the speed of sound is minimum 10 times the maximum velocity.
- $speedsound$, Speed of sound to be used in the simulation, this is by default found as the maximum speed of the system multiplyed by the sound coefficient.
- $coefh$ directly influences the smoothing length of particles. Here set to 1.2 increases the smoothing length by 20% from the default 1.0.

Parameters

- One of the parameters thats need to be defined in DualSPHyics is the precision of the particle interaction in the output file. And is simply how precise the particle position is stored in the data file. Here the double precision is chosen which is the most accurate and also the default in DualSPHyics.
- Another parameter that needs to be defined is the step algorithm the program should use. In DualSPHyics two step algorithms, Verlet and Symplectic, is integrated in the code and are briefly explained in appendix A. Symplectic is more computational demanding, but more precise. Since the symplectic time step algorithm require half time steps, where the verlet does not. Since no study was conducted on this, the symplemectic step algorithm was chosen for the higher accuracy.
- The interaction kernel function is a definable parameter in DualSPHyics, however only two functions are integrated in the code. The two kernel functions are Cubic Spline and Wendland, both are explained in appendix A and can be seen visualised in figure 4.3. The figure shows the kernel functions as a function of the dimensionless variable $q = r/h$, with h being the smoothing length and r being the distance from the particle. Here only particles within 2q of the central particle contribute to the smoothing kernel, which is spherically symmetric and smoothly differentiable for all r. It makes sense to restrict the kernel to this, given that (for purely hydrodynamical quantities) long range forces are negligible [Monaghan, 2005]. For this study the default option in DualSPHyics is chosen, which is the Wendland kernel function.

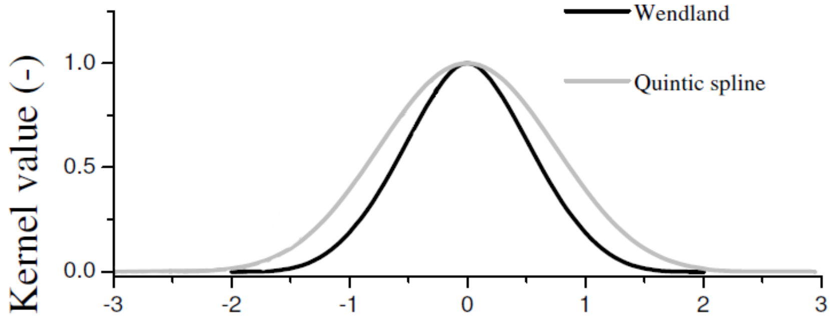

Figure 4.3: The Wendland kernel, Quintic spline plotted as a as a function of the dimensionless variable q. The smoothing lengths and kernel peaks are set to one.

.

- DualSPHysics has two methods of handling viscosity: artificial viscosity, and laminar viscosity and sub particle scale turbulence. Artificial viscosity has been used for all cases presented in this chapter.
- For the density diffusion term there is multiple choices integrated in the dualSPHyics code. The density diffusion are described further in appendix A. In this project the Fourtakas (Full) formulation was used. It is a correction to the more well known DDT developed by Molteni.

Index	Value	Definition	Source
g	$-9.81\,\mathrm{m/s^2}$	Gravitational acceleration	Default
ρ_{p0}	$1\,000\,\mathrm{kg/m^3}$	Reference density of the fluid	Default
h_{swl}	auto	Maximum still water level	Default
γ	7.0	Polytropic constant for water used in the state equation	Default
speedsystem	auto	Maximum system speed (by default the dam-break propagation is used)	Default
coefsound	20	Coefficient to multiply speedsystem	Default
speedsound	auto	Speed of sound to use in the simulation (by default speedofsound=coefsound*speedsystem)	Default
coefh	1.2	Coefficient to calculate the smoothing length ($h = \text{coefh}\sqrt{3p_d^2}$ in 3D)	Changed

Table 4.1: SPH constants.

Value	Definition	Source
1	Precision in particle interaction 0: Simple, **1: Double**, 2: Uses and saves double	Default
2	Step Algorithm 1: Verlet, **2: Symplectic**	Changed
2	Interaction Kernel 1: Cubic Spline, **2: Wendland**	Default
1	Viscosity formulation **1: Artificial**, 2: Laminar+SPS	Default
0.01	Viscosity value	Default
0	Multiply viscosity value with boundary	Changed
3	Density Diffusion Term 0:None, 1:Molteni, 2:Fourtakas, **3:Fourtakas(full)**	Changed
0.1	DDT value	Default
0	Shifting mode **0: None**, 1: Ignore bound, 2: Ignore fixed, 3: Full	Default
1	Rigid Algorithm **1: SPH**, 2: DEM, 3: CHRONO	Default
0.05	Coefficient to calculate minimum time step	Default
0.0001 s	Initial time step	Default
0.00001 s	Minimum time step	Default
0	Velocity of particles used to calculate DT. 1: All, **0: Only fluid/floating**	Default
10.0 s	Time of simulation	Changed
0.01 s	Time out data	Default
700 kg/m^3	Minimum ρ_p valid (default=700)	Default
1 300 kg/m^3	Maximum ρ_p valid (default=1300)	Default

Table 4.2: SPH execution parameters.

4.2 Computational time of SPH simulations

As briefly mentioned in the introduction the main problem with SPH simulations is the excessively long computational runtimes for large domains. This is the case because as the domain size increase the amount of particles that have to be simulated increase exponentially and therefore also the computational runtime. Similar increase in computational runtimes can be seen when the size of the particle is decreased. To make SPH more versatile for engineering application DualSPHysics 5.0 have implemented a technique that utilizes the Graphics Processing Units. GPUs have in the recent years established themselves as a cheap alternative to the more traditional High Performance Computing for scientific computing and numerical modelling. Furtheremore are GPUs designed to manage huge amounts of data and can run parallel computations. This is implemented in the DualSPHysics code, and in turn reduces the computational time significantly.

Most of the simulations done in this project have been run on a computer with following specs:

- GPU: NVIDIA GeForce RTX 2070 SUPER
- CPU: Amd ryzen 9 3950x 16-core processor 3.49 GHz

In figure 4.4 computational time as a function of particle size can be seen. In this simulation the domain size have been held constant. The figure is made from a 11 s long simulation, and a domain size of 1 m^3.

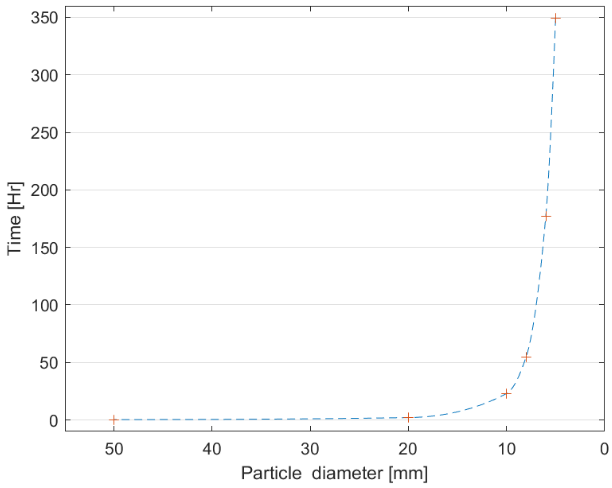

Figure 4.4: Computational time as a function of particle size.

4.3 Influence of wall and bottom proximity, and the size of the particles

To ensure that the model yields results which represents a scenario in open sea, several factors needs to be addressed: The influence of wall proximity, the influence of bottom proximity, and the size of the particles in the model. This is done by doing a convergence study of the added mass, where for each of the cases several simulation have been made.

Close proximity of walls might cause two different effects that can influence the results of the simulation. The first one being the fact that the vertical walls reflects the waves generated by the heave plates movement. When the waves have been reflected and moves back on to the heave plate they might disturb results. The second being the fact that when the heave plate is moving, the displaced water will try to move around it, if the walls are closer to the heave plate the water has a smaller cross section to move through causing an increase in velocity. In turn this increase in velocity causes larger forces to act on the heave plate. The latter of these effects can be caused by the close proximity of the bottom as well.

The influence of particle size is different than the effects of walls and bottom. The SPH concept is build on the assumption that this collection of particles can represent a fluid if the particles are sufficiently small compared to size of the model. In turn it would be optimal in terms of computation time to know when the particles are small enough to accurately represent water in this given scenario.

4.3.1 Model setup

The geometry of the model for the study of the influence of wall and bottom proximity, and the size of the particles is shown on figure 4.5. Here an open box is constructed with a solid bottom and walls to contain the water within. The box' horizontal section is square with side length b. The heave plate consist of a cylinder and a disc, placed in the centre of the box. This design makes it easy to change the parameters, such as the width of the box, height of the water and the size of the particle. The specific changes made is described further in the respective sections below.

The specimen in the centre is subjected to a rectilinear sinusoidal movement and follow the movement graphed on figure 4.6. The figure is shown with an amplitude of 100 mm and a frequency of 0.2 Hz. Due to some uncertainties at the start of the simulation the heave plate will stand still for the first second, this is done to give the particles time to settle before the movement starts. Some data scatter is still present as the heave plate starts to move. To minimise the influence of these uncertainties during data processing, the data from the first seconds of the simulation is excluded. The amount of time excluded depends on the simulated heave frequency. To ease the data processing all the data used from simulations will start from a point where the heave plate is in a downward motion and at the height z=0.

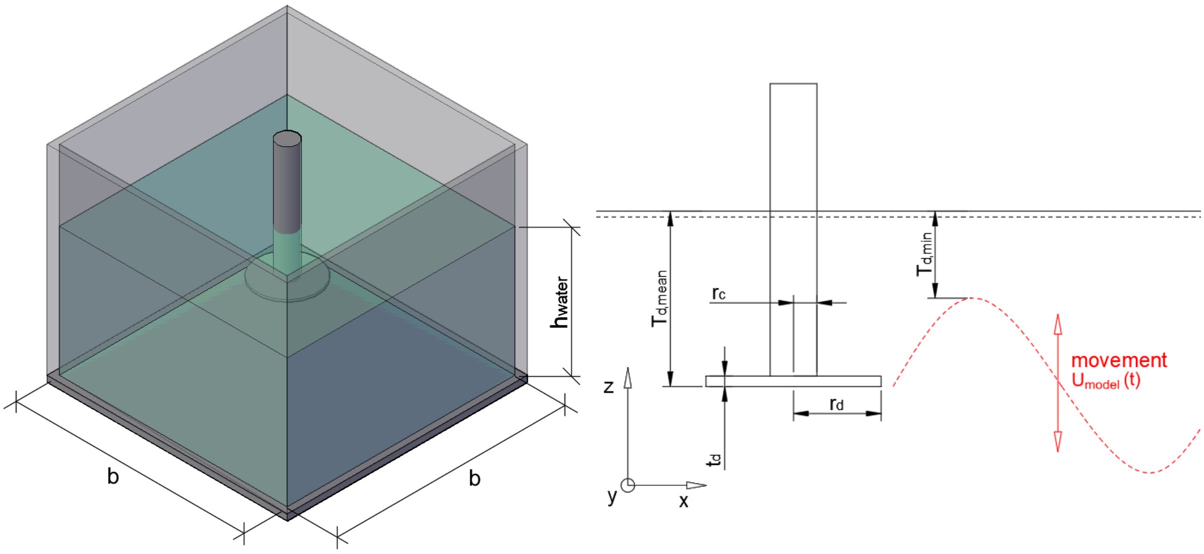

Domain dimensions	
h_{water}	Water depth from bottom to SWL
b	Width of the domain
Heave plate and cylinder	
$T_{d,mean}$	The mean draft from SWL to the bottom of the disc
r_d	Radius of the disc
r_c	Radius of the cylinder
t_d	Thickness of the disc
$U_{model}(t)$	Movement of the disc and cylinder, z=0 at the bottom of the disc

Figure 4.5: Basis for most SPH models used in this project, parameters and specifications of the configuration.

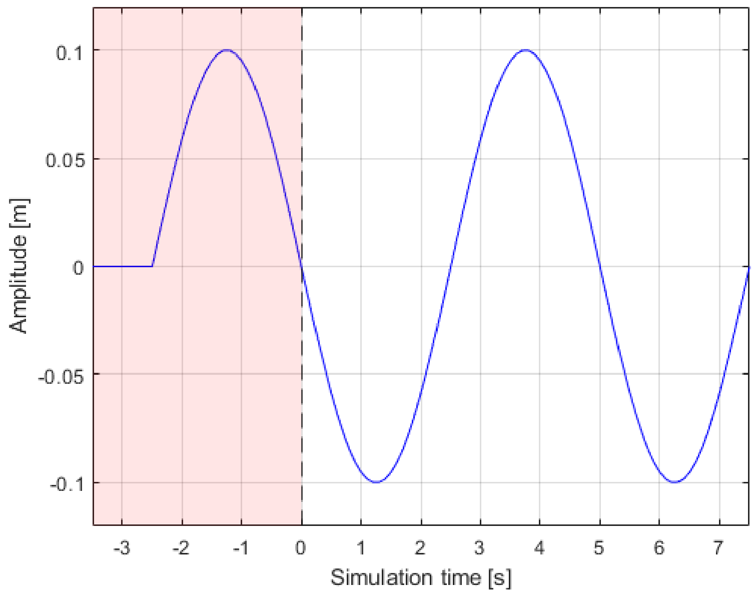

Figure 4.6: The movement induced on the model.

4.3.2 Forces and buoyancy

Forces acting on surfaces are found by splitting the model into groups. An example of this is shown in figure 4.7, where the heave plate and cylinder is split into two groups. This is done to isolate the plate and only extract the forces acting on it, so the data can be easily compared. This is done for all the simulations in this project.

To ease the data processing buoyancy have been subtracted from the results, this is done by taking the mean value for one period and subtracting that value from the total forces. This can be done as long as the heave plate stays submerged.

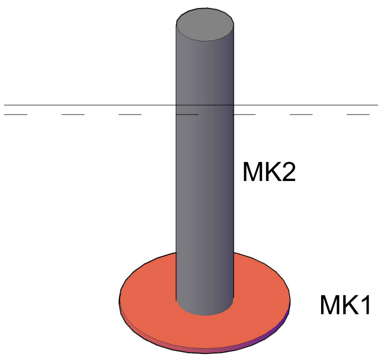

Figure 4.7: Illustration of the heave plate and cylinder. The boundary where forces are extracted are marked with red.

4.3.3 Effects of boundary proximity

To avoid the boundary effects, a model with boundaries far from the heave plate is created. The further the boundaries are from the heave plate the better, but the size is limited by computation time and the combined GPU and CPU memory. A study is therefore carried out with the aim to reduce the domain size. This is done in two parts, one with the aim to reduce the side length b and one to reduce the water depth. Here several simulations for both cases is run. The forces and added mass for each of the simulations are then compared. If changes in boundary proximity does not induce significant changes in force amplitude or added mass, it is assumed that the boundary effects does not influence the heave plate hydrodynamics.

Wall proximity

Five simulations with varying domain width is run. A sketch of the setup is shown in figure 4.8. Parameters and specifications of the simulation configurations is shown in table 4.3. Figure 4.9 shows the time series of the forces acting on the heave plate and the corresponding added mass, where the added mass is calculated as described in Appendix B on page 91. No significant change in forces and added mass are seen as the domain width is decreased, where for the models described in Tabel 4.3 have an average added mass of 41.0 kg.

To ensure there is no boundary effects from the wall proximity for simulations with a higher heave frequency, similar models have been made and the parameters can be seen in Tabel 4.4. The two new models have the same domain size as in model (A) and (C). Figure 4.11 shows the time series of the forces acting on the heave plate, as for the study of lower frequency the forces show no significant change as the domain width is decreased. As there is no significant changes its concluded that models with relatively small domain sizes will yield satisfactory results. However to be on the safe side continued work will be conducted on models with a domain width of 1 000 mm.

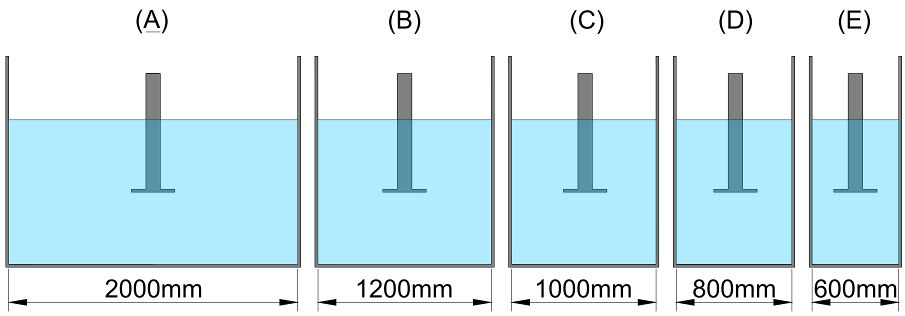

Figure 4.8: Visualisation of the models run to determine effects of wall proximity.

	Simulation				
Basin dimensions	(A)	(B)	(C)	(D)	(E)
Water height (h_{water})	1 000 mm	1 000 mm	1 000 mm	1 000 mm	1 000 mm
Width(b)	2 000 mm	1 200 mm	1 000 mm	800 mm	600 mm
Heave plate and cylinder					
Mean draft (T_d)	500 mm	500 mm	500 mm	500 mm	500 mm
Disc radius (r_d)	150 mm	150 mm	150 mm	150 mm	150 mm
Disc thickness (t_d)	20 mm	20 mm	20 mm	20 mm	20 mm
Cylincer radius (r_c)	50 mm	50 mm	50 mm	50 mm	50 mm
Movement and SPH					
Paticle size	10 mm	10 mm	10 mm	10 mm	10 mm
Amplitude	100 mm	100 mm	100 mm	100 mm	100 mm
Frequency	0.2 Hz	0.2 Hz	0.2 Hz	0.2 Hz	0.2 Hz

Table 4.3: Parameters and specifications of the configuration, the indexes relate to figure 4.5.

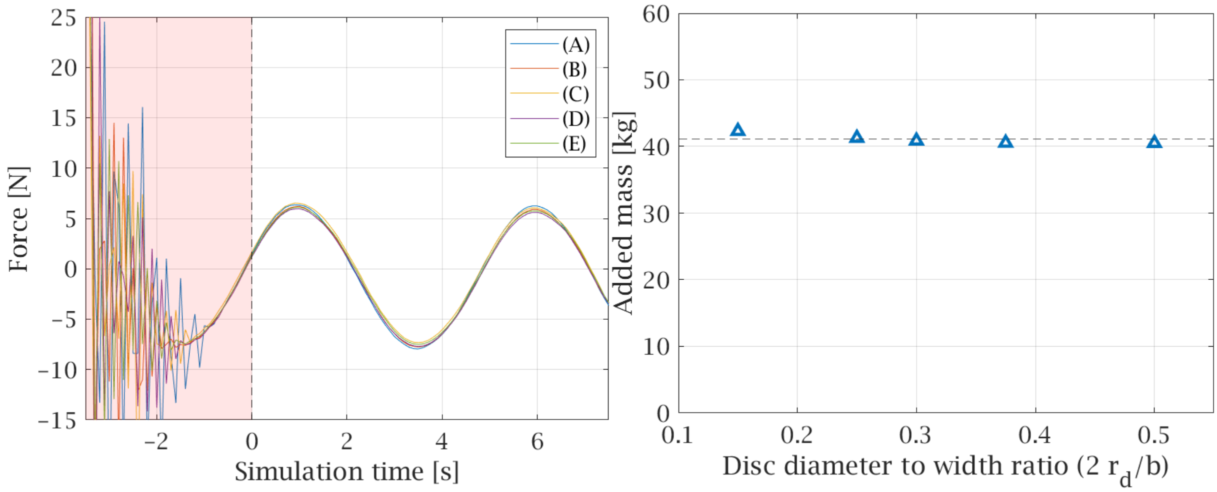

Figure 4.9: Left: Time series of the forces acting on the heave plate. **Right:** corresponding added mass.

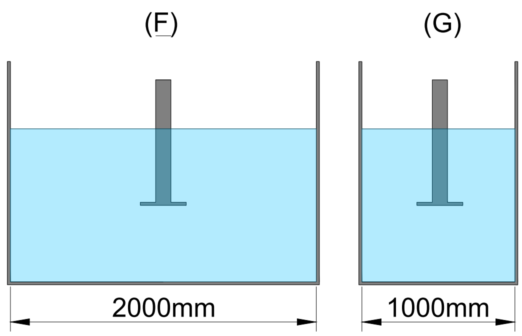

Figure 4.10: Visualisation of the models run to determine effects of wall proximity.

Basin dimensions	**Simulation** (F)	(G)
Water height (h_{water})	1 000 mm	1 000 mm
Width(b)	2 000 mm	1 000 mm
Heave plate and cylinder		
Mean draft (T_d)	300 mm	300 mm
Disc radius (r_d)	150 mm	150 mm
Disc thickness (t_d)	20 mm	20 mm
Cylincer radius (r_c)	40 mm	40 mm
Movement and SPH		
Paticle size	10 mm	10 mm
Amplitude	100 mm	100 mm
Frequency	0.8 Hz	0.8 Hz

Table 4.4: Parameters and specifications of the configuration, the indexes relate to figure 4.5.

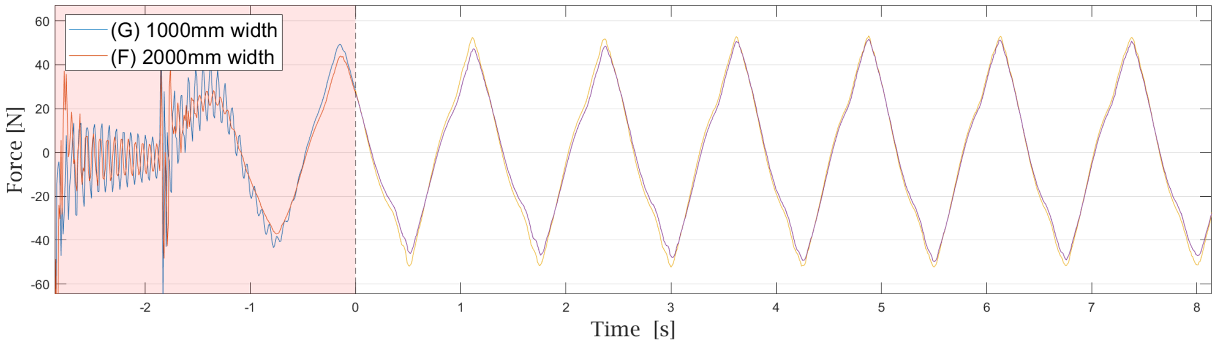

Figure 4.11: Time series of the forces acting on the heave plate, with the configureation described in Table 4.7.

Bottom proximity

In correspondence with the model setup on figure 4.5 and the findings in the study about domain width, three models with varying water depth have been made. These three models are sketched in Figure 4.12, the parameters used are shown in Table 4.5. Figure 4.13 shows the time series of the forces acting on the heave plate and the added mass for each of the models. Added mass is calculated as described in Appendix B on page 91. As for the study of wall proximity no significant changes in the forces and added mass can be seen as the bottom proximity decreases. This indicates that as long as the disc proximity to the bottom is held above 500 mm will there be no influence on the forces from the proximity to the bottom.

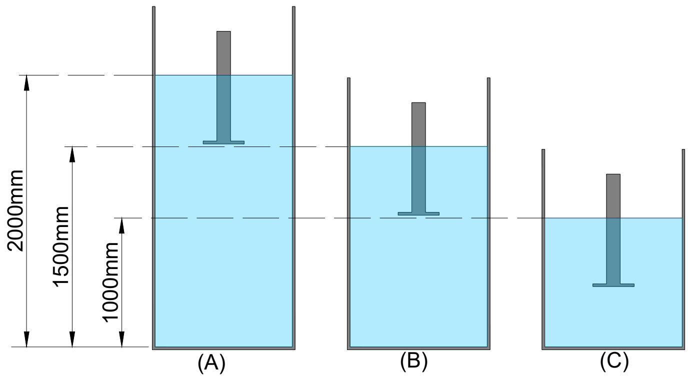

Figure 4.12: Visualisation of the models run to determine effects of bottom proximity.

Basin dimensions	Simulation (A)	(B)	(C)
Water height (h_{water})	2 000 mm	1 500 mm	1 000 mm
Width(b)	1 000 mm	1 000 mm	1 000 mm
Heave plate and cylinder			
Mean draft (T_d)	500 mm	500 mm	500 mm
Disc radius (r_d)	150 mm	150 mm	150 mm
Disc thickness (t_d)	20 mm	20 mm	20 mm
Cylinder radius (r_c)	50 mm	50 mm	50 mm
Movement and SPH			
Paticle size	10 mm	10 mm	10 mm
Amplitude	100 mm	100 mm	100 mm
Frequency	0.2 Hz	0.2 Hz	0.2 Hz

Table 4.5: Parameters and specifications of the configuration, the indexes relate to figure 4.5.

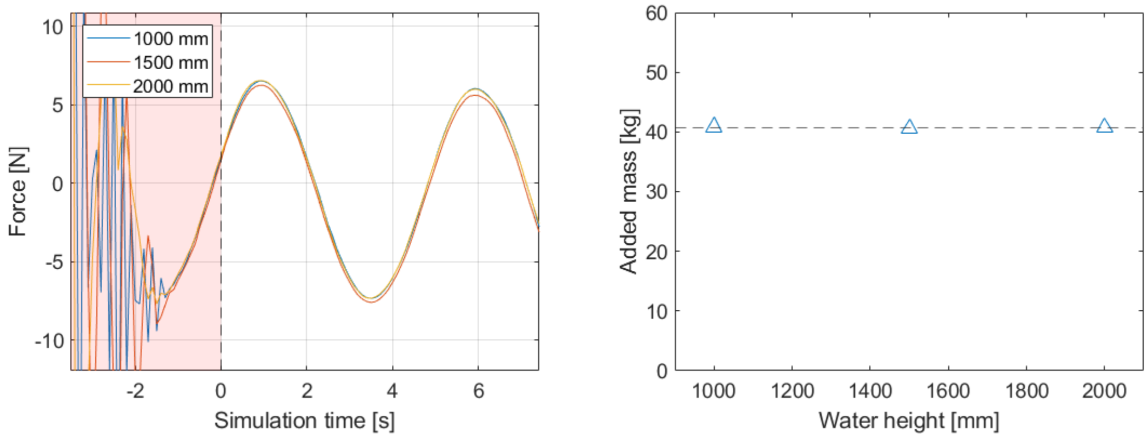

Figure 4.13: Time series of the force (left) and added mass (right). Both displayed for the range of water height used in the study.

4.3.4 Convergence study of particle size

The influence of the the particle size is studied, to ensure the accuracy of the numerical results and to keep the computation time low. In this study, several SPH simulations have been run with varying particle sizes, from large to small, until a convergence have been reached. To keep unforeseen effects at a minimum, the simulation parameters are kept in accordance with the findings from the study on boundary effects. The added mass for each simulation is calculated using the recommended procedure from DNV, described in Appendix B on page 91. The added mass for each simulation is shown in figure 4.14, here some scatter in the results can be seen, however the ones with smaller particle size seems to be converging around an added mass of ≈40 kg. This leads to the conclusion, with some compromise, that simulations with a particle size of 0.01 m diameter will yield satisfactorily results. Its worth noting that the computational time of the simulation with particle sizes of 0.01 m and 0.005 m is respectively 2.3 Hr and 35.0 Hr.

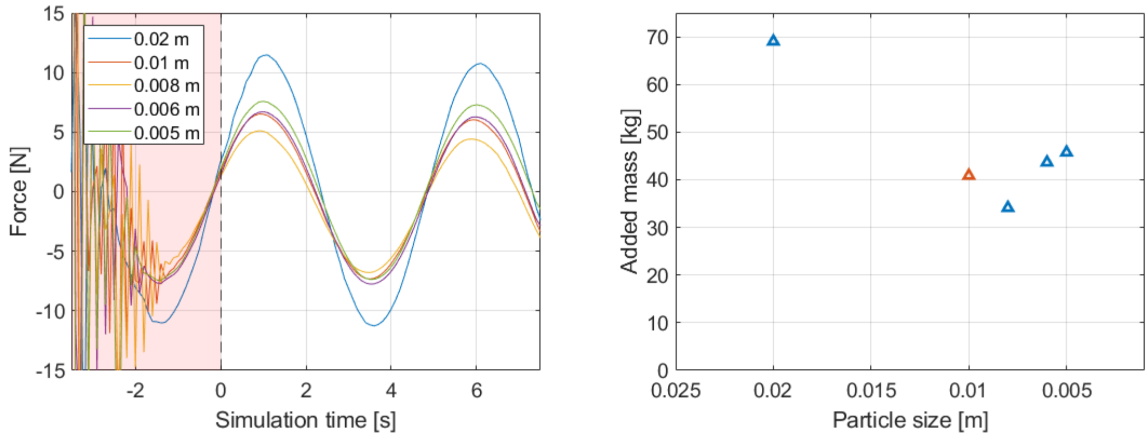

Figure 4.14: Time series of the force (left) and added mass (right). Both displayed for the range of particle sizes used in the study.

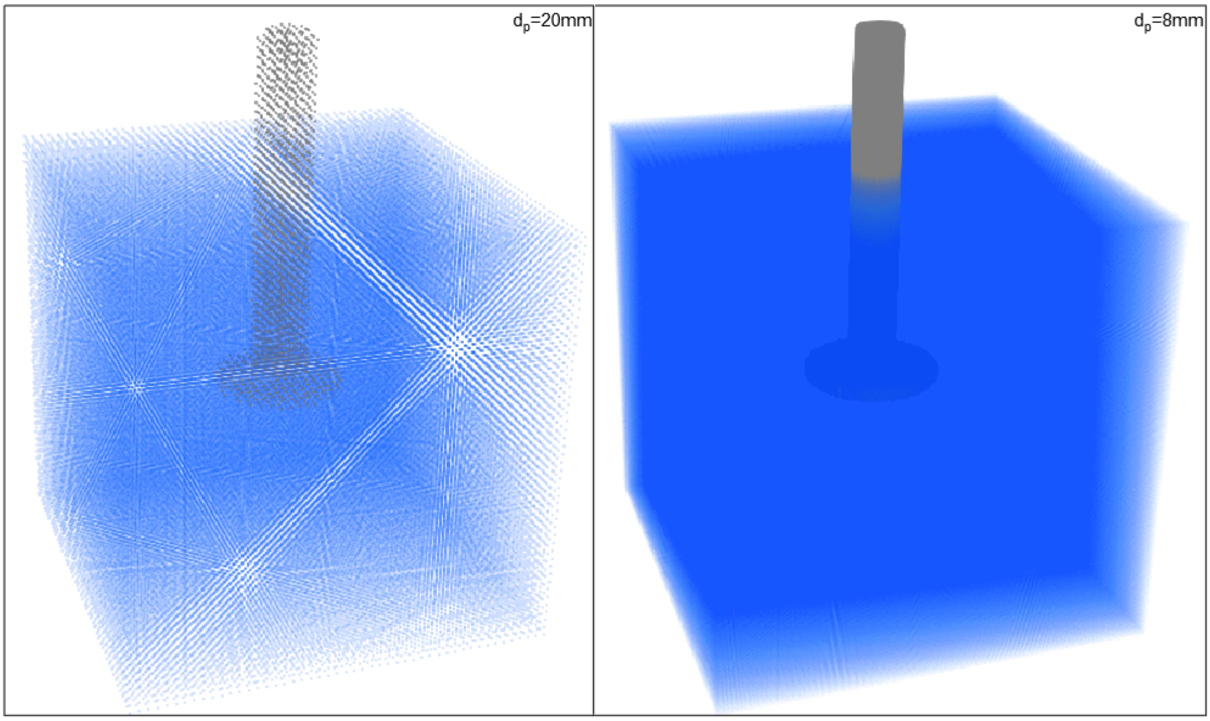

Figure 4.15: Visualisation of the influence of particle size. Where the picture on the left represents a model with an inner particle distance of 20 mm, and the one on the right represent an inner particle distance of 8 mm.

4.3.5 Summary

In summary the parameters found in the influence of wall and bottom proximity studies, and the convergence study of particle size can be seen in table 4.6. These parameters are then used to reconstruct the setup used in the experiment. Notably the frequencies used in the study of influence of the bottom proximity is the lowest frequency used in all the simulations, this is the case because the boundary effects was studied prior to the experiments, and afterwards other SPH simulations was deemed more important. Although as the study of wall proximity influence saw no changes in the forces at higher frequency it is assumed that a water depth of 1 000 mm adequately models the hydrodynamics.

Index	Value	Defination
b, l	1000 mm	Width and length of the domain
h_{water}	1000 mm	Water depth
d_p	10 mm	Diameter of particle

Table 4.6: Parameters used for the simulations.

4.4 SPH model for experiment

This section aims to recreate the cases tested in the experiment using a numerical SPH model. As there is slightly different experimental setups for the tests with constant mean draft and the experiments for varying minimum draft. First a basis for the general numerical model is given, followed by the two specific setups.

4.4.1 Basis for numerical model for experiment

A model in dualSPHysics is constructed to represent the experimental setup described in section 3.1 on page 15. However reconstructing the wave basin with its full size of 13.0 m · 8.5 m · 1.0 m, would not be feasible. This is due to simulating a basin this large would result in a large amount of particles, and with a particle size low enough to get satisfactorily results would yield a too long computational time. Therefore a much smaller basin is constructed, this is done in corresponds with the study conducted in section 4.3, and should not influence the results. The model can be seen in figure 4.16. Identical to the boundary and particle size studies the heave plate and cylinder is placed in the centre of the model and is given a rectilinear sinusoidal movement.

As stated in section 4.3.1 the heave plate starts moving after the first second, this is again done to give the particles time to settle before the movement starts. Additionally scatter in the data at the start of the simulation will be seen when the heave plate starts moving. To minimise the influence of these uncertainties the data from the first few seconds of the simulation excluded.

The force is measured exclusively on the heave plate and the buoyancy is removed from the force, as described in 4.3.2.

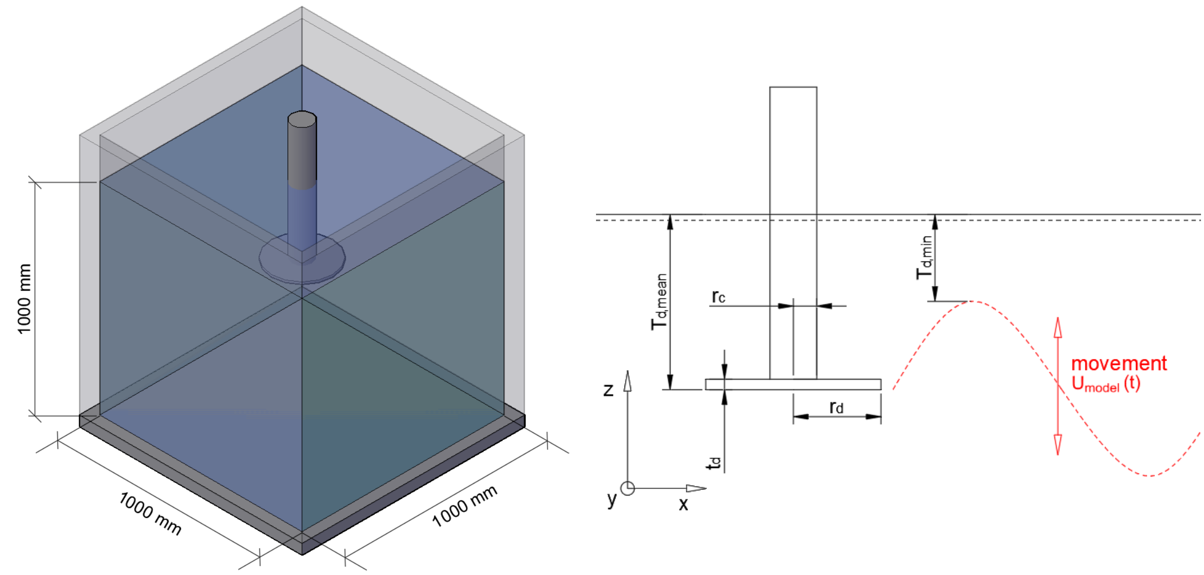

Figure 4.16: Basis for the numerical model.

4.4.2 Simulations with constant mean draft

The first numerical model is used to simulate the same setup as used in the first experiment. The first experiment varied the amplitude, frequency and radius, with constant draft. In total 100 simulations was run with different combinations of heave amplitude, heave frequency and radius of the disc. The combinations are described in section 3.2 on page 17. The parameters and specifications of the configuration for the simulations are given in Table 4.7

Basin dimensions	
Water height (h_{water})	1 000 mm
Width(b)	1 000 mm
Heave plate and cylinder	
Mean draft (T_d)	300 mm
Disc radius (r_d)	[100 mm; 125 mm; 150 mm; 175 mm; 200 mm]
Disc thickness (t_d)	18 mm
Cylincer radius (r_c)	40 mm
Movement and SPH	
Paticle size	10 mm
simulation time	11 s
Amplitude	[25 mm; 50 mm; 100 mm; 150 mm]
Frequency	[0.2 Hz; 0.4 Hz; 0.6 Hz; 0.8 Hz; 1.0 Hz]

Table 4.7: Parameters and specifications of the configuration, the indexes relate to figure 4.5, where the brackets, [ ], indicate the varying parameter.

4.4.3 Varying minimum draft

The second numerical model is used to simulate the experiment conducted on varying minimum draft. The goal is to simulate the influence of the surface when the heave plate is moved closer to the surface. This is done by having a constant minimum draft, $T_{d,min}$ and varying the mean draft to fit the oscillation amplitude. Three different minimum draft depth was simulated with two different heave amplitudes. The movement measured from the bottom of the heave plate for the different amplitudes can be seen in figure 4.17.

Only the combinations that gave satisfactorily results in the experiment was simulated .An overview of the simulated cases is shown in table 4.8. The parameters and specifications of the configuration for the simulations are given in Table 4.9

	$T_{D,min}$ [mm]	15		10		5	
	a [mm]	0.05	0.1	0.05	0.1	0.05	0.1
	0.2	X	X	X	X	X	X
	0.4	X		X		X	
f [Hz]	0.6						
	0.8						
	1						

Table 4.8: Overview of the combinations made. Blue and green colour indicate that a experiment was conducted, where the blue colour furthermore indicates an observed error. Red indicate that no simulation nor experiment was conducted. Whereas a cross indicate the data was later discarded. Only the green without crosses are simulated in this study.

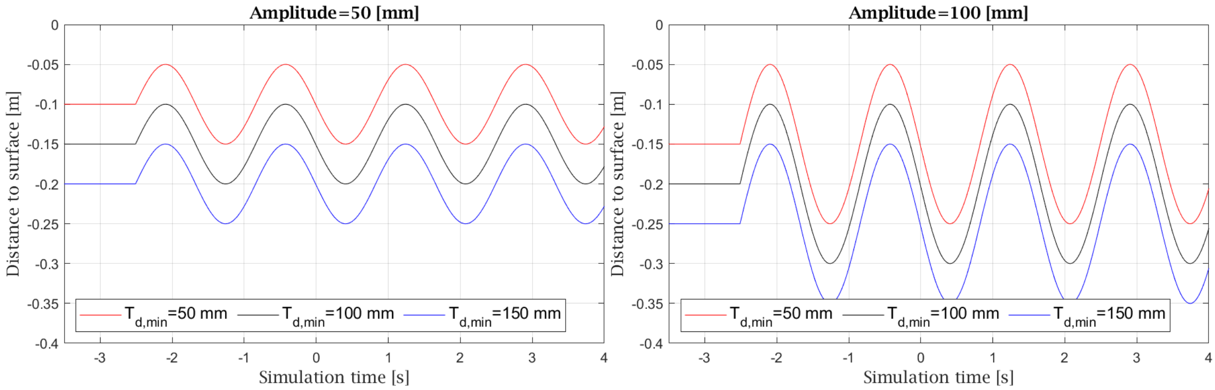

Figure 4.17: Heave plate movement measured from the bottom of the heave plate for different instances of $T_{d,min}$.

Basin dimensions	
Water height (h_{water})	1 000 mm
Width (b)	1 000 mm
Heave plate and cylinder	
Mean draft (T_d)	[50 mm; 100 mm; 150 mm]
Disc radius (r_d)	150 mm
Disc thickness (t_d)	18 mm
Cylincer radius (r_c)	40 mm
Movement and SPH	
Paticle size	10 mm
Amplitude	[50 mm; 100 mm]
Frequency	0.6 Hz

Table 4.9: Parameters and specifications of the configuration, the indexes relate to figure 4.5, where the brackets, [ ], indicate the varying parameter.

4.5 Added mass, drag coefficient and force amplitude

Force amplitude, drag coefficients and added mass are found for the force time series. Added mass and drag is found following the method described in Appendix B. Examples of the fitted curve for the added mass is shown in figure 4.18. The examples shown has $r_d = 150$ mm, $a = 50$ mm, $T_{d,mean} = 300$ mm, and varying frequency. Here the scatter in the data, as mentioned earlier, can be seen in the beginning of the time series. This scatter is discarded and excluded from the fits. The excluded data is indicated by the red zone. This is done for all the numerical simulations and the results are presented below.

Results for the ordinary simulations with $T_{d,mean} = 300$ mm are displayed in section 4.5.1 and results for simulations with varying minimum draft are presented in 4.5.2.

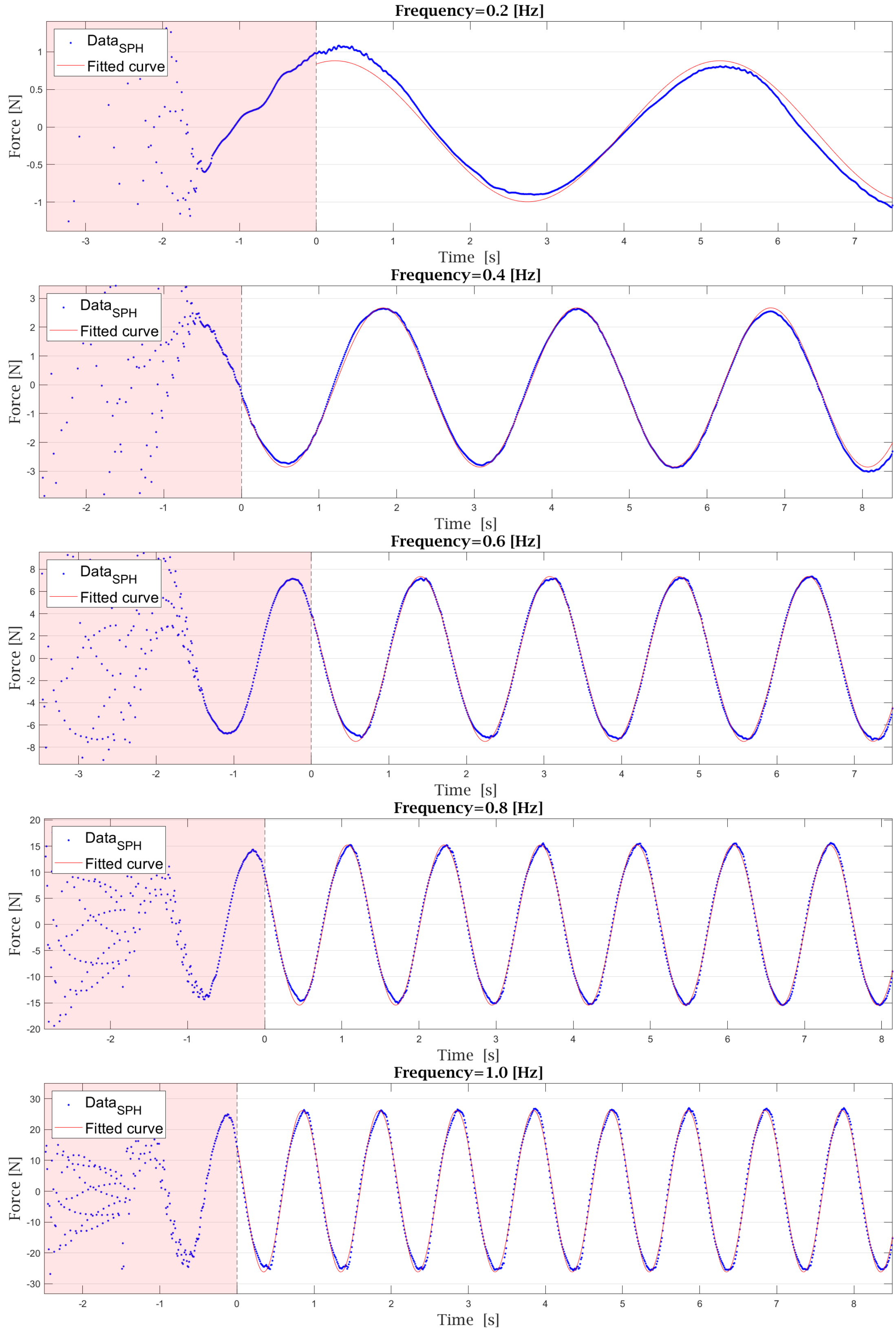

Figure 4.18: Plot of the fitted curve for added mass. All the cases are with $r_d = 150\,\mathrm{mm}$, $a = 50\,\mathrm{mm}$ and $T_{d,mean} = 300\,\mathrm{mm}$. The area marked with red corresponds to the discarded data.

4.5.1 Results for ordinary simulations

Figure 4.19, 4.20 and 4.21 shows, respectively, the added mass, drag coefficients and force amplitude for the models with $T_{d,mean} = 300\,\text{mm}$. For the simulations with a disc radius of $r_d = 100\,\text{mm}$ and $r_d = 125\,\text{mm}$ it seems the added mass and drag coefficient for frequencies above 0.2 Hz are both mostly uncorrelated with amplitude and frequency. However for $r_d = 150\,\text{mm}$, $r_d = 175\,\text{mm}$ and $r_d = 200\,\text{mm}$ it seems that the added mass and drag coefficients increase with the amplitude. For all the cases for frequency, $f = 0.2\,\text{Hz}$, and partly $f = 0.4\,\text{Hz}$, the added mass and drag coefficients respectively are significantly lower or higher than for the rest of the frequencies.

The force amplitudes behave as expected yielding larger forces with increases in a, f and r_d.

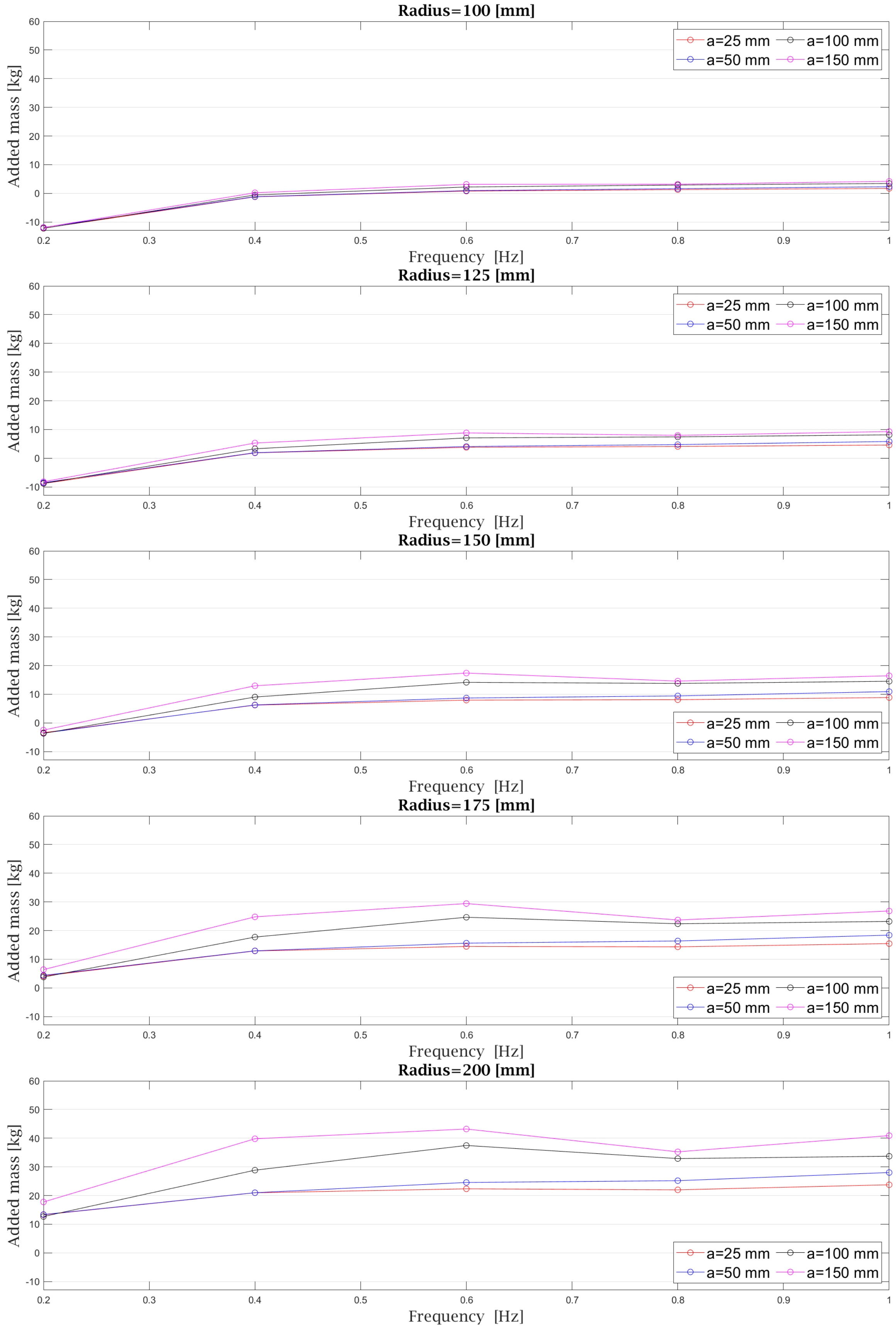

Figure 4.19: Added mass for the modelled cases with $T_{d,mean} = 300\,\text{mm}$.

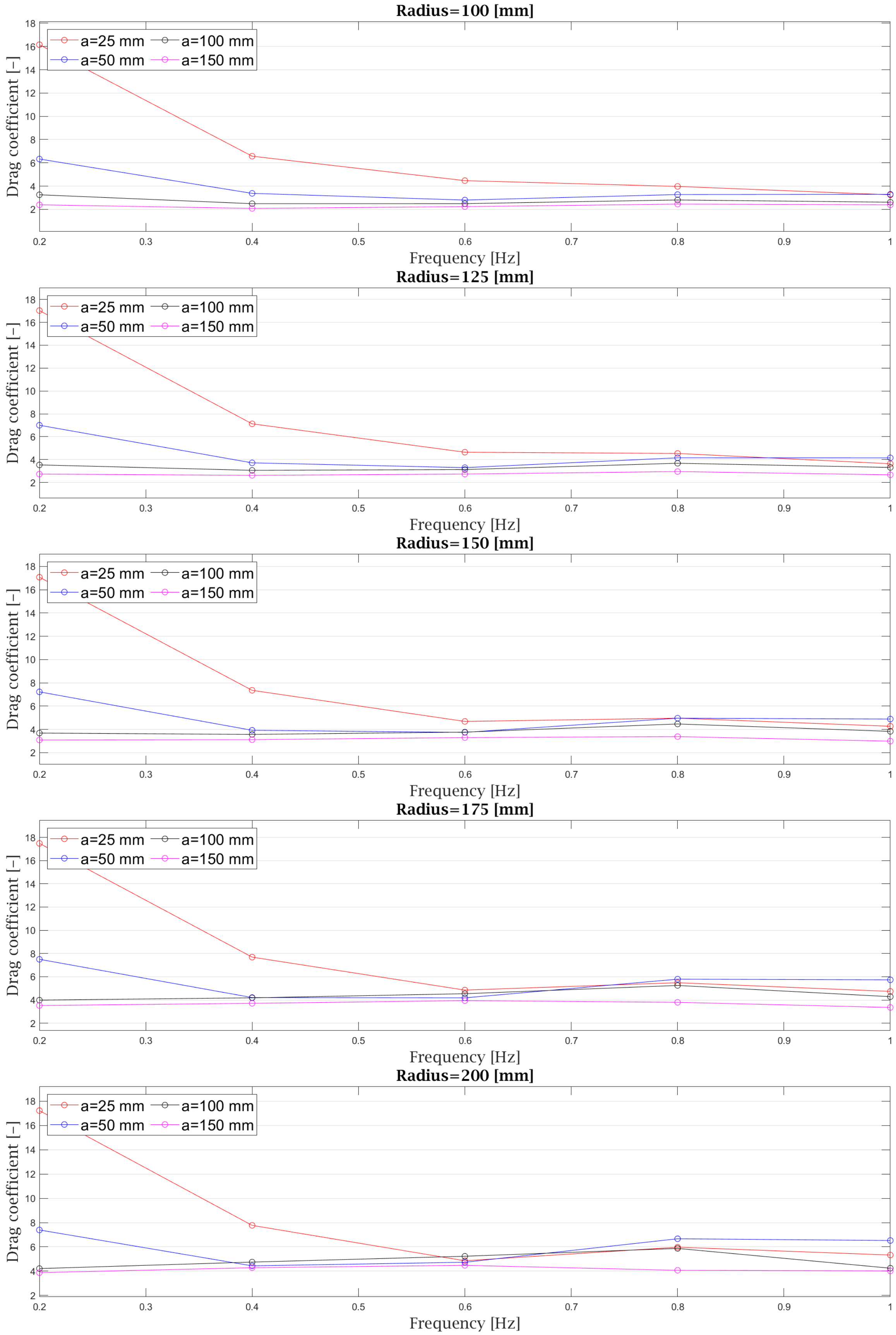

Figure 4.20: Drag coefficients for the modelled cases with $T_{d,mean} = 300\,\mathrm{mm}$.

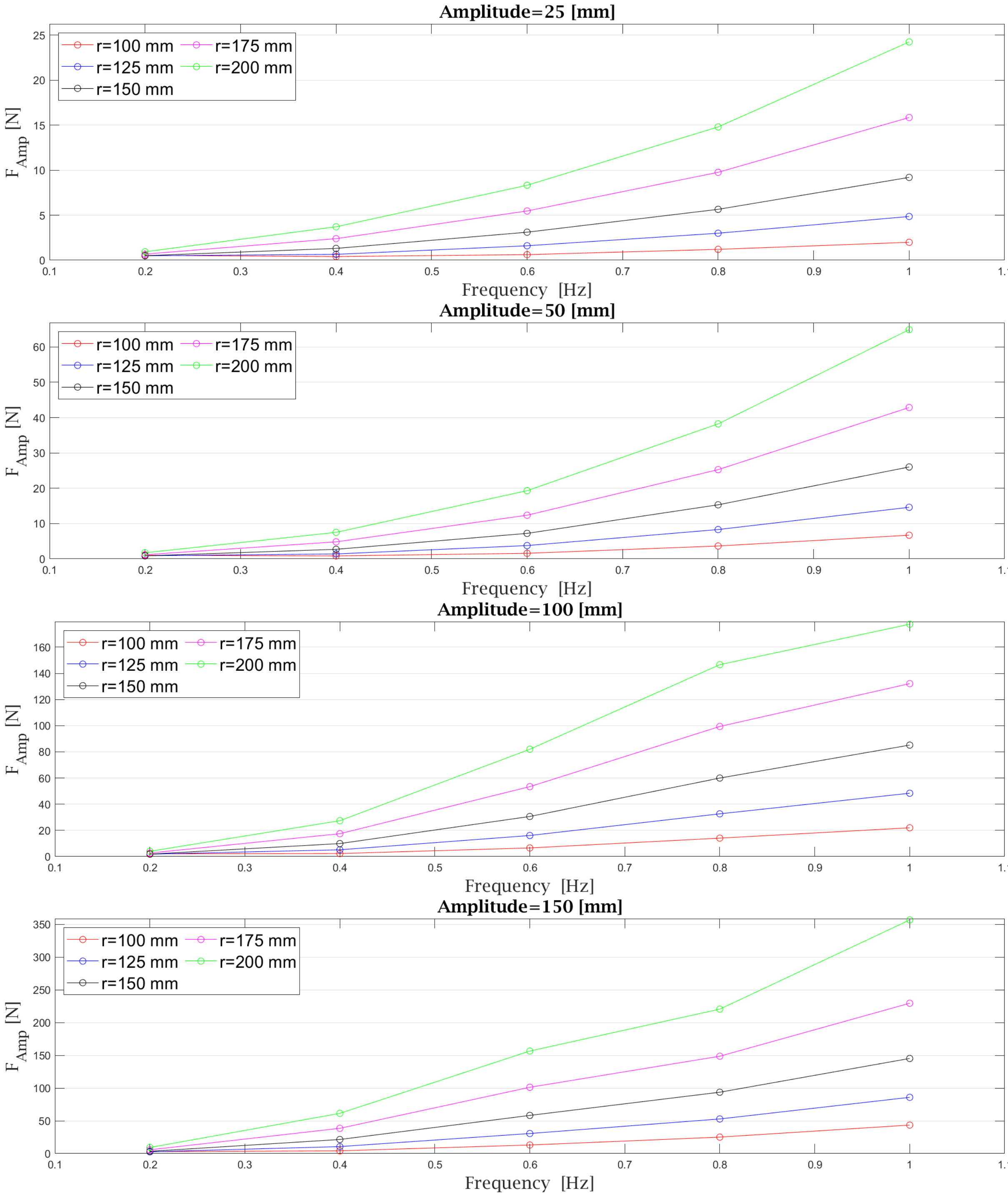

Figure 4.21: Force amplitudes for the modelled cases with $T_{d,mean} = 300\,\text{mm}$.

4.5.2 Results for varying minimum draft

Figure 4.24 and 4.25 shows the added mass and drag coefficients for the simulations with variations of the minimum draft. Added mass and drag coefficient don't seem to have any clear correlation with $T_{d,min}$. However this might be explained by the SPH model not being discretized into small enough particles. As T_d is measured from the bottom of the plate, and the thickness of said plate is 18 mm, the remaining distance to the surface is only three particles thick for $T_{d,min} = 50\,\text{mm}$. Combining this with the fact that the heave motion disturbs the surface, drastically lowers the reliability of the results. This is visualised in Figure 4.22, where two models with different minimum draft, namely $T_{d,min} = 50\,\text{mm}$ and

$T_{d,min} = 150\,\text{mm}$, are shown to the time where the heave plate is at its highest. This inaccuracy is also seen in the force time series in Appendix D, where more scatter in the data can be seen for the models with lower $T_{d,min}$ values. The scatter seems to decrease as $T_{d,min}$ increases.

Figure 4.26 shows the force amplitude from the setup. Here the same trend as from the experiment can be seen- Larger oscillation amplitudes and higher frequencies all induces larger loads. The minimum draft does not seem to have a clear correlation with the force amplitudes.

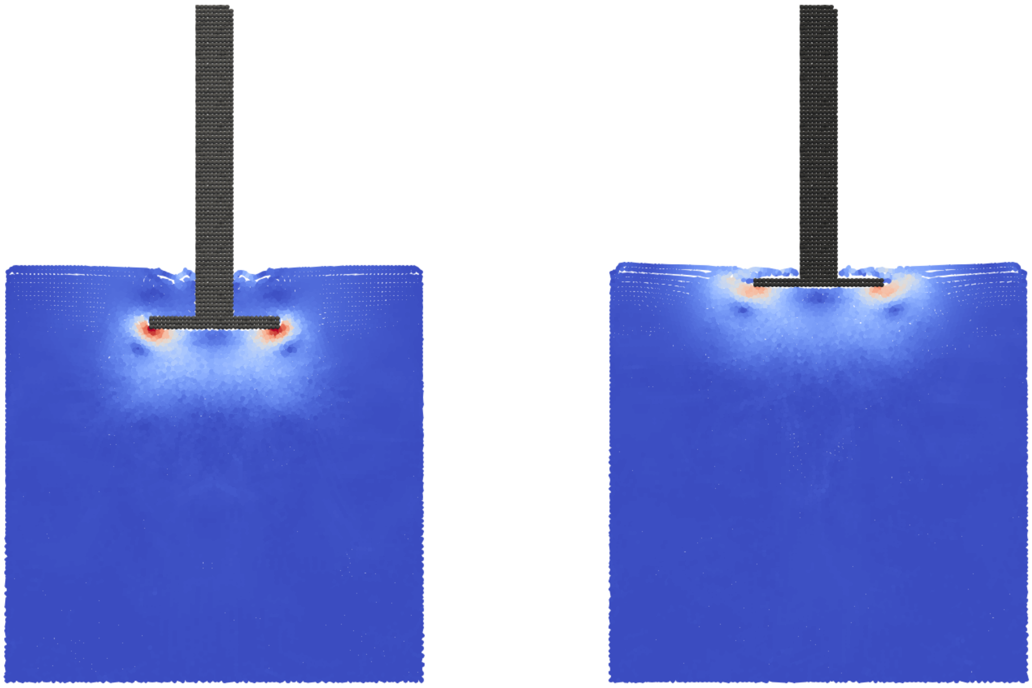

Figure 4.22: SPH visulations for different minimum draft, both models with $f = 0.6\,\text{Hz}$, $r = 125\,\text{mm}$, and $a = 100\,\text{mm}$. **Left:** $T_{d,min} = 150\,\text{mm}$. **Right:** $T_{d,min} = 50\,\text{mm}$.

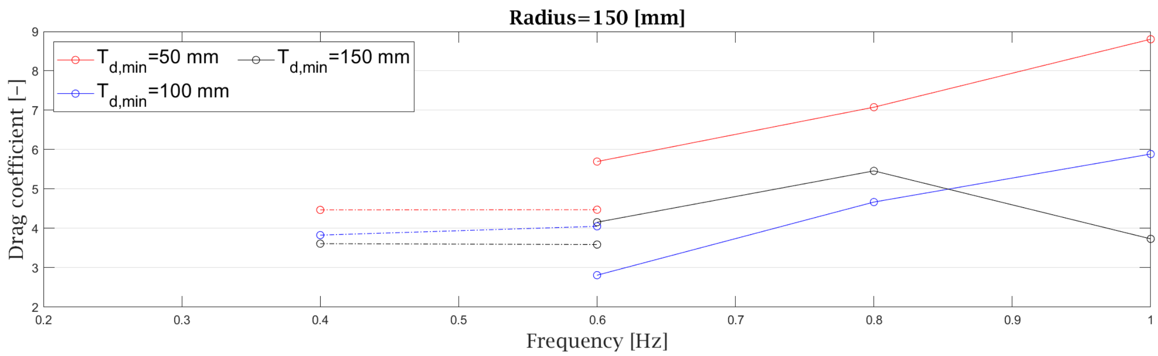

Figure 4.23: Drag coefficients for the modelled cases with $r_d = 150\,\text{mm}$, where the lines with linestyle "$- \cdot -$" represents amplitude, $a = 100\,\text{mm}$ and the solid lines represent $a = 50\,\text{mm}$.

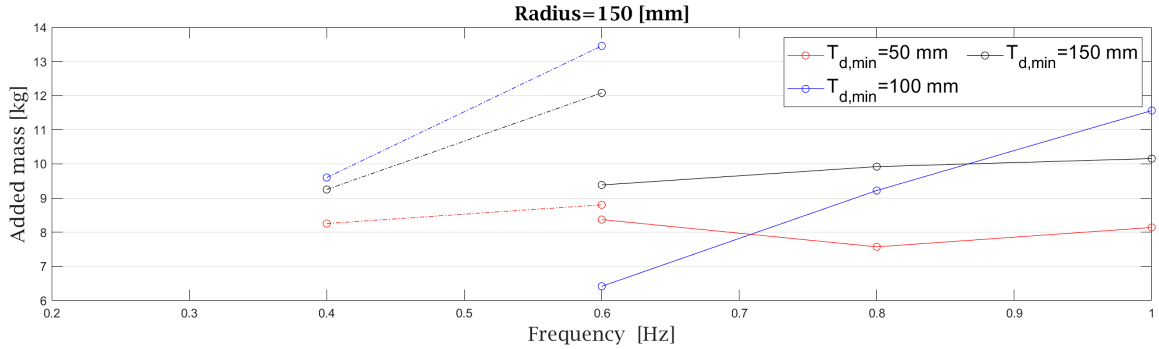

Figure 4.24: Added mass for the modelled cases with $rd = 150\,\text{mm}$, where the lines with linestyle "$-\cdot-$" represents amplitude, $a = 100\,\text{mm}$ and the solid lines represent $a = 50\,\text{mm}$.

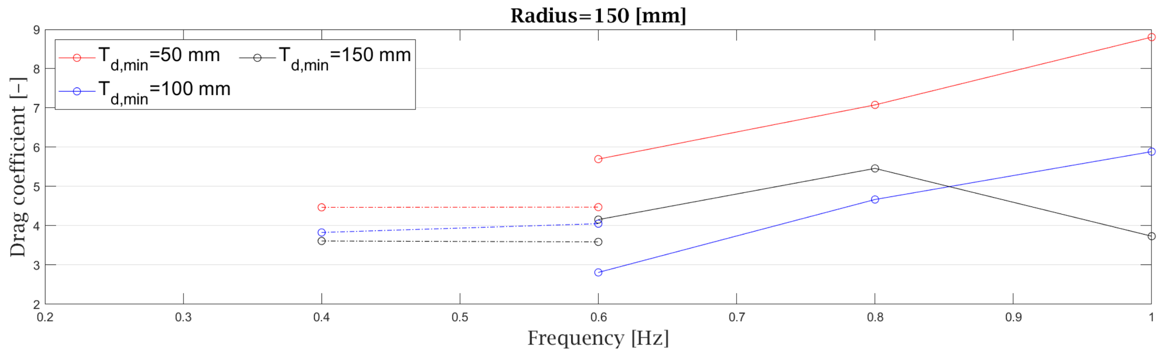

Figure 4.25: Drag coefficients for the modelled cases with $rd = 150\,\text{mm}$, where the lines with linestyle "$-\cdot-$" represents amplitude, $a = 100\,\text{mm}$ and the solid lines represent $a = 50\,\text{mm}$.

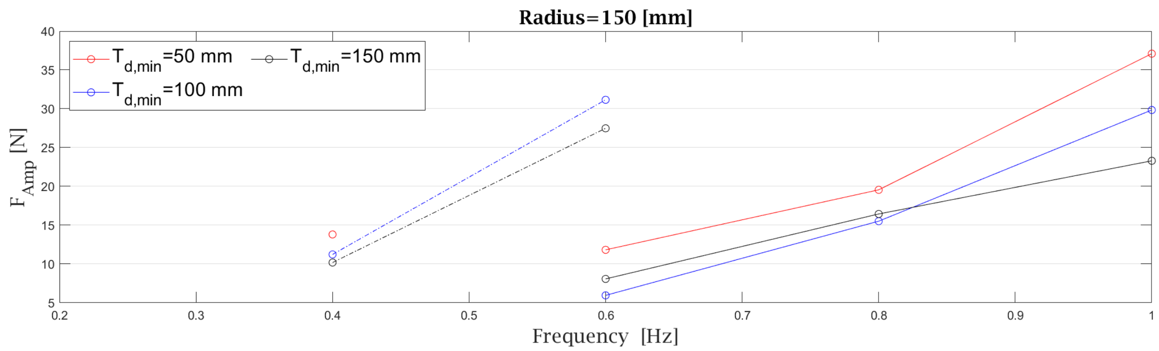

Figure 4.26: Force amplitudes for the modelled cases with $rd = 150\,\text{mm}$, where the lines with linestyle "$-\cdot-$" represents amplitude, $a = 100\,\text{mm}$ and the solid lines represent $a = 50\,\text{mm}$.

Comparison of data 5

In this chapter results from chapters 2, 3 and 4 are compared in terms of amplitude of force, added mass, and drag coefficient. For increased clarity all figures in this chapter follows the legend rules described in table 5.1. Results for the ordinary setup, and the setup with varying minimum draft are showed separately.

	Experiments	SPH	Theory
Linetype	Solid ——	Dashed - - -	Dotted ········
Data points	○	△	×

Table 5.1: Common legend for this chapter.

5.1 Ordinary setup

5.1.1 Force amplitude

The force amplitude of experiments, SPH-models and theoretical calculation is displayed in figures 5.1 and 5.2. The force amplitude increase as all three input parameters increase, a, f and r_d. This seems consistent for all three models but they naturally do not agree perfectly. For the cases with $a = 25$ and 50 mm the SPH model yields results below both the theoretical, and experimental results. The theoretical results on the other hand, are only below the experiment for $r_d = 100$ mm and 125 mm, and seems to come close to the experimental results at 150 mm. For $r_d = 175$ and 200 mm the force amplitudes are larger than the experiment.

The SPH results follows the same trend for $a = 100$ and 150 mm as for the lower amplitudes, yielding forces that are lower than the experiment. The theoretical results are at all times lower than the experimental results for amplitudes $a = 100$ and 150 mm.

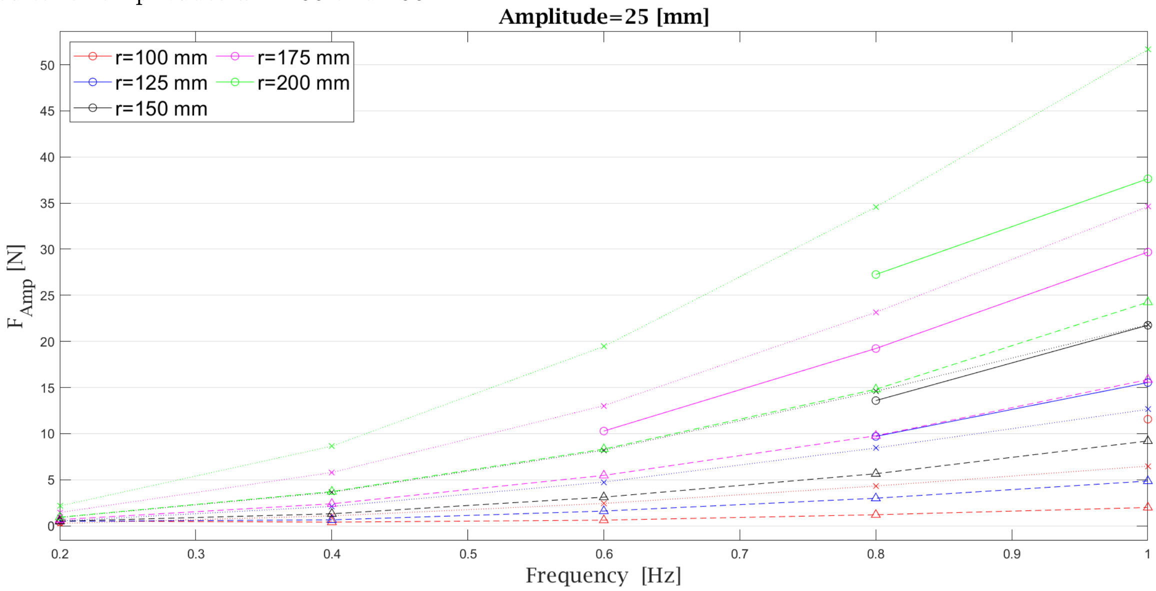

Figure 5.1: Comparison of data with oscillation amplitudes kept constant, as a function of frequency.

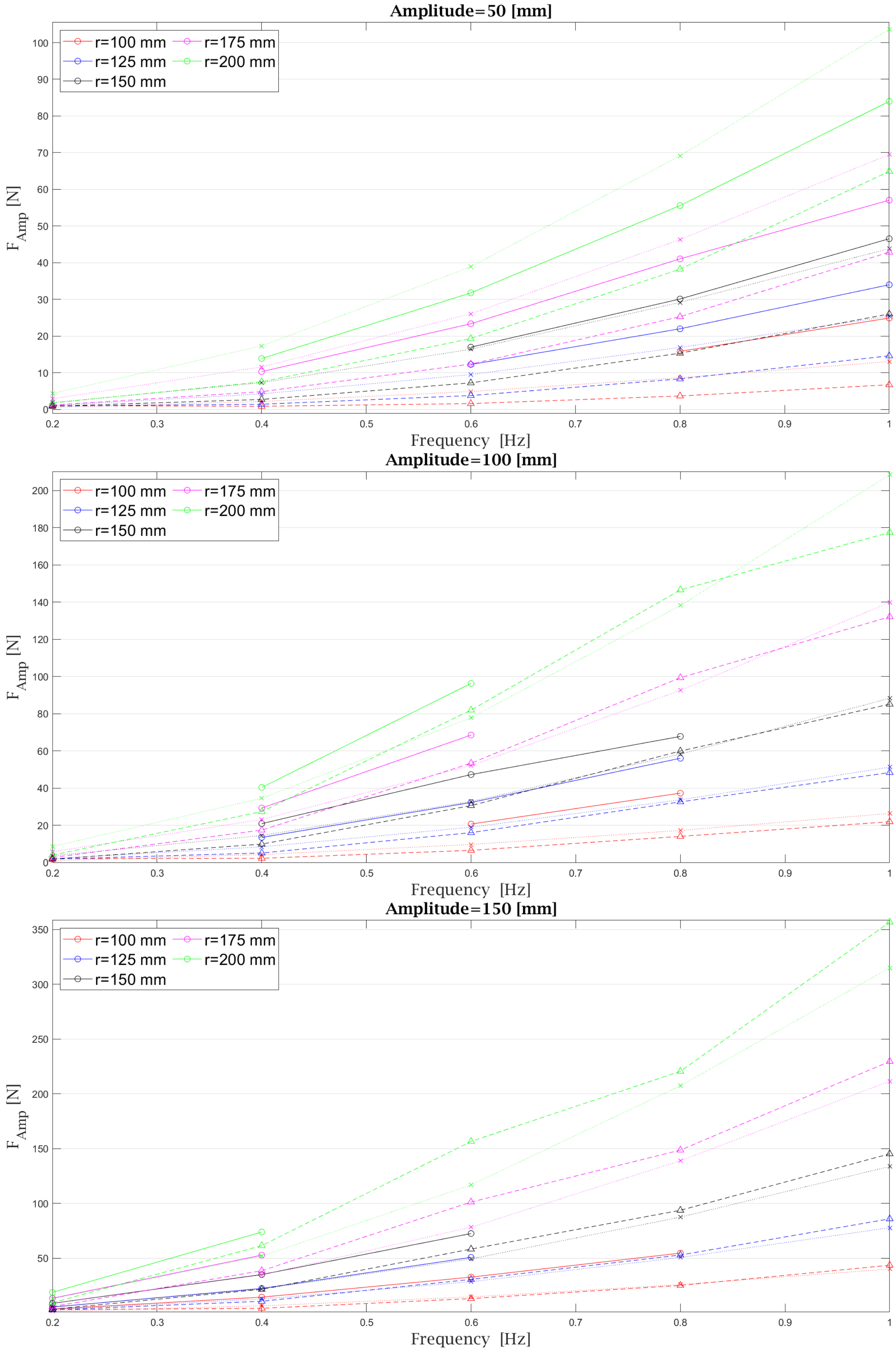

Figure 5.2: Comparison of data with oscillation amplitudes kept constant, as a function of frequency.

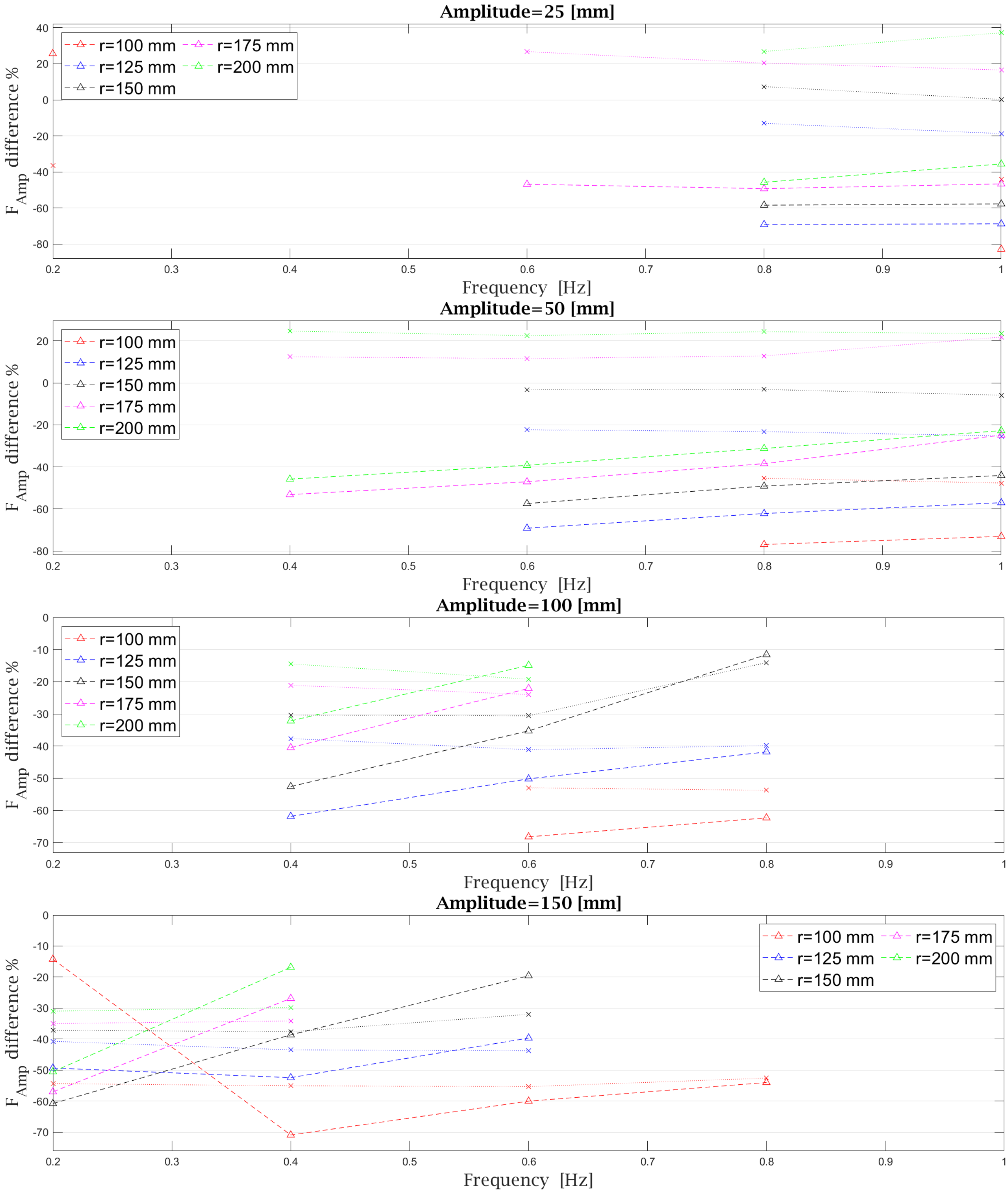

Figure 5.3: Percent difference in force amplitudes for both SPH and theoretical results with respect to the experimental results.

When comparing both SPH and theoretical results with the experiments the accuracy might be more clear when looking at percentage differences. The percentage difference between force amplitude of either SPH or theory and the experimental data, are shown in figure 5.3. Here negative percentages represent that amplitudes are lower than those of the experiment and positive percentages amplitudes above those of the experiment.

Looking at the theoretical data in figure 5.3 the error seem to be, in many cases, almost constant for each radius and amplitude. If the percentage difference is indeed constant for changes in frequency it implies that the error of the theory is independent of the movement. The error varying for changes in amplitude contradicts this to a certain degree, as changing amplitude changes the velocity/acceleration of the heave plate the same way changing the frequency does. See table 5.2.

		a [mm]			
f [Hz]	T [s]	25	50	100	150
0.2	5.0	0.01	0.02	0.04	0.06
0.4	2.5	0.02	0.04	0.08	0.12
0.6	1.6	0.03	0.06	0.12	0.18
0.8	1.25	0.04	0.08	0.16	0.24
1.0	1	0.05	0.10	0.20	0.30

Table 5.2: Mean absolute velocities for the test cases in [m/s]. Compared cases are colored.

From table 5.2 it becomes apparent that if the change in velocity/acceleration is the cause of the error for the theoretical data, the change in error between the case with $r = 200$ mm, $a = 50$ mm, $f = 0.4$ Hz and $r = 200$ mm, $a = 50$ mm, $f = 0.8$ Hz should be the same as the change in error between $r = 200$ mm, $a = 50$ mm, $f = 0.4$ Hz and $r = 200$ mm, $a = 100$ mm, $f = 0.4$ Hz, example cases are underlined in table 5.2. The errors of the cases are 24.7 and 24.3% for the fist two and, 24.7 and -14.5% for the latter. Obviously the change in error is significant for the latter of the two comparisons whereas it is almost non existent for the first. That concludes that the difference in error is not correlated to the change in velocity. The most obvious difference between the impact of changing these two parameters is that changing the amplitude also implicit changes the minimum draft of the heave plate. This indicates that the changes in error between different amplitudes are due to the theoretical method not taking into account the proximity of the surface.

Observing the error of the SPH results on figure 5.3 two definite trends become visible. First off, the results seem to become more accurate as the radius of the heave plate increase. Secondly the results seem to become more accurate as both amplitude and frequency increases. The first of these two trends is likely related to the size of the SPH particles in relation to the heave plate radius. As the particle size is the same ($p_d = 10$ mm) for all cases of SPH simulation, the number of particles which occupies the area of the heave plate vary with the radius. A rough estimate of the mean number of particles covering the area of the heave plate can be found by:

$$n_p \approx \frac{A_{heave}}{(\frac{p_d}{2})^2 \cdot \pi} \tag{5.1}$$

With A_{heave} being the area of the heave plate, and p_d being the particle size. Results for the different radii are displayed in table 5.3 along with the corresponding errors for the cases with $a = 100$ mm and $f = 0.6$ Hz. This difference in discretization seems to have an impact on the accuracy of the results, contradicting the convergence of particle size in section 4.3.4, since the discretization of an $r_d = 100$ mm disc with a particle size of 0.005 m is the same as a $r_d = 200$ mm disc with a particle size of 0.01 m.

r_d [mm]	100	125	150	175	200
A_{heave} [cm^2]	314.16	490.87	706.85	962.11	1256.63
n_p	400	625	900	1225	1600
Example error	-68.2%	-50.2%	-35.3%	-22.1%	-14.9%

Table 5.3: Area, and rough estimate of particles occupying the heave plate. Each SPH particle occupies 0.79 cm^2, the example errors are given for $a = 100$ mm and $f = 0.6$ Hz.

The difference in error for changes in amplitude and frequency are more curious, and might be caused by the choice of viscosity formulation for the SPH models. The simulations has been run with the *Artificial* *viscosity* formulation by [Monaghan, 1992] which guarantees the stability of the model at high velocities, which is logical, as it is developed to predict astronomical events. In addition it guarentees the stability of models with free water surfaces. It does however yield high shear viscous forces at low velocity and as a results have trouble correctly predicting low velocity flow cases [Vorobyev, 2012]. The *Artificial velocity* formulation is, in DualSPHysics controlled by the choice of the parameter α which defaults to 0.01 since it has proven the best to describe wave loads on offshore structures. As a reference the error for the SPH results for the same three compared cases as the the theoretical error are: -45.8, -31.2 and -32.2% showing a consistent dependency on the velocity of the movement.

If the error of the SPH model is caused by a combination of these two effects, correcting them by using a more discretized model and either a different viscosity formulation or configuring α to fit the lower velocities found in the experiment should significantly reduce the errors displayed in figure 5.3.

5.1.2 Added mass

Added mass as described in the theory in chapter 2.1 is the mass of water which moves with the object. From this added mass, the added mass coefficient C_a is found:

$$C_a = \frac{m_{added}}{\rho \, V_R} \tag{5.2}$$

In the Morison equation the inertia coefficient is used which is found as $C_m = 1 + C_a$. The algorithm for deducing the added mass A of an object in [DNV GL A/S, 2011] described in appendix B, results in added mass found based on the inertia coefficient and not the added mass coefficient:

$$C_m = \frac{m_{added}}{\rho \, V_R} + 1 = \frac{A}{\rho \, V_R} \tag{5.3}$$

The value of the reference volume V_R vary with the choice of theory, as it is not standardized for the heave plate geometry, see section 2.1. Therefor the added mass for both the experiment and SPH models are more accurately comparable with the theory by using A instead of m_{added}. The theoretical results shown in figure 5.4 are therefore corrected to be represented as A.

Looking at figure 5.4, the added mass calculated by the SPH model for the frequency 0.2 Hz for all cases of simulation are well below the other results, and seems to stand out in particular. This could be an effect of the uncertainty connected to the low velocities mentioned in section 5.1.1. The remaining SPH results are all below the added mass of the experiment, but as the experimental data they seem to be somewhat correlated to changes in amplitude. The higher frequency cases with $r_d = 100$ and 125 mm are almost constant with changes in frequency as expected, but the cases with $r_d = 150$, 175 and 200 mm has some variation for changes in frequency. These changes with frequency are inconsistent, as it would seem as the added mass peaks around a frequency off 0.6 Hz, which is both inconsistent with theory and experimental results. The most feasible reasons for this is that the SPH model has some inconsistency, or that the fitting method for finding added mass has some inaccuracy.

The added mass formulation by [Tao et al., 2007] are well below both the other theories as well as any results of the experiments. The added mass formulation presented by DNV and the slightly altered sphere yields, although slightly different, consistently the highest values of added mass for the theoretical formulations. The added mass represented by an ellipse are per definition lower than that of the sphere.

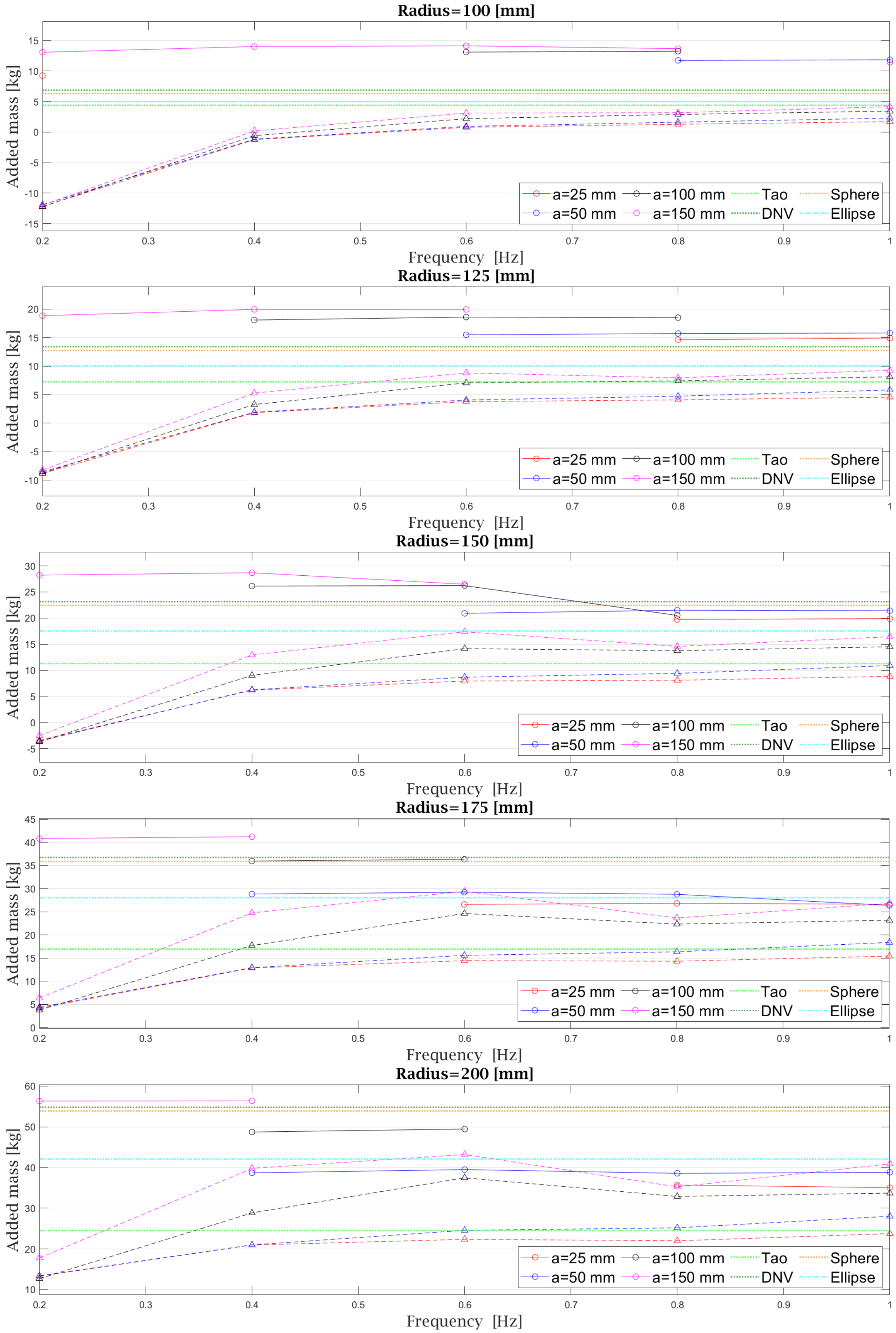

Figure 5.4: Added mass calculated for the experiment, SPH models and corrected theoretical values.

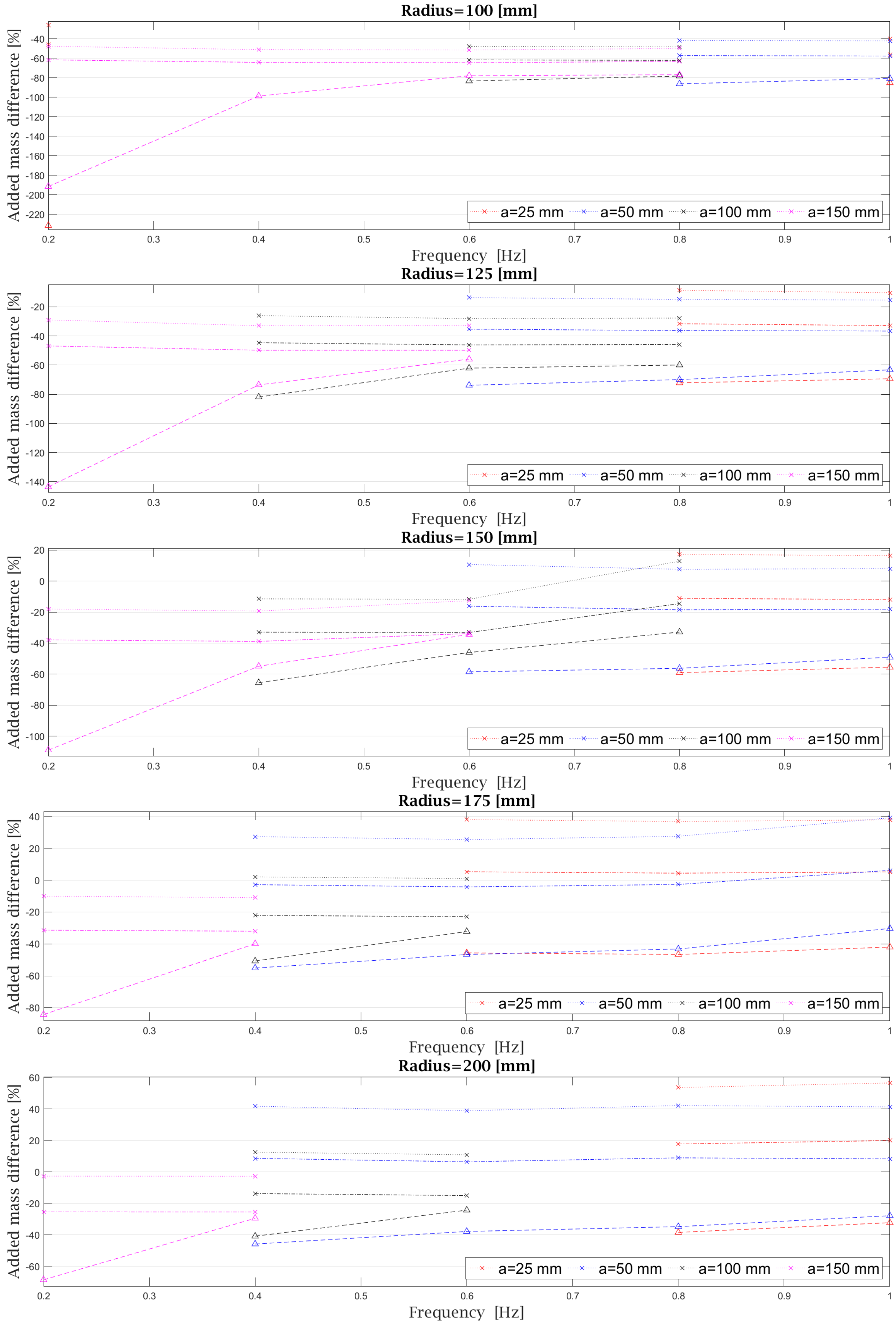

Figure 5.5: Added mass difference in % between results of SPH, DNV and elliptical added masses and experimental results. As two theoretical results are present the elliptical results are depicted with a $- \cdot -$ linestyle.

As for the comparison of force amplitude the differences in result might be more clear when looking at percentage differences in figure 5.5. Since the formulation by [Tao et al., 2007] are well blow the others and the spherical added mass is consistently only slightly below that of [DNV GL A/S, 2011]. Only the DNV and elliptical added masses has been included in this comparison.

As for the comparison of force amplitudes it is clear that the margin of error for the SPH added mass decreases as both the particle velocity and radius of the heave plate increases. This is not surprising as the method of which the added mass is deduced is based on the the same time series of force.

The margin of error for the theoretical results does not show much. As the added mass is constant for changes in frequency and amplitude the change in error between each amplitude is only the difference in added mass measured during the experiment. As described in section 3.6 this is likely caused by the change in minimum draft as the change in amplitude reduces the minimum distance to the surface. Both the DNV formulation and the elliptical theory seems to yield gradually higher results as the radius increases, compared to the experimental data. The overall reliability of the theory does not seem to change, as it seems that further increases of the heave plate radius might cause the theoretical estimations of added mass to be significantly higher than what is realistic.

5.1.3 Drag coefficients

When subjected to the method described in appendix B, the experimental and SPH results yield the fitting parameter B in addition to the added mass. This fitting parameter is the linearized damping of the heave plate, which in turn describes the drag coefficient of the heave plate, along with the drag area. Following the theory described in [DNV GL A/S, 2011], this drag coefficient is constant for an objects shape. For a circular thin plate $C_d = 1.12$ for values of Reynolds numbers above 10^3. The lowest mean Reynolds number for all experiment cases is $Re = 4.0 \cdot 10^3$. Results are displayed on figure 5.6. And percentage differences for the results of SPH, and theoretical results with respect to the experiment are shown in figure 5.7

The drag coefficients of the experiments does not vary much with changes in radius but do get slightly larger as the radius increase. Whether this is a measure of the increased turbulence is unknown. There is almost no variation for changes in frequency, but there is a trend that for the larger amplitudes results in lower drag coefficients. In a similar fashion to what was discussed in section 5.1.1 this effect might be caused by the proximity of the surface, even though this should imply that results are getting less accurate as the amplitude increases, when comparing to the theoretical value of $C_d = 1.12$ this is not the case as the largest amplitudes are closest to the theoretical value.

The results from the SPH simulations seems to follow the same trend as mentioned in section 5.1.1. The results for the lower velocities are far from the expected values, but as the frequency and amplitudes increase this effect diminish and the results form an almost straight line. Although this line does not seem to asymptote towards the theoretical drag coefficient, it does for most cases come reasonably close to the experimental results.

Notably the percentile errors for the SPH drag coefficients are in general the lowest of all three compared parameters. This might be caused by SPH more accurately modelling the velocity effects in the fluid rather than acceleration effects. Although this is speculation, and the difference is more likely a result of the velocity formulation of the fit, for deriving added mass and drag coefficient, being more accurate than the acceleration fit.

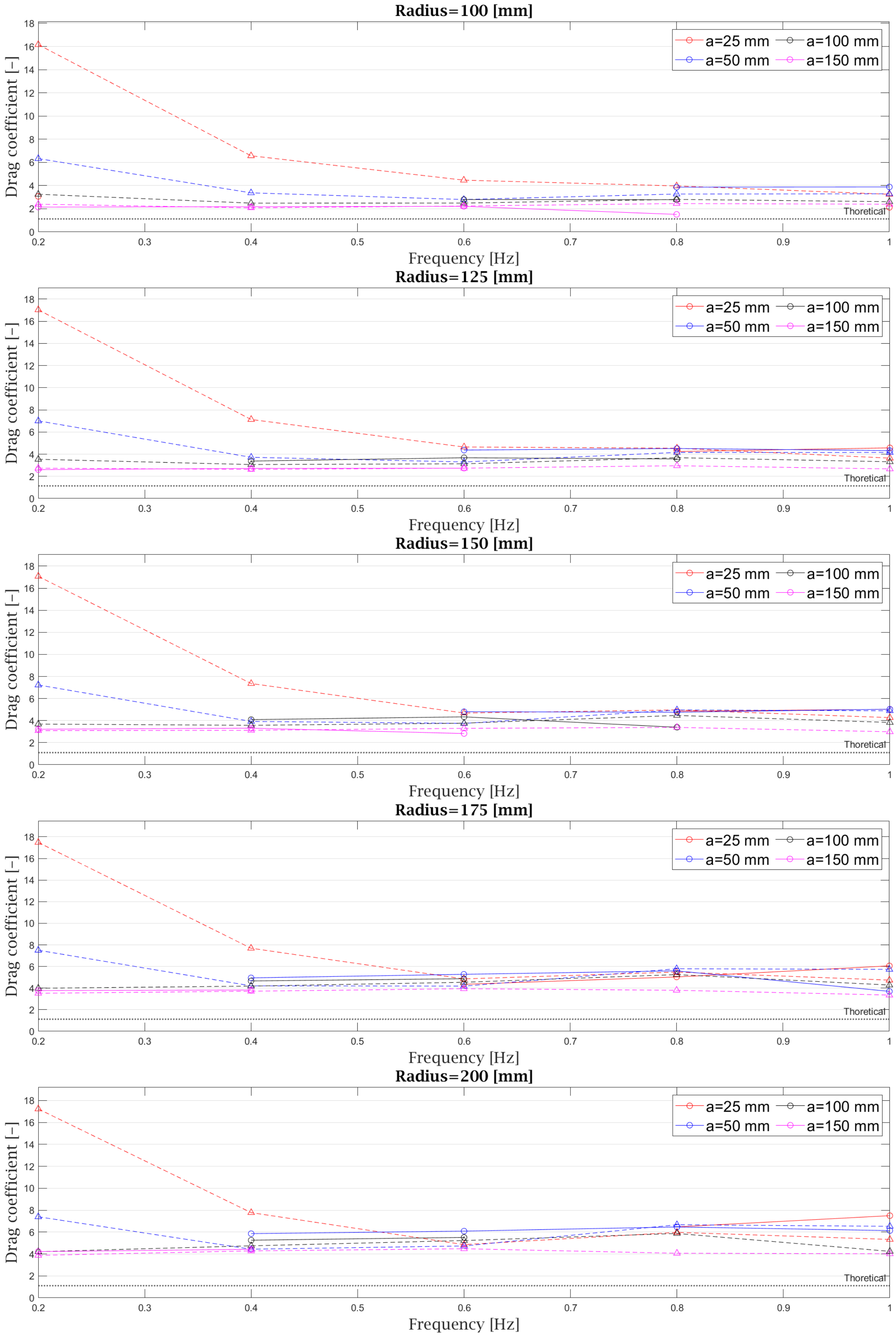

Figure 5.6: Drag coefficients of the experimentals, SPH model and theoretical results.

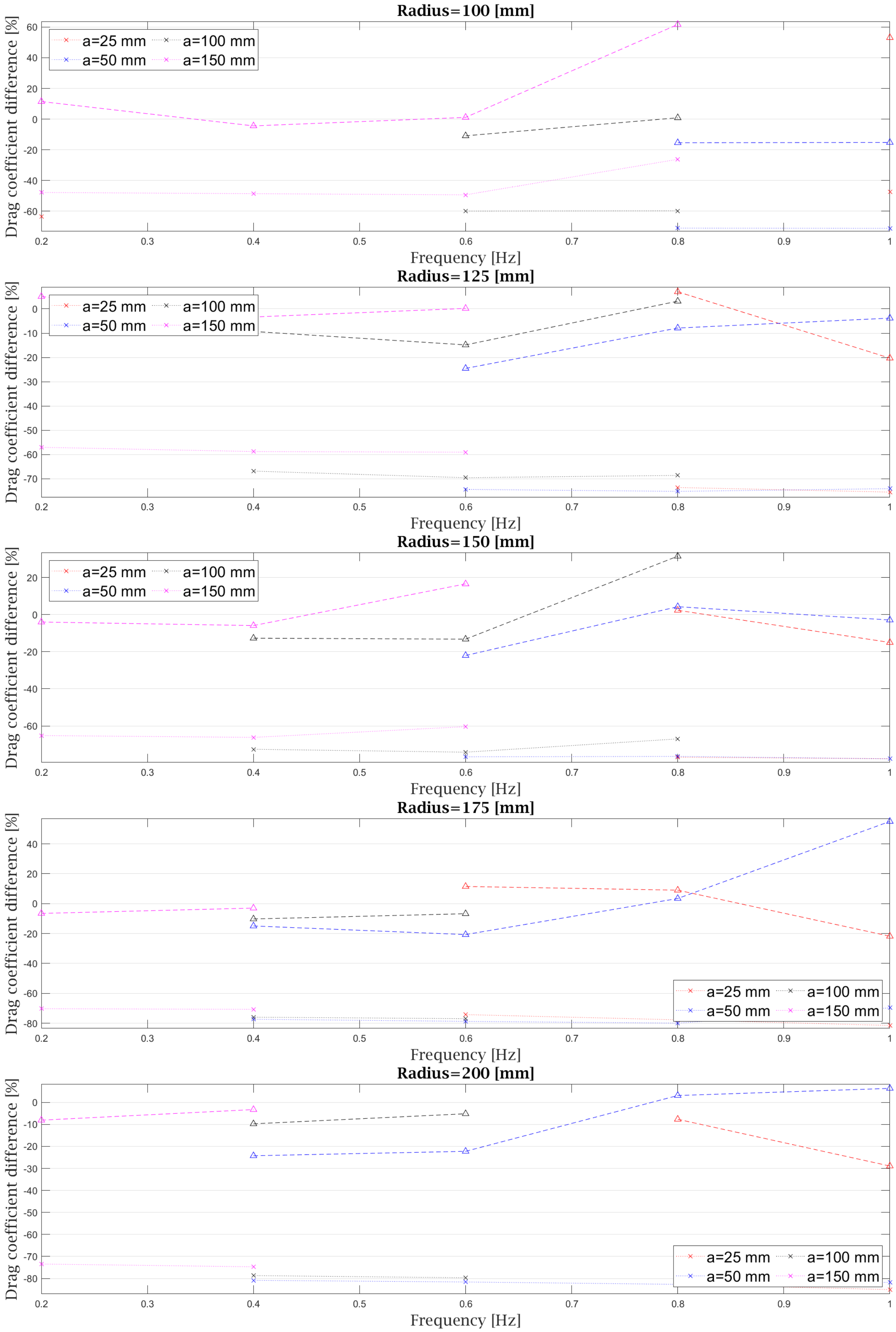

Figure 5.7: Drag coefficient difference in % for the SPH model and theoretical results compared to the experiments.

5.2 Varying minimum draft

5.2.1 Force amplitude

The force amplitude from the experiment and the SPH simulations are shown in figure 5.8. The two models seem to roughly follow the same trend as in the ordinary setup. As the parameters frequency and amplitude increases so does the forces. However for all the combinations of frequency, amplitude and distance to surface, the force amplitudes of the experiments are larger than results of the SPH model. Figure 5.9 show the percentage difference between force amplitude of SPH and the experiments. There is roughly a 50 % difference for most of the combinations. However the percentage difference seem to be weakly correlated with frequency and amplitude, where cases with larger values of a and f has smaller margins of error. This observation is consistent with the trends observed in section 5.1.

No clear correlation can be seen in the force amplitude with the change in minimum draft, $T_{d,min}$. The numerical model seems to agree with the experiment, where a change in $T_{d,min}$ do not influence the force amplitude significantly.

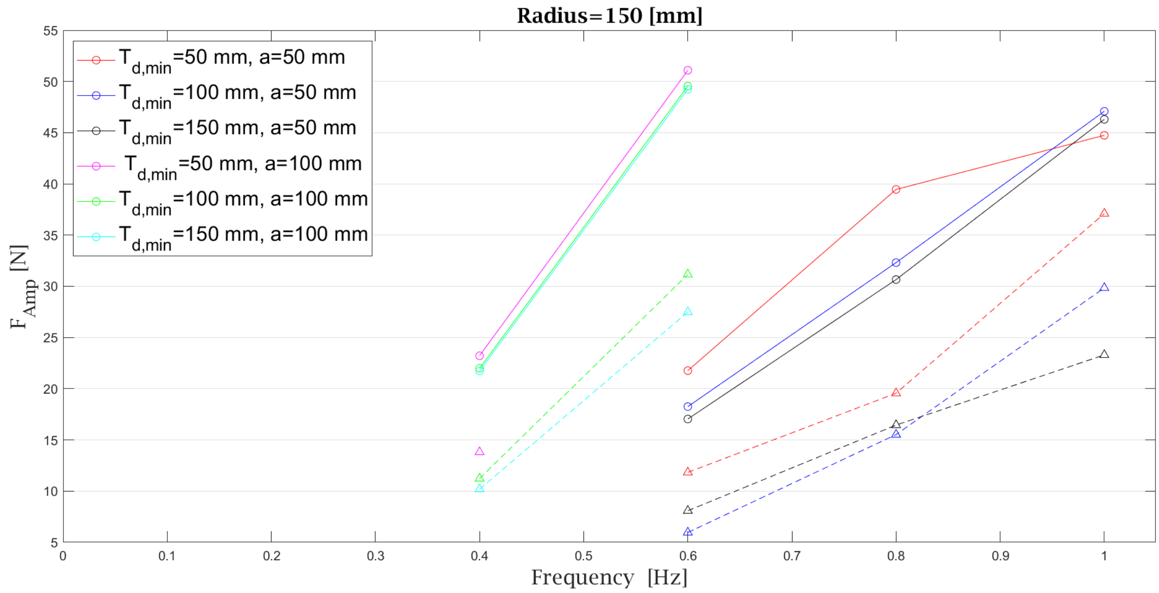

Figure 5.8: Force amplitudes from the experiment and SPH.

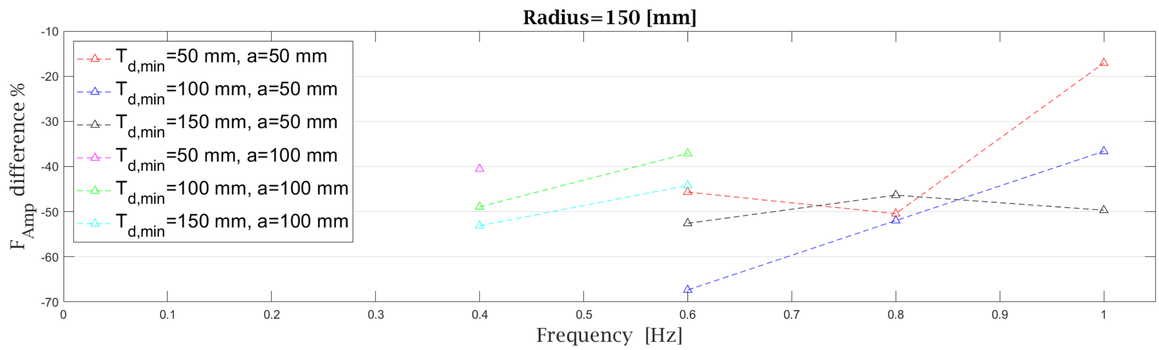

Figure 5.9: Force amplitudes difference for experiment and SPH.

5.2.2 Added mass

The added mass from the experiment and the SPH simulations are shown in figure 5.10. The added mass calculated from the SPH model follows the same trend as for the force amplitudes as it is well below the results from the experiment. However the two models seem to disagree. The added mass of the SPH model increases with the frequency, and the added mass of the experiment decrease with an increase in frequency. This can be explained by the way the added mass is calculated by fitting a curve to the force time series. Figure 5.12 shows the fitted curve for two examples with different values of $T_{d,min}$, namely $T_{d,min}$ = 50 mm and $T_{d,min}$ = 150 mm. Here it can be seen that the curve fits for the setup with a low $T_{d,min}$ value does not fit as well as for the setups with a high $T_{d,min}$ value. So if the results for $T_{d,min}$ = 50 mm and $T_{d,min}$ = 100 mm are discarded, due to bad fits, and only $T_{d,min}$ = 150 mm are compared, the same tendencies as for the ordinary setup is displayed. For $T_{d,min}$ = 150 mm and a = 50 mm for both SPH and experiment seems to agree that the added mass is constant with changes in frequency as expected. This is presumed to be because the hydrodynamic effects of the movement are too far from the surface to take effect.

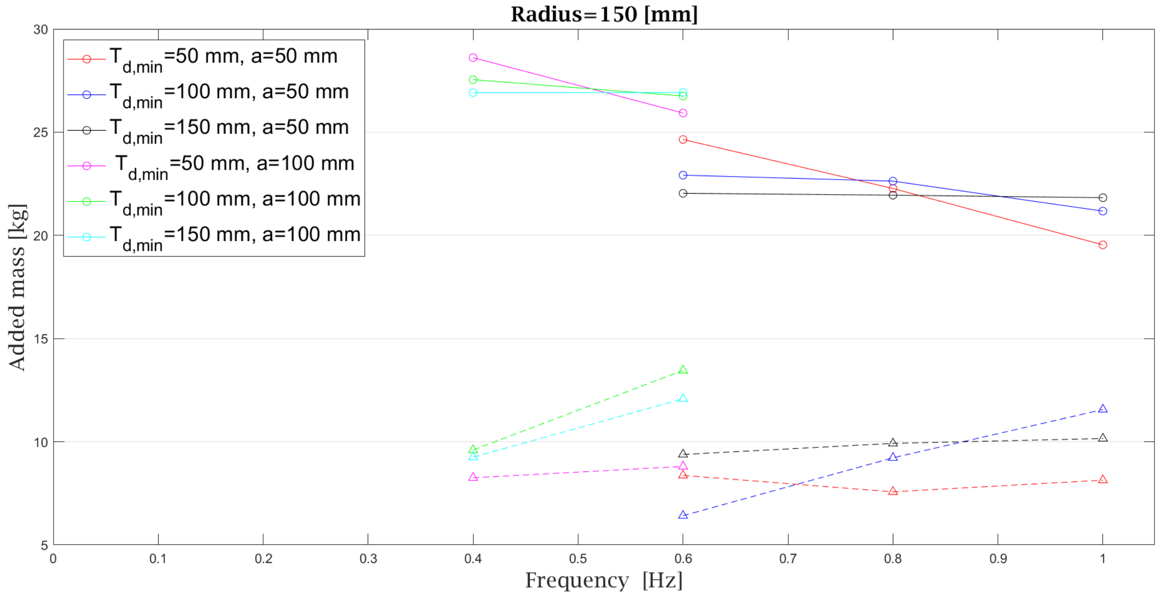

Figure 5.10: Added mass from the experiment and SPH.

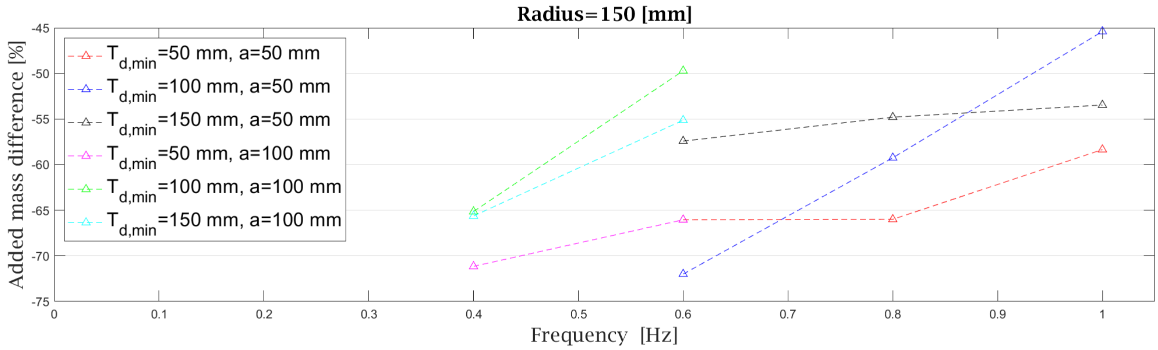

Figure 5.11: Added mass difference from the experiment and SPH.

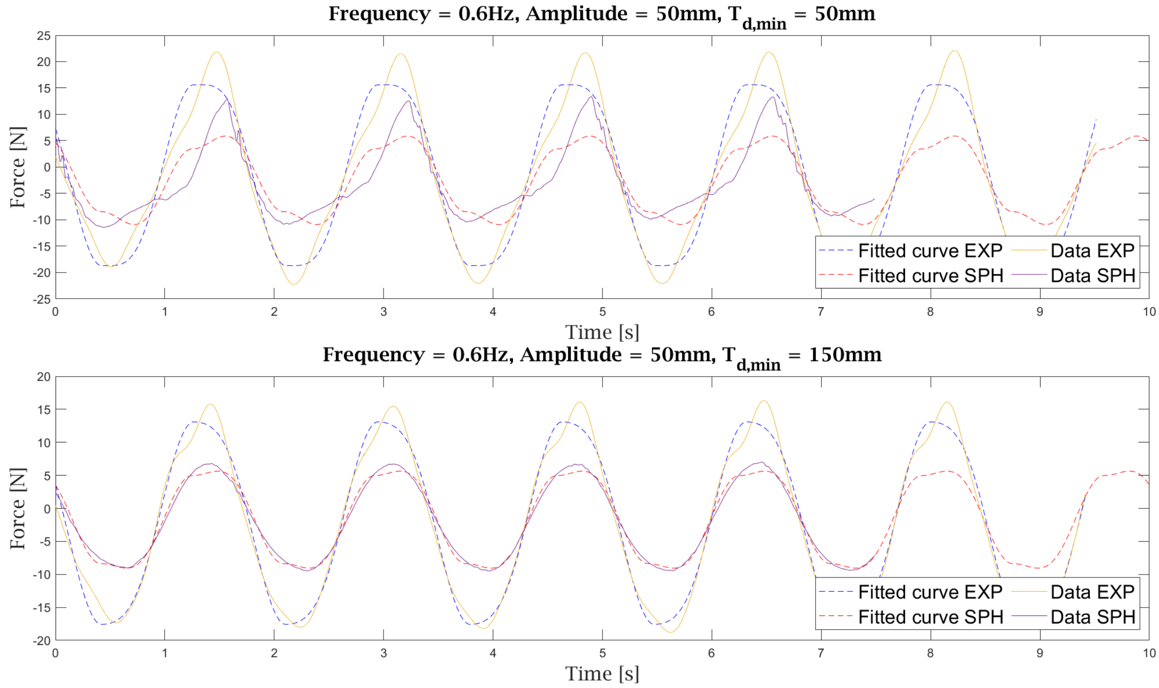

Figure 5.12: Force curves for both SPH and experiment, with fitted curves.

5.2.3 Drag coefficients

The drag coefficients from the experiment and the SPH simulations are shown in figure 5.13. As for added mass, the drag coefficients are found by fitting a curve to the data. The curve fits for the setup with a low $T_{d,min}$ value does not fit as well as for the setups with a high $T_{d,min}$ value, which makes the drag coefficients hard to compare. However for $T_{d,min} = 150\,\text{mm}$ the same trend can be seen for both experiment and SPH, as it is farther away from the surface. Due to the bad fits the drag coefficients and added mass does not tell much about how well SPH model handles the change in minimum draft.

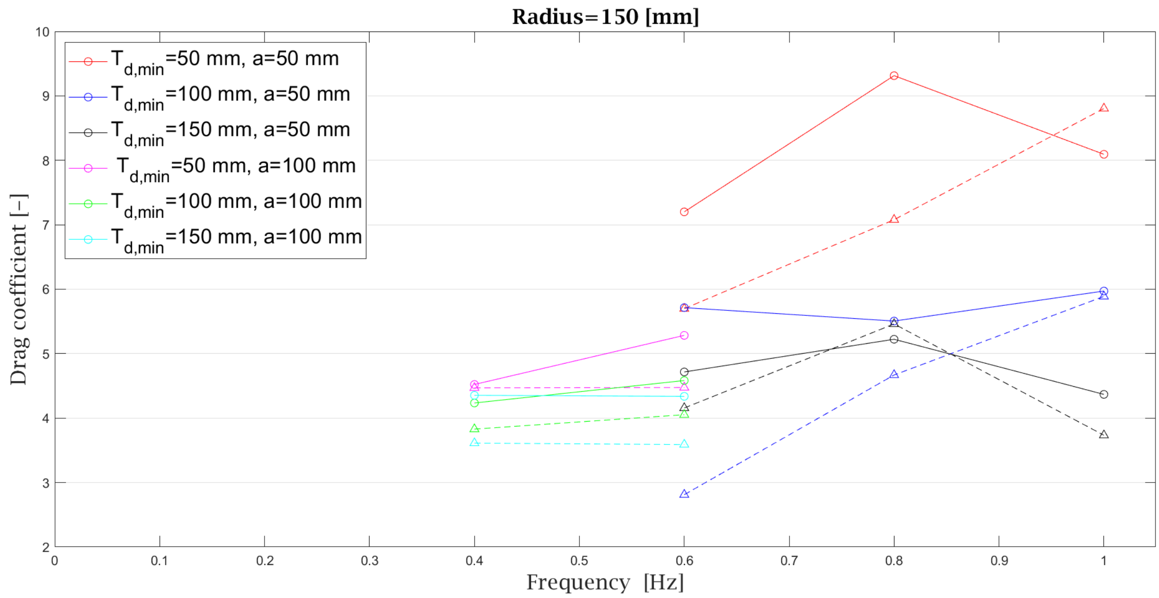

Figure 5.13: Drag coefficients from the experiment and SPH.

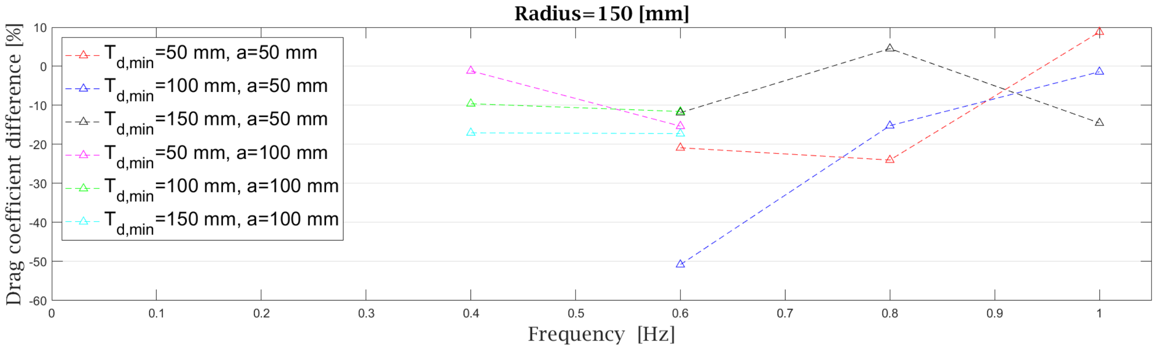

Figure 5.14: Drag coefficients difference from the experiment and SPH.

Discussion 6

This chapter addresses the assumed causes of error between the different testing methods described in chapter 5, as well as the accuracy of the found added masses and drag coefficients.

In chapter 5 several trends in terms of error between the experimental, theoretical and SPH model results were identified: Different amplitudes of motion seemed to influence the results independent of the velocity, the discretization of the SPH model appear to influence results, and the velocity appear to have an impact on the accuracy of the SPH simulations. These trends are further investigated and discussed in the following sections. In addition, the accuracy of the method, for which added mass and the drag coefficient is found, is discussed, as well as the validity of the methods overall.

6.1 Surface distance/amplitude

It was observed in chapter 5 that the added mass for experiment and SPH models seemed correlated with amplitude. It was assumed that it likely is caused by the change in minimum draft, as the change in amplitude reduces the minimum distance to the surface. To find out whether this is true, amplitude and minimum draft is compared. In table 6.1 the added mass calculated from the experimental data is shown for disc radius $r = 150\,\mathrm{mm}$. As seen in the table the added mass does not vary significantly with $T_{d,min}$. For amplitude $a = 100\,\mathrm{mm}$ the added mass varies from 28.6 kg to 25.3 kg and for amplitude $a = 50\,\mathrm{mm}$ it varies 24.65 kg to 19.54 kg. Notably all of these extremum values are for $T_{d,min} = 50\,\mathrm{mm}$. If $T_{d,min} = 50\,\mathrm{mm}$ is disregarded and only the rest of the data is considered, then the added mass variation with $T_{d,min}$ is even lower. For amplitude $a = 100\,\mathrm{mm}$ the added mass varies from 27.54 kg to 26.19 kg and for amplitude $a = 50\,\mathrm{mm}$ it varies 22.92 kg to 20.91 kg. This leads to the conclusion that the observed correlation with amplitude is not caused by the change in minimum draft, as minimum draft of 2/3 disc radius or higher does not influence the added mass significantly. Additionally the observed correlation with amplitude is presumably caused by the development of flow around the disc. A visualisation of the flow around the heave plate for different variations of parameters are shown in figure 6.1.

		Frequency [Hz]			
Td,min [mm]	Amplitude [mm]	0.4	0.6	0.8	1.0
50	50	-	24.65	22.27	19.54
	100	28.61	25.3	-	-
100	50	-	22.92	22.63	21.18
	100	27.54	26.75	-	-
150	50	-	22.04	21.95	21.82
	100	26.91	26.92	-	-
250	50	-	20.91	21.51	21.42
200	100	26.19	26.21	-	-

Table 6.1: Added mass for experiment, shown for disc radius $r = 150\,\mathrm{mm}$. Units in [kg].

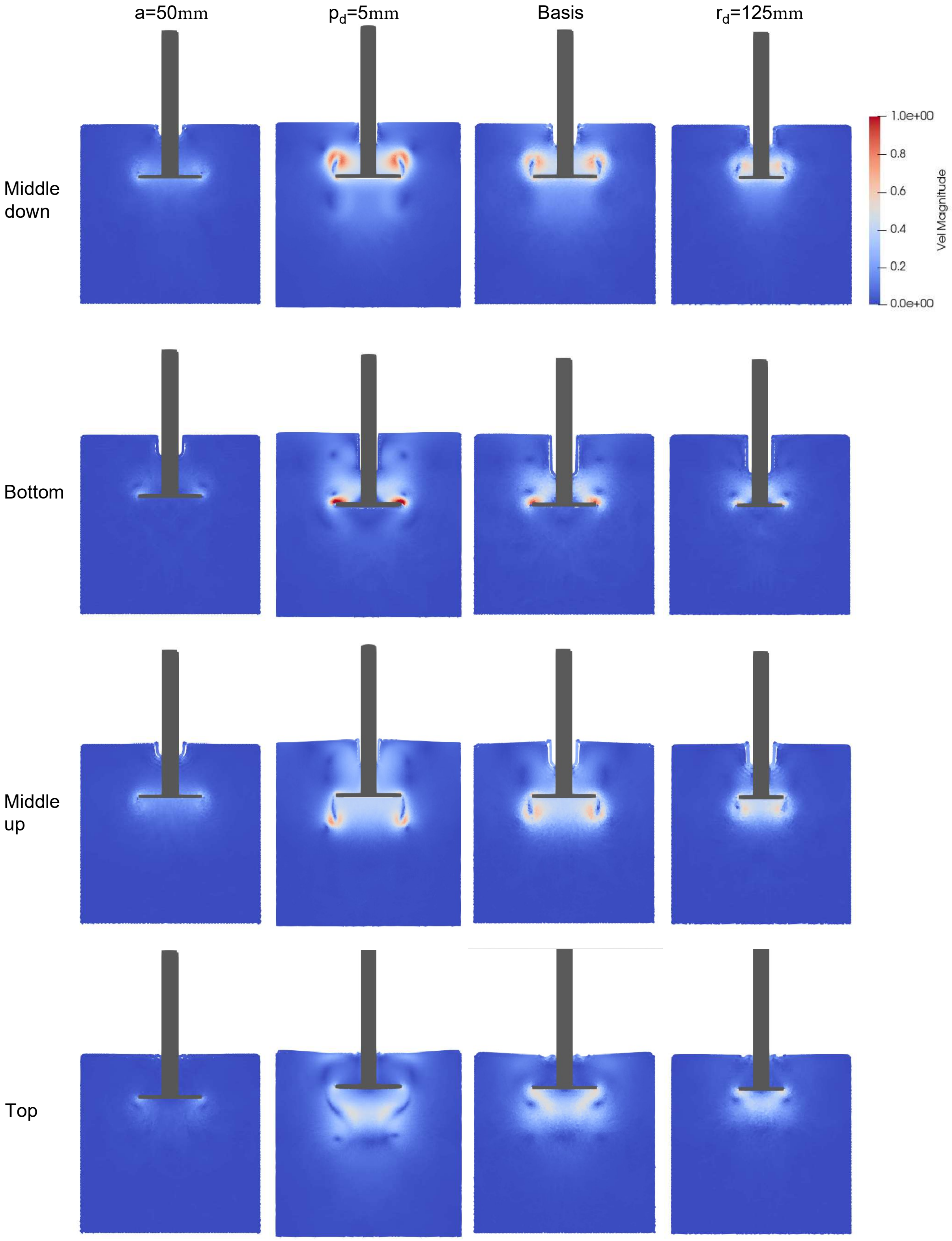

Figure 6.1: Visualisation of the SPH flow around a heave plate given different variations of parameters. The basis column is simulated for the case with $r_d = 175$ mm, $a = 100$ mm, $f = 0.6$ Hz and particle size of $p_d = 10$ mm. Other columns represent the same model with one changed parameter. The flow is displayed for the motion at the positions: Middle-moving down, bottom, middle-moving up and top.

6.2 Discretization

In chapter 5 it was discovered that the error of SPH results, compared to the experiments, generally decrease as the heave plate radius increases. To find out whether the difference in discretization is the cause of this trend, a study of the particle size is performed for the case with $r_d = 100\,\text{mm}$, $a = 25\,\text{mm}$ and $f = 1\,\text{Hz}$. This case is chosen because it is the case with the largest error for force amplitude at -82 %. See figure 5.3. The simulation is run for particle sizes of $p_d = 20$, 10, 8 and 6 mm. The resultant time series is shown on figure 6.2, and force amplitudes is found to 1.30, 1.99, 2.41 and 2.28 N respectively.

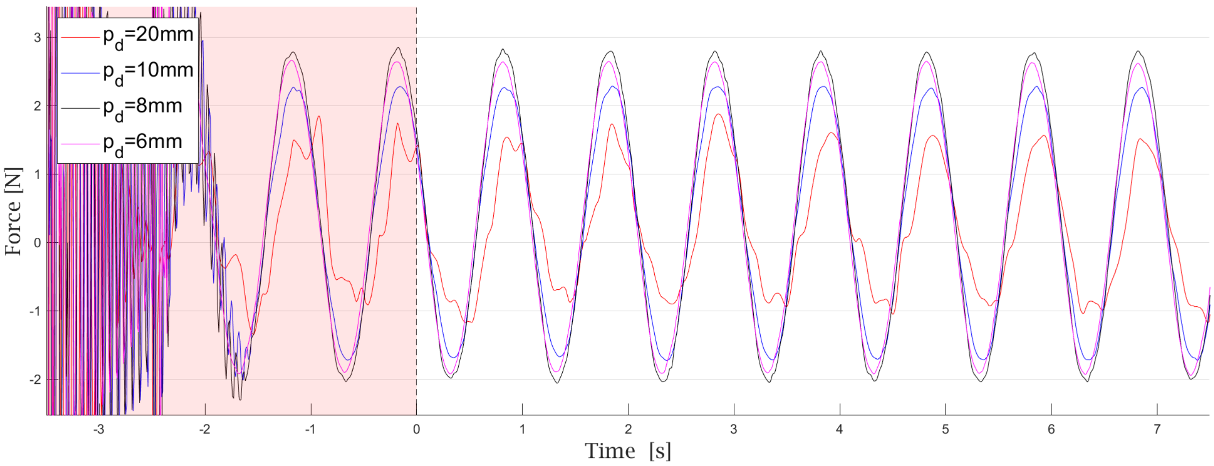

Figure 6.2: Force time series for the convergence study of particle size for $r_d = 100\,\text{mm}$, $a = 25\,\text{mm}$ and $f = 1\,\text{Hz}$.

Looking at figure 6.2 the difference between the levels of discretization seems rather meaningful with an increase of 15 % in force amplitude from the particle size used in the experiment, $p_d = 10\,\text{mm}$, to $p_d = 6\,\text{mm}$. Although, comparing this force amplitude to the results of the experiments, the increased discretization does not seem to have any meaningful influence on the results, as the error between the case with $p_d = 6\,\text{mm}$ and the experiments is still -80 %. Following equation (5.1) an increase in discretization from $p_d = 10$ to 6 mm increases the number of particles covering the heave plate area from $n_p \approx 400$ to 1111. If lack of discetization is the main source of error this increase should bring the margin of error close to that of the $r_d = 175\,\text{mm}$ heave plate with a particle size of $p_d = 10\,\text{mm}$ as it has $n_p \approx 1250$. This is not the case as the $r_d = 175\,\text{mm}$ case has an error of -47 %. This leads to the conclusion that the effect of the increased discretization are minimal and that the increased accuracy at higher values of r_d are caused by some other phenomenon.

Presumably larger heave plates causes larger particle velocities in their vicinity as they move, which links the increased accuracy of larger radii to the effects of the increased velocities and the viscosity formulation, which are discussed in section 6.3. A visualisation of this effect is shown in figure 6.1, along with the difference in flow for SPH models with particle 10 mm and 5 mm.

6.3 Viscosity formulation and velocity

In chapter 5 it was observed that the SPH model accuracy increases as velocity of the movement increases. To quantify this observation the percentile errors for force amplitudes of the SPH model for the coloured velocities in table 6.2 is displayed in table 6.3.

		a [mm]			
f [Hz]	T [s]	25	50	100	150
0.2	5.0	0.01	0.02	0.04	0.06
0.4	2.5	0.02	0.04	0.08	0.12
0.6	1.6	0.03	0.06	0.12	0.18
0.8	1.25	0.04	0.08	0.16	0.24
1.0	1	0.05	0.10	0.20	0.30

Table 6.2: Mean absolute velocities for the test cases in [m/s]. Colored cases corresponds to the percentile differences of table 6.3.

r_d [mm]	100		125		150		175		200	
Amplitude	1	2	1	2	1	2	1	2	1	2
Orange	-	-	-69.1	-	-58.4	-	-49.2	-53.2	-45.7	-45.8
Green	-	-14.2	-69.2	-49.3	-57.4	-60.8	-47.1	-57.0	-39.2	-50.5
Red	-76.9	-	-62.2	-61.9	-49.1	-52.6	-38.4	-40.5	-31.2	-32.2
Purple	-68.2	-70.9	-50.2	-52.4	-35.3	-38.6	-22.1	-26.9	-14.9	-16.8

Table 6.3: Percentile error of force amplitude for SPH simulation corresponding to the mean absolute velocities of table 6.2. Amplitude corresponds to first and second amplitude at which the mean velocity appears.

Looking at table 6.3, it is clear that the mean velocity of the setup definitely is correlated to the margin of error of the SPH simulation. Additionally it emphasises the observation that larger radii induces smaller errors. Notably there is very little difference between the accuracy at amplitude 1 and 2 for most cases. This reinforces the assumption that the error is mostly dependant on the velocities as the mean velocity of the heave plate is the same.

As stated in chapter 5, a likely cause of this accuracy discrepancy for the different velocities is the choice of viscosity formulation in the SPH simulations. To test whether the accuracy problem can be solved by simply changing to the other viscosity formulation available in dualSPHysics, a set of simulations is run with the "*Laminar viscosity and SPS turbulence*" viscosity scheme. The four cases run with the new viscosity scheme are:

Case nr.	r_d [mm]	a [mm]	f [Hz]	Mean velocity [m/s]
1	125	25	1	0.05
2	125	50	0.6	0.06
3	125	100	0.4	0.08
4	125	150	0.2	0.06

These cases were chosen as they have have low mean velocities, and in turn large percentile errors for the "*Artificial velocity*" SPH models. The force amplitudes of the SPH simulations for the different viscosity schemes are displayed in figure 6.3.

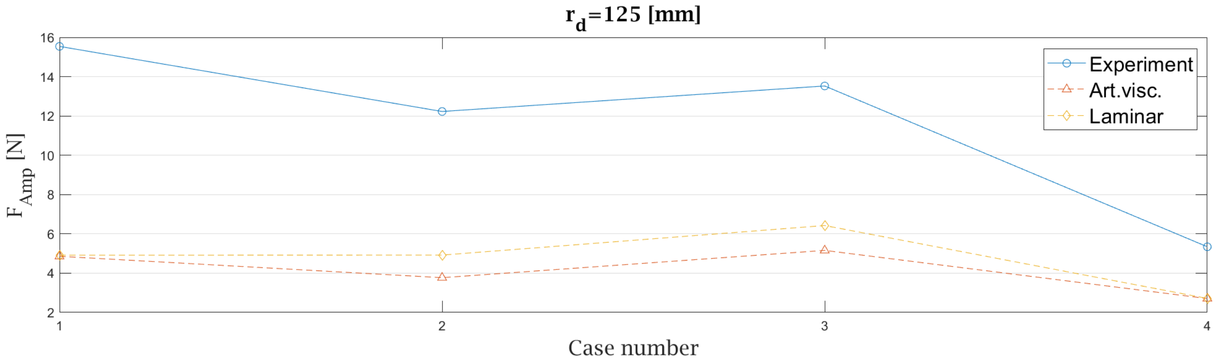

Figure 6.3: Force amplitudes for SPH simulations with differing viscosity schemes and the experiment.

Notably on figure 6.3 the results for case 1 and 4 are almost completely equal for the different viscosity schemes. Although for the cases 2 and 3 the laminar viscosity scheme results in larger peak forces than the artificial. Even though these two cases do show increased accuracy, the fact that case 1 and 4 did not, counteracts the argument. As no clear accuracy increase can be perceived there is no grounds on which to conclude that the laminar scheme would yield overall more accurate results than the artificial viscosity scheme.

As the laminar viscosity scheme did not seem to solve the accuracy problem of the SPH simulations, two approaches to correcting the error are proposed. The first is to model the heave plate setup as a full scale model with accordingly larger particles. If the viscosity problem is based on low numerical velocities the larger movements and bodies will induce velocities large enough to yield accurate results. If the problem on the other hand is based on relative velocities, a second approach, although more tedious, might yield better results. As the artificial viscosity scheme is based on the parameter α, it might be tuned to yield appropriate results for the velocities sizes of the given scenario.

6.4 Added mass and damping coefficient method

After using the method of deducing the added mass and drag coefficients from the force time series described in appendix B, it has occurred that it is quite vulnerable to displacements in time. Since the method is based on fitting a sum of sine curves, describing the movement of the object, to the force time series, the size of the resulting fitting parameters are as a result very vulnerable to any phase shift that is not taken into account said fitting function. This means that if there for any reason, is even a little delay, or difference in the data that moves the force peaks in time, this impacts the resultant added mass and drag coefficients. As a visual representation of how much any delay can impact the added mass and drag coefficients, the resultant A and C_d of the experiment and SPH model for $r_d = 175\,\text{mm}$, $a = 100\,\text{mm}$, $f = 0.6\,\text{Hz}$, with different displacement in time are shown in figure 6.4.

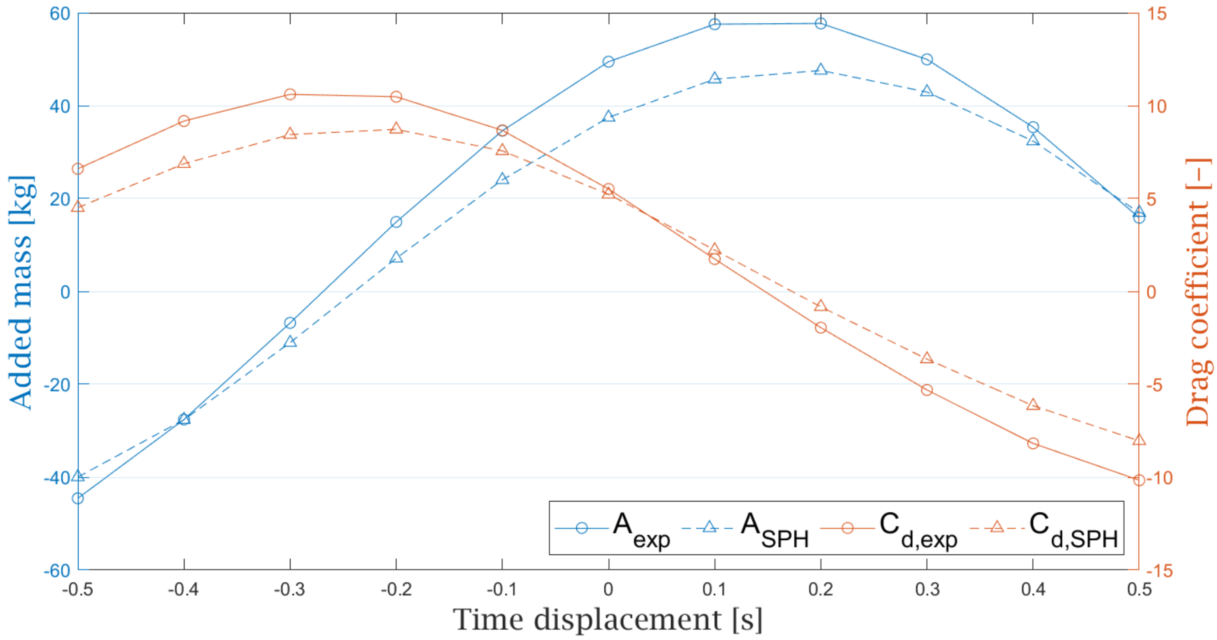

Figure 6.4: Resultant values of A and C_d for displacements in time.

As visible in figure 6.4 a relatively small displacement of the time series results in significant differences in its accuracy. This brings into consideration the assumption that the velocities and accelerations used for the fit, are the inverse of the movement of the heave plate, and not the movement of the particles. While this may very well be a fair assumption, any delay in the development of flow around the heave plate might have impacted the results. If this is the case, and there is some form of delay, the actual values of the added mass and drag coefficients might not represent the hydrodynamics of the heave plate very well. Even so this does not mean that the method is useless. As it is based upon a fit of the data, the values of A and C_d are correct no matter the time displacement, and can be reinstated in the formula to reproduce the said fit. This means that even though the velocity of the heave plate might not agree perfectly with the particle velocity of the water, as long as the fit is accurate, the time series can be reproduced based on the motion which was used in the fit. Or in this case the motion of the heave plate. While this does not guarantee that the values of A and C_d are correct in terms of the hydrodynamics it does guarantees that the time series produced is representative of the input, dependant on the input motion. Which is very useful from a practical standpoint as it enables reproduction of eg. experimental data in a theoretical model.

Conclusion 7

The purpose of this thesis was to asses the hydrodynamic effects of oscillating heave plates via a theoretical approach, SPH modeling and physical experiments.

The experiments was conducted on oscillating heave plates with different sizes, amplitudes, frequencies and distance to the surface. A large part of the data from said experiments was disturbed by the actuator being unable to reproduce the specified movement accurately, this caused large parts of the data to be discarded as they did not accurately depict the intended hydrodynamics. Even with the reduced sample size the experimental results were still comparable to both the SPH simulations and theoretical approach. As the theoretical and SPH models both introduces assumptions or parameters, which might not be representative for the given hydrodynamic problem, the results of the experiment were assumed to be the most accurate of the three, and used as the point of comparison.

The theoretical approach was based on the Morrison equation and in turn rely on the added mass-, and drag coefficients chosen for the heave plate. As these coefficients are not standardised for more complicated geometries, different values of added mass coefficients were used as an attempt to determine if one was more accurate than the others. When results of the theoretical approach was compared to the experiment, the margin of error was inconsistent as the theoretical approach yielded results both larger and smaller than those of the experiment, for the different heave plate cases. Unfortunately due to these inconsistencies none of the choices for the added mass coefficient could be deemed overall more accurate than the others.

The theory states that the added mass and drag coefficients are constant for changes in both the frequency and amplitude of the oscillation performed by the heave plate. When looking at the results of both SPH models and the experiment, this statement seems false. Both SPH and experimental results show some variation in added mass and drag coefficient with changes in amplitude, but with the relative small sample size of this thesis, more data will be needed to prove this theorem.

For the SPH model a preliminary study on the parameters used in the simulation was conducted. Here the domain size of the simulation was assessed, it was found that a relatively small domain size was cable of representing the water basin used in the conducted experiment. A similar study was conducted on the particle size to find a level of discretization fine enough to accurately represent water and adequately rough as to not cause unnecessary computational time. These findings were then used to create a numerical model capable of simulating the conducted experiments.

The SPH model was compared to the experiment. It was found that the SPH model consistently estimates lower loads than the experiment, and accuracy increased as heave plate radius increased. This was theorised to be caused by the particle sizes being too large. It was found that a finer discretization did improve the results, but not enough to explain the error. Additionally it was discovered that the SPH model was reproducing the result from the experiment for a fast moving heave motion better than a slow moving motion. This was presumed to be caused by the viscosity scheme of the model not being able to accurately predict low velocity flows. This statement agrees with the increased accuracy of the larger plates, as they presumably cause larger particle velocities when moved.

A study on the influence of the minimum draft of the disc was conducted to make sure that results were not affected by surface effects. For this a set of SPH simulations and an experiments was conducted. Even though the tests only provided a relatively small sample size it indicated that as long as the minimum draft is larger than 2/3 of the heave plate radius the effects from the surface proximity is minimal.

Neither the SPH model nor the theoretical approach yielded results which were consistently close to those of the experiment. While the theoretical formulation are more consistently closer to the experimental results, the margin of error changes with the differing radii and amplitudes making it unreliable, at least with the choices of assumptions and parameters used in this thesis.

The SPH formulation on the other hand is very unreliable for the cases with low velocities and quite reliable when velocities are increased. For the cases with the largest velocities the error is reduced below -20% and given further discretization of the model might close the gap even further. Although to be a viable tool for predicting heave plate hydrodynamics the velocity problem needs to be looked into.

Even if this velocity problem is solved, another limiting factor of the SPH method is the long computational time. With the computational equipment used for this thesis a standard simulation of the heave plate takes approximately 2.5 hrs for a simulation of 11 seconds. This is a simulation of a very simple geometry, in a small domain, with a relatively low level of discretization. Just looking at the simulated time, a simulation of the effects from eg. a 10 minute wind time series would in theory take 136 hrs for the setup presented in this thesis. As a result the SPH simulations might be a tool for determining the added mass and drag coefficients of a component for use in eg. a boundary element model, and not a replacement for already established CFD models such as BEM. At least until much more powerful computational equipment is available at more consumer friendly prices, then we might see full scale floating wind turbine SPH models.

Bibliography

Aalborg University [2021], 'Wavelab'.
URL: *https://www.hydrosoft.civil.aau.dk/wavelab/*

Altomare, C., Crespo, A., Rogers, B., Dominguez, J., Gironella, X. and Gómez-Gesteira, M. [2014], 'Numerical modelling of armour block sea breakwater with smoothed particle hydrodynamics', *Computers Structures* 130, 34–45.
URL: *https://www.sciencedirect.com/science/article/pii/S0045794913002824*

C.-H. Lee [1995], *WAMIT THEORY MANUAL*, Massachusetts Institute of Technology.

DNV GL A/S [2011], *DNV-RP-H103 MODELLING AND ANALYSIS OF MARINE OPERATIONS*, april 2011 edn, DNV GL A/S.

Domínguez, J., Fourtakas, G., Altomare, C., Canelas, R., Tafuni, A., García Feal, O., Martínez-Estévez, I., Mokos, A., Vacondio, R., Crespo, A., Rogers, B., Stansby, P. and Gómez-Gesteira, M. [2021], 'Dualsphysics: from fluid dynamics to multiphysics problems', *Computational Particle Mechanics* .

DualSPHysics [2021], 'Dualsphysics wiki'.
URL: *https://github.com/DualSPHysics/DualSPHysics/wiki*

EMODnet [2021], 'Bathymetry'.
URL: *https://www.emodnet-bathymetry.eu*

Global Wind Atlas [2021], 'Global wind atlas'.
URL: *https://globalwindatlas.info*

Michael Meister [2015], 'Smoothed particle hydrodynamics in urban water management', p. 215.

Molteni, D. and Colagrossi, A. [2009], 'A simple procedure to improve the pressure evaluation in hydrodynamic context using the sph', *Computer Physics Communications* 180, 861–872.

Monaghan, J. [2005], 'Smoothed particle hydrodynamics', *Reports on Progress in Physics* 68, 1703.

Monaghan, J. J. [1992], 'Smoothed particle hydrodynamics', *Annual Review of Astronomy and Astrophysics* 30(1), 543–574.
URL: *https://doi.org/10.1146/annurev.aa.30.090192.002551*

NASA [2021], 'The effects of climate change'.
URL: *https://climate.nasa.gov/effects/*

Our World in Data [2020], 'Energy mix'.
URL: *https://ourworldindata.org/energy-mix*

Rambøll [2021], 'Figure of fowt designs'.
URL: *https://ramboll.com/projects/germany/corewind*

Stiesdal, H. [2021], 'Tetraspar and tetrabase, industrialized offshore wind turbine foundations'.
URL: *https://www.stiesdal.com/material/2019/02/Stiesdal-Tetra-01.02.19.pdf*

Tao, L., Molin, B., Scolan, Y.-M. and Thiagarajan, K. [2007], 'Spacing effects on hydrodynamics of heave plates on offshore structures', p. 18.

Truong, N., Arikatla, S. and Enquobahrie, A. [2021], 'Fluid simulation in imstk using smoothed-particle hydrodynamics (sph)'.
URL: `https://blog.kitware.com/sph-fluid-simulation-in-imstk/`

Vorobyev, A. [2012], 'A smoothed particle hydrodynamics method for the simulation of centralized sloshing experiments'.
URL: *https://publikationen.bibliothek.kit.edu/1000031251/2394684*

Wind Europe [2017], 'Floating offshore wind vision statement'.
URL: *https://windeurope.org/wp-content/uploads/files/about-wind/reports/Floating-offshore-statement.pdf*

Wind Europe [2020], 'Wind energy in europe in 2019, trends and statistics'.
URL: *https://windeurope.org/wp-content/uploads/files/about-wind/statistics/WindEurope-Annual-Statistics-2019.pdf*

SPH Theory A

This appendix describes some basic theory behind the SPH formulation used in DualSPHysics. Notably, the general formulation, governing equations, force calculation and time stepping. All theory is based on [DualSPHysics, 2021] and [Michael Meister, 2015]

A Smoothed particle hydrodynamics (SPH) model is a model that takes a continuum of fluid and discretizes it at certain interpolation points/particles. These particles have their own physical properties: mass (m), density (ρ), velocity (v) and pressure (p). The discritized Navier Stokes equation is integrated at each particle location according to the properties of its neighbouring particles. This is done at each time step, and the movement of the individual particle is found from the updated properties. The range of neighbouring particles taken into account is referred to as the smoothing length h.

The conservations of mass, energy and momentum in the fluid, are reformulated to a form suited for particle simulation, rather than their usual differential form. This is done by use of an interpolation function that estimates the values at the particle points. This function is referred to as the kernel function denoted W. It is designed to represent a function F of the position vector $\mathbf{r}$ defined in the integral of $\mathbf{r'}$:

$$F(\mathbf{r}) = \int F(\mathbf{r'})W(\mathbf{r} - \mathbf{r'},h)d\mathbf{r} \tag{A.1}$$

Which can be approximated to a non continuous discrete form. For instance, the interpolation for particle a is a sum of the particles within the smoothing length h:

$$F(\mathbf{r}_a) \approx \sum_b F(\mathbf{r}_b)W(\mathbf{r}_a - \mathbf{r}_b,h)\Delta\mathbf{v}_b \tag{A.2}$$

With v_b being the volume of particle b and, ρ_b and m_b being the density and mass of b respectively, A.2 can be rewritten as:

$$F(\mathbf{r}_a) \approx \sum_b F(\mathbf{r}_b)\frac{m_b}{\rho_b}W(\mathbf{r}_a - \mathbf{r}_b,h) \tag{A.3}$$

The concept of the kernel function, and thereby the SPH model is shown in figure A.1

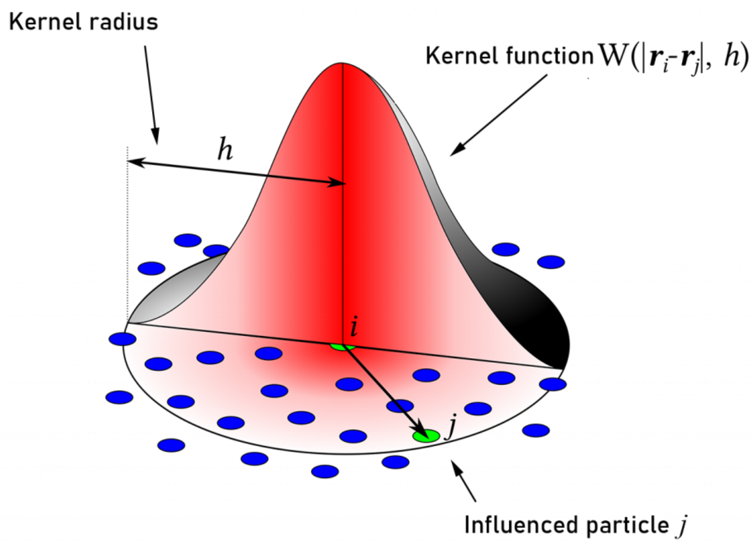

Figure A.1: Principle the kernel function shown in a 2D environment [Truong et al., 2021].

Smoothing kernel

The kernel function is a central feature of SPH, it is the function that determines the weighting of nearby particles contribution to the change of each particles physical properties. It is dependant on the non dimensional particle distance $q = r/h$ with r being the distance between two given particles. DualSPHysics is designed to use one of two kernel functions, the 4th order Wendland kernel or the cubic spline. The choice of which is central for the performance of the model. The cubic spline results in longer computation time due to its piecewise definition, but usually compensates with higher accuracy:

$$W(r,h) = \alpha_D \begin{cases} 1 - \frac{3}{2}q^2 + \frac{4}{3}q^3 & 0 \leq q \leq 1 \\ \frac{1}{4}(2-q)^3 & 1 \leq q \leq 2 \\ 0 & q \geq 2 \end{cases} \tag{A.4}$$

The Wendel kernel is the default choice of DualSPHysics and results in faster compution time:

$$W(r,h) = \alpha_D \left(1 - \frac{q}{2}\right)^4 (2q+1) \qquad 0 \leq q \leq 2 \tag{A.5}$$

In both A.4 and A.5 α_D is the normalisation constant that is dependant on the dimensions of the model and is different for the two kernels and for 2D and 3D cases:

$$\alpha_D = \begin{cases} \frac{10}{7\pi h^2} & \text{Cubic spline 2D} \\ \frac{1}{\pi h^3} & \text{Cubic spline 3D} \\ \frac{7}{4\pi h^2} & \text{Wendland 2D} \\ \frac{21}{16\pi h^3} & \text{Wendland 3D} \end{cases} \tag{A.6}$$

A.1 Governing SPH Equations

The governing equations of hydrodynamics are reformulated by principle of equation (A.3), to their descrete SPH form.

Continuity equation

Since the simulation is weakly compressible the associated density of particles changes even though each particles mass are constant. The associated density is found by solving the continuity equation for the particles. In traditional hydrodynamics the continuity equation in its differential form can be written as:

$$\frac{\mathrm{d}\rho}{\mathrm{d}t} = -\rho \nabla \cdot v \tag{A.7}$$

With v being the fluid velocity. Applying the interpolation formula (A.3), (A.7) can be rewritten as:

$$\frac{\mathrm{d}\rho_a}{\mathrm{d}t} = \rho_a \sum_b \frac{m_b}{\rho_b} \mathbf{v}_{ab} \cdot \nabla_a W_{ab} \tag{A.8}$$

With $\mathbf{v}$ being the particle velocity vector. The subscript ab denoting the difference between particle a and particle b. For velocity $\mathbf{v}_{ab} = \mathbf{v}_a - \mathbf{v}_b$, as for the subscript in combination with the kernel function $W_{ab} = W(\mathbf{r}_a - \mathbf{r}_b, h)$.

Momentum equation

The changes in fluid velocity is described by the momentum equation, which is the Navier Stokes equation for a continuum:

$$\frac{\mathrm{d}\mathbf{v}}{\mathrm{d}t} = -\frac{1}{\rho} \nabla P + \mathbf{g} + \boldsymbol{\Gamma} \tag{A.9}$$

Where:

P	Pressure
$\mathbf{g}$	Gravitational acceleration
$\boldsymbol{\Gamma}$	Dissipatetive/viscosity terms

DualSPHysics has two methods of handling viscosity: artificial viscosity, and laminar viscosity and sub particle scale turbulence. Only artificial viscosity has been used in this project, and laminar viscosity and sub particle scale tubulence with therefore not be considered.

For artificial viscosity the momentum equation (A.9), and the interpolation formula A.3 can be rewritten to its discretized form:

$$\frac{\mathrm{d}\mathbf{v}_a}{\mathrm{d}t} = -\sum_b m_b \left(\frac{P_b + P_a}{\rho_b \cdot \rho_a} + \prod_{ab} \right) \nabla_a W_{ab} + \mathbf{g} \tag{A.10}$$

The viscosity term $\prod_{ab}$ is given by:

$$\prod_{ab} = \begin{cases} \frac{1}{\rho_{ab}} \cdot \left(-\alpha \frac{c_a + c_b}{2} \frac{h \mathbf{v}_a b \cdot \mathbf{r}_{ab}}{\mathbf{r}_{ab}^2 + 0.01 h^2}\right) & \text{Cubic spline 2D} \\ \frac{1}{\pi h^3} & \text{Cubic spline 3D} \end{cases} \tag{A.11}$$

α is a dissipation coefficient. Experiments has shown that results are best with $\alpha = 0.1$

Equation of state

As stated, DualSPHysics considers the system of particles in the SPH model to be weakly compressible, relating pressure and dansity by the equation of state:

$$P = \frac{c_s^2 \rho_0}{\lambda} \cdot \left(\left(\frac{\rho}{\rho_0} \right)^{\lambda} - 1 \right) \tag{A.12}$$

where λ is the polytropic index (usually 7 for water), ρ_0 is the reference density, and the numerical speed of sound is defined as $c_s = \sqrt{\partial P / \partial \rho}$ [Domínguez et al., 2021].The system is made weakly compressible by artificially lowering the speed of sound. Therefore the speed of sound is treated as an input parameter, taken into accound by the coefficient $b = \frac{c^2 \rho_0}{\lambda}$. The artificial speed of sound must fullfill the requirement of being ten times larger than the expected maximum velocity in the model. As long as this requirement is fullfilled density variations is less than 1% and the model yields reasonable results.

In this project auto estimation of the speed of sound, and thereby b, were used. The auto estimation is based on the maximum velocity of a dam break scenario. Where the maximum velocity (the propagation of the water front) can be approximated by:

$$c_0 \approx \sqrt{g \cdot h_{swl}} \tag{A.13}$$

To make sure that eventual moving parts do not induce velocities larger than 1/10 of the speed of sound. A larger coefficient is used:

$$c = 20 \cdot \sqrt{g \cdot h_{swl}} \tag{A.14}$$

A.2 Density diffusion term (DDT)

The smoothed particle hydrodynamics method is well suited for simulation complex fluid dynamics problems when problem shows strong free surface dynamics. In general in many problems the flow speeds look quite good, but checking the distribution of pressure, the situation is different. Where large random pressure oscillations are present due to numerical high frequencies acoustic signal [Molteni and Colagrossi, 2009]. Within DualSPHysics there is an option to apply a diffusive term Ψ_{ab} to the density fluctuations on the continuity equation. In this project the Fourtakas (Full) formulation was used. It is a correction to the DDT developed by Molteni [Molteni and Colagrossi, 2009]. Where the Molteni DDT uses the dynamic density, the Fourtaka formulation uses the total and hydrodynamic densities:

$$\Psi_{ab} = 2(\rho_b^D - \rho_a^D)\frac{\mathbf{x}_{ab}}{|\mathbf{x}_{ab}|^2} \rightarrow 2(\rho_{ab}^T - \rho_{ab}^H)\frac{\mathbf{x}_{ab}}{|\mathbf{x}_{ab}|^2} \tag{A.15}$$

The subscripts "D" denotes the dynamic densities, "T" and "H" denotes total and hydrostatic density components respectively. And since $\rho_D = \rho_T - \rho_H$ the revision is acceptable form a theoretical point of view. This results in a model that is more accurate around boundaries in simulations which are gravity dominated.

A.3 Boundary conditions

DualSPHysics uses whats called the dynamic boundary condition. Simulating boundary elements as particles which needs to satisfy the same equations as the fluid particles, but they do not move when forces are exerted on them.

When a fluid particles approaches a boundary object/particle within a distance of two times the smoothing length, the density of the boundary particle(s) will increase. This in turn results in an increase of pressure due to the equation of state, and due to the momentum equation this pressure increase results in a repulsive force acting on the fluid particle.

This boundary condition can be applied to both moving and static boundaries. In a moving scenario the boundary particles are simply moved a certain distance in each time step, the effect of the boundary is then moved with it as a result. As a result of this, the dynamic boundary conditions accurafy relies heavely on the length of the time step. Since larger timesteps will induce unrealistic large repulsive forces.

A.4 Computing forces

In DualSPHysics forces exerted on boundary elements can be calculated by computing the acceleration of the individual boundary particles from the effects the surrounding fluid has on the boundary, the total force exacted on the boundary object can then be found from the sum of accelerations of the boundary particles. This is shown graphically on figure A.2.

Accelerations are found by the particle interaction:

$$\frac{d\mathbf{v}_a}{dt} = -\sum_b m_b \left(\frac{P_b}{\rho_b^2} + \frac{P_a}{\rho_a^2} + \Pi_{ab} \right) \nabla_a W_{ab} + g \tag{A.16}$$

The total force is then computed from the sum of the accelerations:

$$F = m \cdot \sum \frac{d\mathbf{v}_a}{dt} \tag{A.17}$$

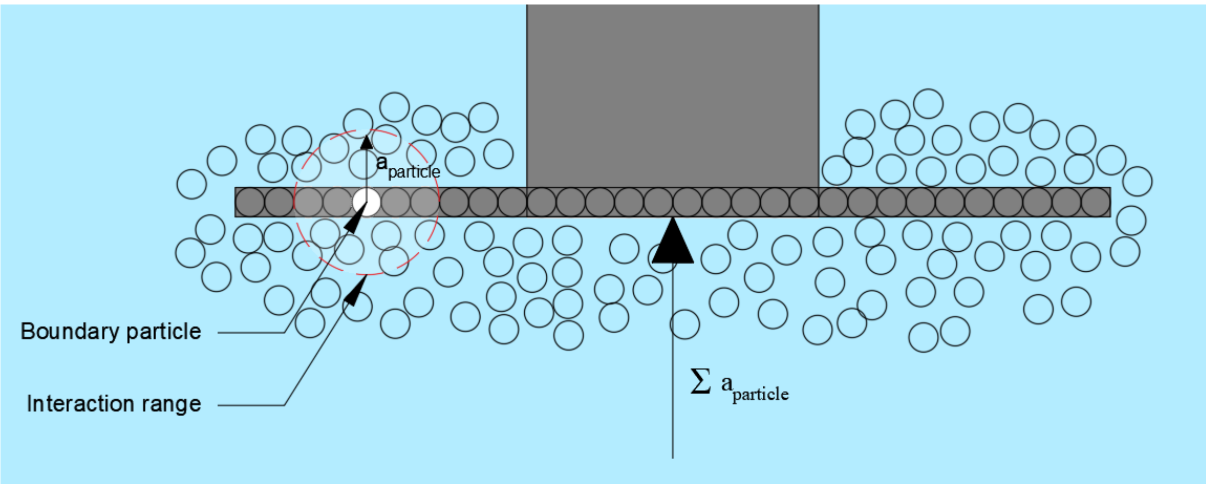

Figure A.2: Principle of force computation in DualSPHysics.

A.5 Time stepping

In DualSPHysics have implemented two different time integration schemes. These are used to integrate the governing equations in time by either using a computationally simple Verlet based scheme or a more numerically stable but computationally intensive two-stage Symplectic method. The governing equations can be seen in equation (A.18).

$$\frac{\mathrm{d}\mathbf{v_a}}{\mathrm{d}t} = F_a; \frac{\mathrm{d}\rho_a}{\mathrm{d}t} = R_a; \frac{\mathrm{d}\mathbf{r_a}}{\mathrm{d}t} = \mathbf{v_a} \tag{A.18}$$

A.5.1 Verlet time integration scheme

The Verlet time intergration scheme is often used in molecular dynamics, such as SPH, since it is a a low computational cost scheme with a second order accurate space integrator that does not require multiple calculation steps within an iteration interval [Domínguez et al., 2021]. The variables are calculated according to equation A.19.

$$\begin{aligned} \mathbf{V_a^{n+1}} &= \mathbf{V_a^{n-1}} + 2\Delta t \mathbf{F_a^n} \\ \mathbf{r_a^{n+1}} &= \mathbf{r_a^n} + \Delta t \mathbf{V}_a^n \frac{1}{2} \Delta t^2 \mathbf{F_a^n} \\ \rho_\mathbf{a}^\mathbf{n+1} &= \rho_\mathbf{a}^\mathbf{n-1} + 2\Delta t \mathbf{R_a^n} \end{aligned} \tag{A.19}$$

Due to the time integration being staggered over a time interval will it result in the equations of density and velocity being decoupled, which may lead to divergence of the integrated values. Therefore, an intermediate step is required every N_s steps. This is recommended to be done around every 40 steps.

The intermediate step can be seen in equation (A.20)

$$\begin{aligned}\mathbf{V_a^{n+1}} =& \mathbf{V_a^n} + \Delta t \mathbf{F_a^n} \\ \mathbf{r_a^{n+1}} =& \mathbf{r_a^n} + \Delta t \mathbf{V}_a^n \frac{1}{2} \Delta t^2 \mathbf{F_a^n} \\ \rho_\mathbf{a}^\mathbf{n+1} =& \rho_\mathbf{a}^\mathbf{n} + 2\Delta t \mathbf{R_a^n}\end{aligned} \tag{A.20}$$

A.5.2 Symplectic position Verlet time integration scheme

The symplectic position Verlet time integration scheme is ideal for Lagrangian schemes as it is time reversible and symmetric in the absence of diffusive terms that preserve geometric futures [Domínguez et al., 2021]. In the absence of dissipation forces will the symplectic position Verlet time integration scheme be as shown in equation (A.21).

$$\begin{aligned}\mathbf{r_a^{n+1/2}} =& \mathbf{r_a^n} + \frac{\mathbf{\Delta t}}{\mathbf{2}} \mathbf{v_a^n} \\ \mathbf{v_a^{n+1}} =& \mathbf{v_a^n} + \Delta t \mathbf{F_a^{n+1/2}} \\ \mathbf{r_a^{n+1}} =& \mathbf{r_a^{n+1/2}} + \frac{\Delta t}{2} \mathbf{v_a^{n+1}}\end{aligned} \tag{A.21}$$

In the presence of viscous forces and density evolution, is the velocity required at at the $(n+1/2)$ step thus is a velocity Verlet half step introduces, and is used to compute the required velocity for the acceleration and density evolution. The new integration scheme is shown in equation (A.22).

$$\begin{aligned}\mathbf{r_a^{n+1/2}} =& \mathbf{r_a^n} + \frac{\Delta t}{2} \mathbf{v_a^n} \\ \mathbf{v_a^{n+1/2}} =& \mathbf{v_a^n} + \frac{\Delta t}{2} \mathbf{F_a^n} \\ \mathbf{v_a^{n+1}} =& \mathbf{v_a^n} + \Delta t \mathbf{F_a^{n+1/2}} \\ \mathbf{r_a^{n+1}} =& \mathbf{r_a^n} + \Delta t \frac{\mathbf{v_a^{n+1}} + \mathbf{v_a^n}}{2}\end{aligned} \tag{A.22}$$

The density evolution follows the half time steps of the symplectic position Verlet scheme as shown in equation (A.23).

$$\begin{aligned}\rho_a^{n+1/2} =& \rho_a^n + \frac{\Delta t}{2} + \mathbf{R_a^n} \\ \rho_a^{n+1} =& \rho_a^n + \frac{2 - \varepsilon_a^{n+1/2}}{2 + \varepsilon_a^{n+1/2}} \\ \varepsilon_a^{n+1/2} =& -(R_a^{n+1/2} / \rho_a^{n+1/2}) \Delta t\end{aligned} \tag{A.23}$$

Estimating added mass and damping factor B

From a forced oscillation test of a structure, where the structure oscillate sinusoidally at a frequency. Time series for motion and force are analyzed and the total oscillating mass and the linearised damping can be estimated by a least-squares method, using equation (B.1). Where the added mass, A, can be found by subtracting the structural mass of the structure. [DNV GL A/S, 2011]

$$F(t) = -(M + A)\ddot{z}(t) - B|\dot{z}(t)|\dot{z}(t) \tag{B.1}$$

Where:

$F(t)$	Time series for force
M	Structural mass
A	Added mass
$z(t)$	Time series for motion
B	Linearised damping

The movement, velocity and acceleration of the sinusoidal movement are defined as in equation (B.2). Notably the acceleration and velocity is negative compared to the actual derivatives of the movement function. This is done because particle movements are the negatives of the heave plate movements.

$$\begin{aligned} z(t) &= a\sin(\phi + 2\pi f t) \\ \dot{z}(t) &= -2\pi a f\cos(\phi + 2\pi f t) \\ \ddot{z}(t) &= 4af^2\pi^2\sin(\phi + 2\pi f t) \end{aligned} \tag{B.2}$$

Where:

a	is acceleration
f	is frequency in [Hz]
ϕ	is the phase shift

As an example the method is used on the results from the theoretical model described in 2.1. Input parameters are: $r_d = 0.15$m, $t_d = 0.01$m, $a = 0.1$m, $f = 0.2$Hz, $m_a = 9$kg, $V_R = 0.0141\text{m}^3, C_d = 1.12$ and $C_a = 0.64$. Equation B.1 is then used with the least squares method to fit to the model data. See figure B.1.

The fitting parameters A and B are then found to $A = 23.13$ and $B = 39.58$. Notably A is not equal to the added mass input of the model, this is because A is the added mass corresponding to the value of inertia coefficient C_m Which is used to find the real value of the added mass m_a:

$$C_m = C_a + 1 = \frac{m_a}{\rho V_R} + 1 = \frac{A}{\rho V_R} \rightarrow m_a = A - \rho\, V_R = 9\text{kg} \tag{B.3}$$

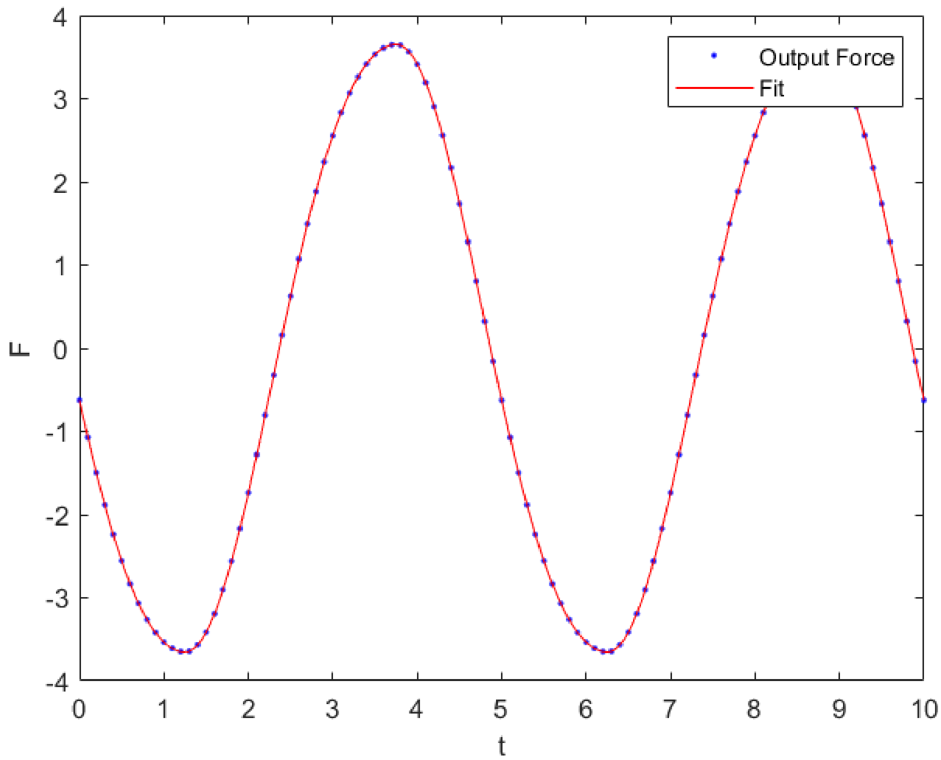

Figure B.1: Visualisation of the fit with force time series.

Which is the same value as the input. To compare the value of B to the input value the drag coefficient is calculated:

$$C_d = \frac{2B}{\rho A_p} = 1.12 \tag{B.4}$$

Where A_p is the projected area of the object normal to the direction of oscillation, in this case, the area of the disc. Resulting in $C_d = 1.12$, the same value as the input.

Calibration of Load cell C

The VETEK TS-100kg load cell was calibrated by changing the output gain and offset to fit the expected maximum and minimum tensile loads it is subjected to. The minimum tensile load is the weight of the heave plate configuration with the smallest radius $r_d = 100\,\text{mm}$ at $F_{t,min} = 33.11\,\text{N}$ and the maximum expected load, is based on the results of the theoretical model $F_{t,max} \approx 150\,\text{N}$. The gain is set to 0.28mV/V and offset is set to 23%. Resulting in output voltages for the minimum and maximum expected tensile loads of $V_{min} = -0.189\text{V}$ and $V_{max} = -7.208\text{V}$. Since the data collection device is configured to only read signals between -10 and $10\,\text{V}$, this leaves room for the experiment to yield forces larger than the expected values in both tension and compression.

To produce a translation function between outputs of the load cell and the applied load. The load cell was subjected to a series of loads. The outputs for each of the loads were recorded and linear regression by the method of least squares is used to approximate the translation function. See figure C.1.

$$f(x) = -16.6543x + 29.9669\ [N] \tag{C.1}$$

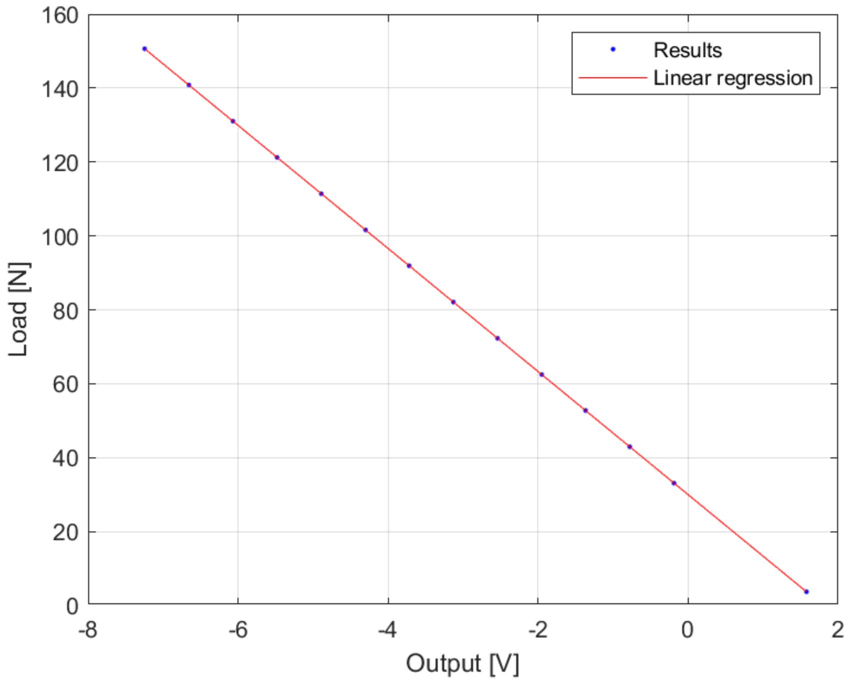

Figure C.1: Fit of the translation function to the calibration data.

Results D

Here the results from the experiment (filtered), SPH, and theoretical data from the formulation based on [DNV GL A/S, 2011] are shown for five seconds. The data has been synchronised based on movement of the heave plate, and the time 0 is the point where the heave plate is in the 0 position on the way down. All experiments that where excluded following the phenomenons described in section 3.5 are displayed with dashed magenta lines.

D.1 Ordinary

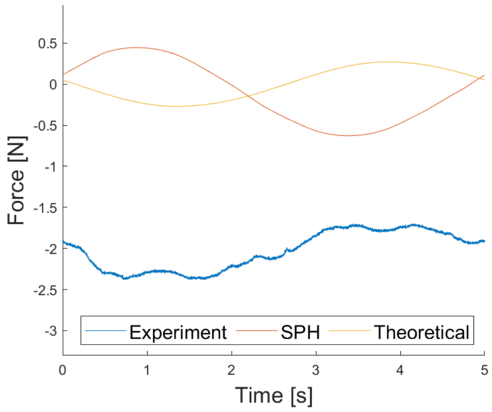

Figure D.1: r_d=100 mm, a=25 mm, f=0.2 Hz

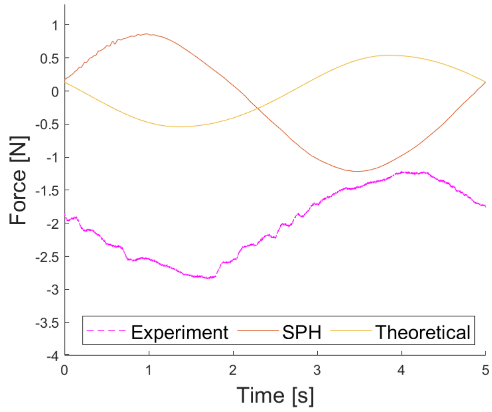

Figure D.2: r_d=100 mm, a=50 mm, f=0.2 Hz

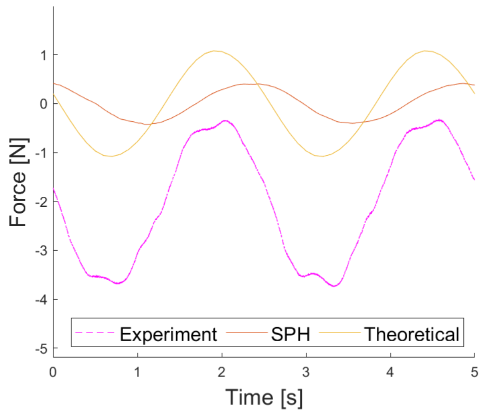

Figure D.3: r_d=100 mm, a=25 mm, f=0.4 Hz

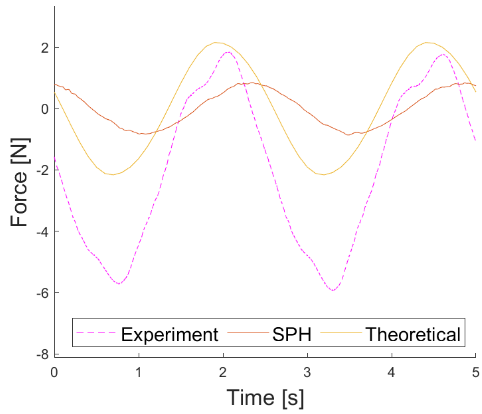

Figure D.4: r_d=100 mm, a=50 mm, f=0.4 Hz

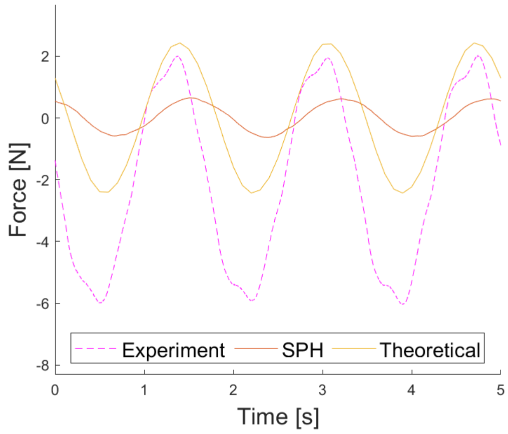

Figure D.5: r_d=100 mm, a=25 mm, f=0.6 Hz

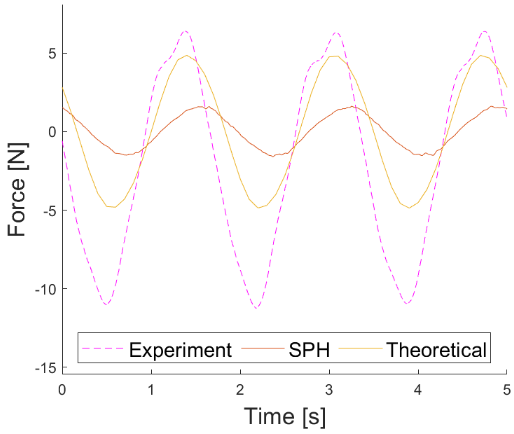

Figure D.6: r_d=100 mm, a=50 mm, f=0.6 Hz

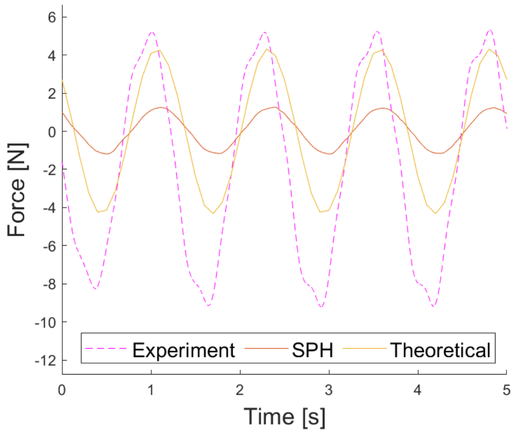

Figure D.7: r_d=100 mm, a=25 mm, f=0.8 Hz

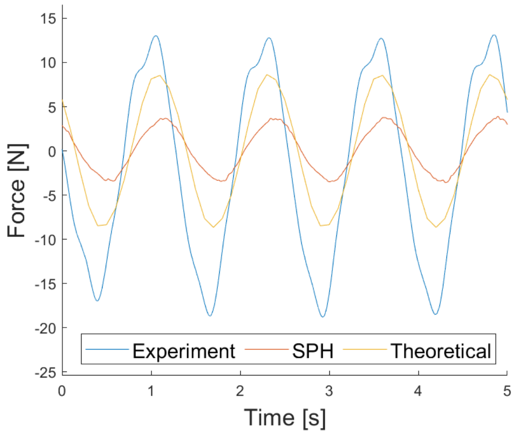

Figure D.8: r_d=100 mm, a=50 mm, f=0.8 Hz

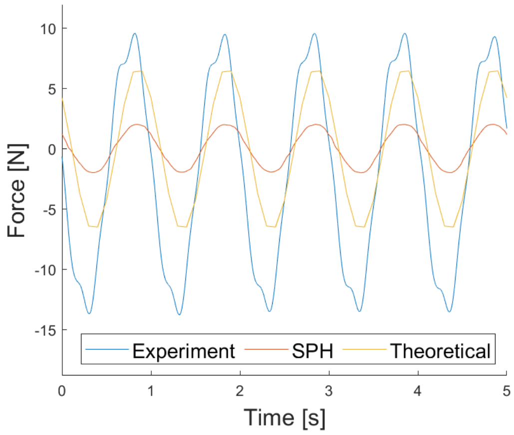

Figure D.9: r_d=100 mm, a=25 mm, f=1 Hz

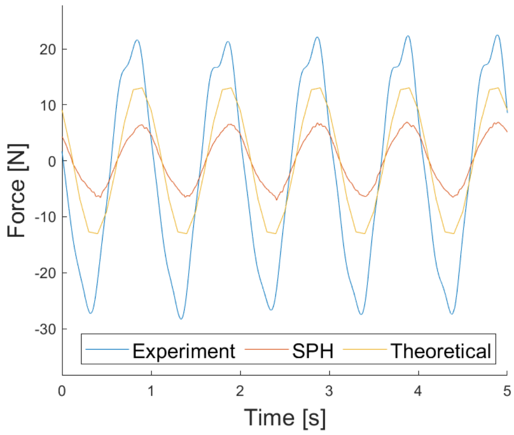

Figure D.10: r_d=100 mm, a=50 mm, f=1 Hz

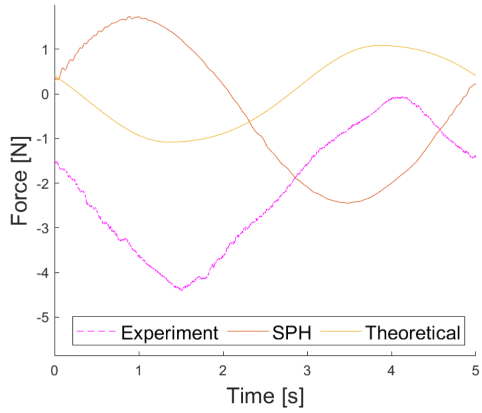

Figure D.11: r_d=100 mm, a=100 mm, f=0.2 Hz

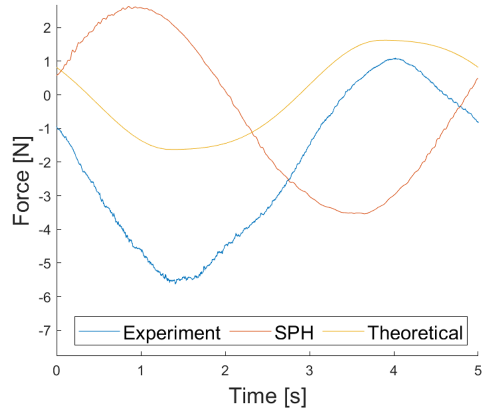

Figure D.12: r_d=100 mm, a=150 mm, f=0.2 Hz

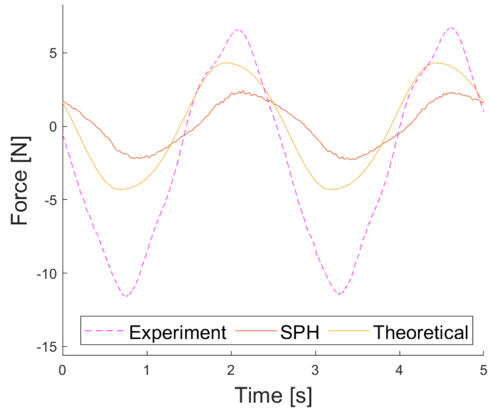

Figure D.13: r_d=100 mm, a=100 mm, f=0.4 Hz

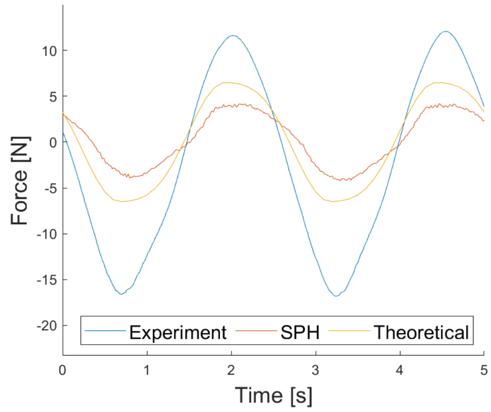

Figure D.14: r_d=100 mm, a=150 mm, f=0.4 Hz

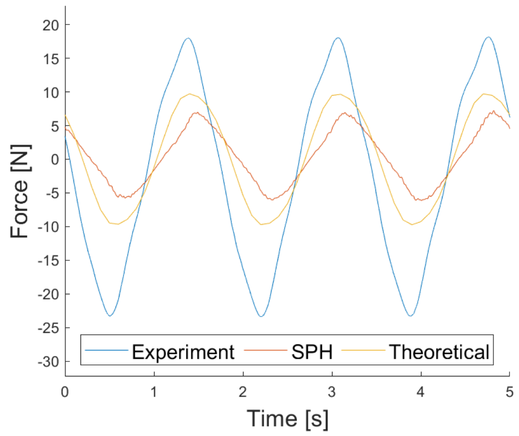

Figure D.15: r_d=100 mm, a=100 mm, f=0.6 Hz

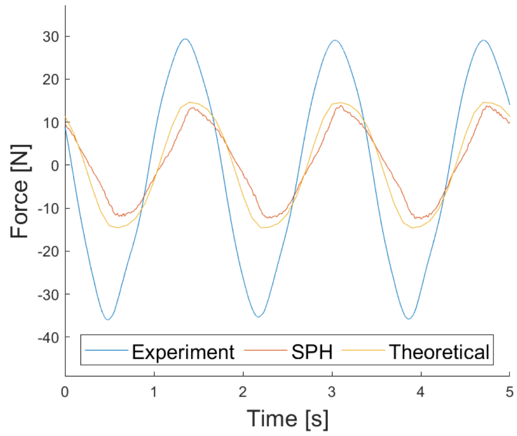

Figure D.16: r_d=100 mm, a=150 mm, f=0.6 Hz

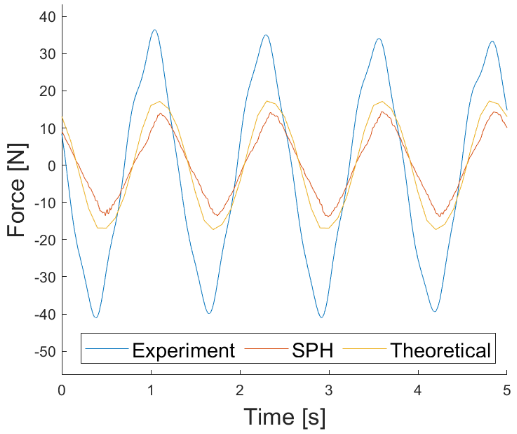

Figure D.17: r_d=100 mm, a=100 mm, f=0.8 Hz

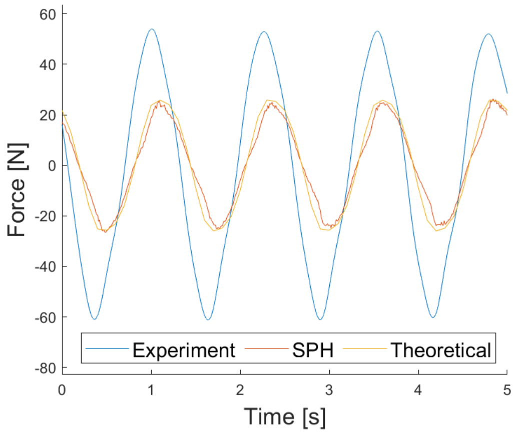

Figure D.18: r_d=100 mm, a=150 mm, f=0.8 Hz

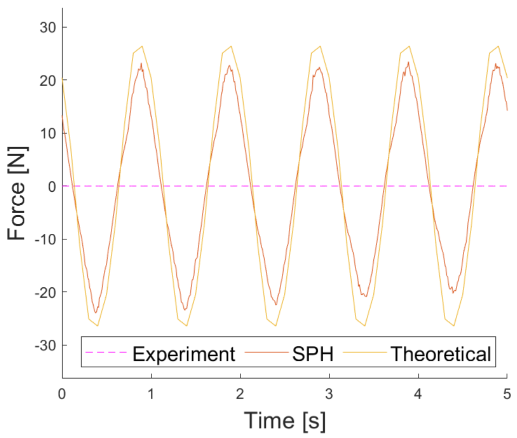

Figure D.19: r_d=100 mm, a=100 mm, f=1 Hz

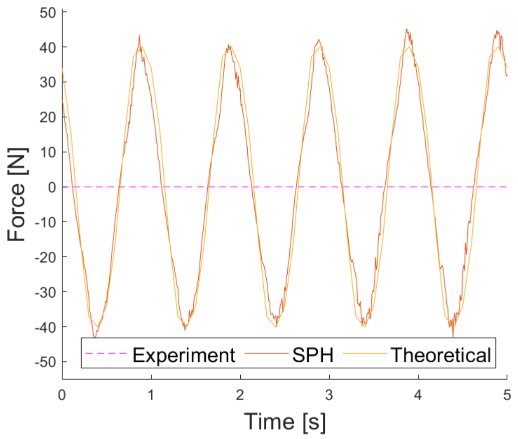

Figure D.20: r_d=100 mm, a=150 mm, f=1 Hz

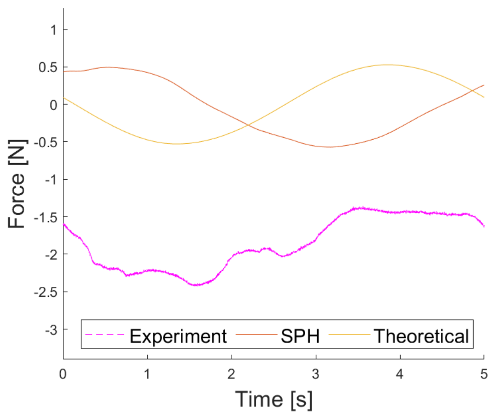

Figure D.21: r_d=125 mm, a=25 mm, f=0.2 Hz

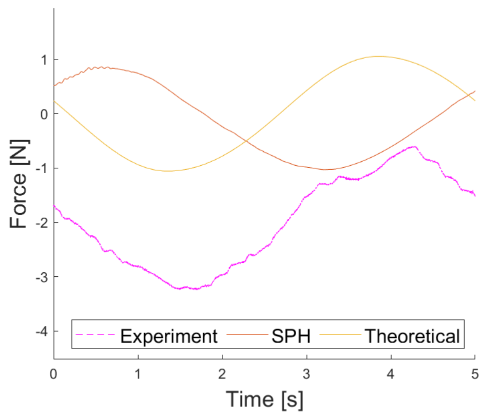

Figure D.22: r_d=125 mm, a=50 mm, f=0.2 Hz

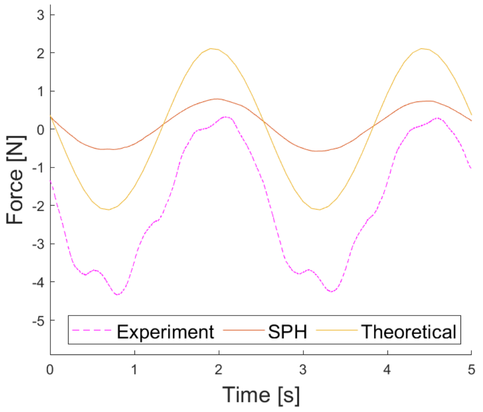

Figure D.23: r_d=125 mm, a=25 mm, f=0.4 Hz

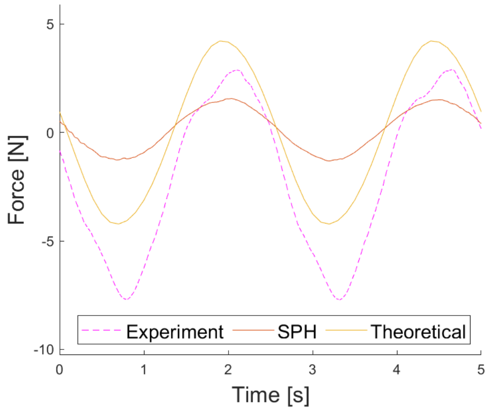

Figure D.24: r_d=125 mm, a=50 mm, f=0.4 Hz

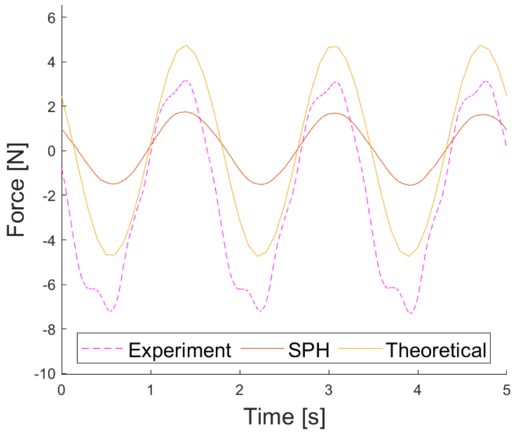

Figure D.25: r_d=125 mm, a=25 mm, f=0.6 Hz

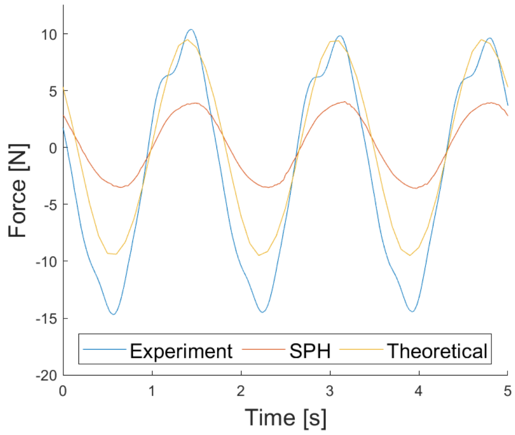

Figure D.26: r_d=125 mm, a=50 mm, f=0.6 Hz

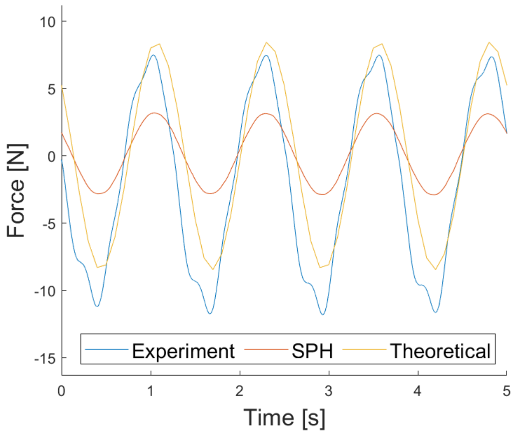

Figure D.27: r_d=125 mm, a=25 mm, f=0.8 Hz

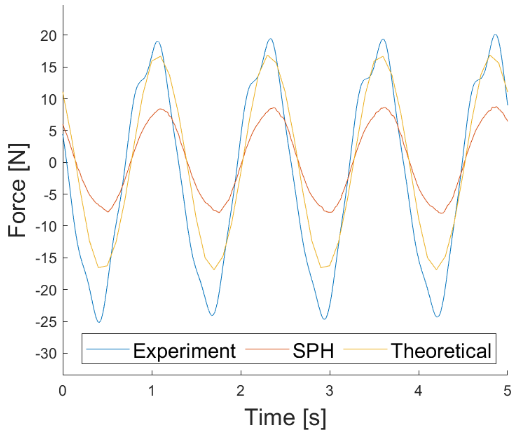

Figure D.28: r_d=125 mm, a=50 mm, f=0.8 Hz

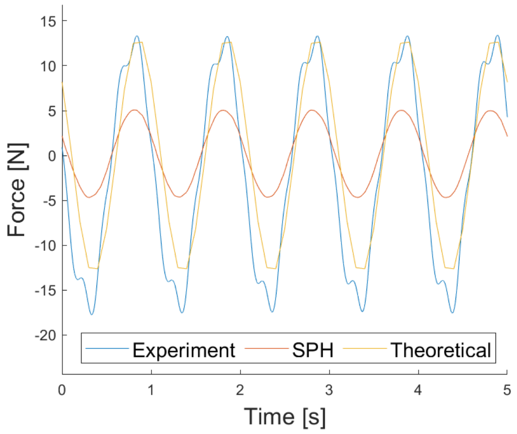

Figure D.29: r_d=125 mm, a=25 mm, f=1 Hz

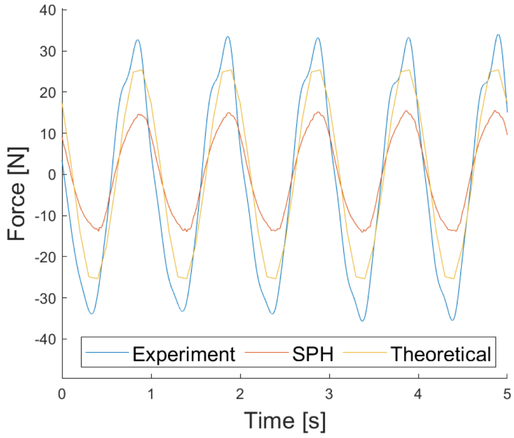

Figure D.30: r_d=125 mm, a=50 mm, f=1 Hz

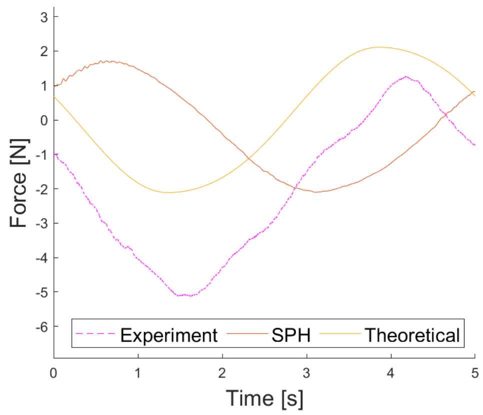

Figure D.31: r_d=125 mm, a=100 mm, f=0.2 Hz

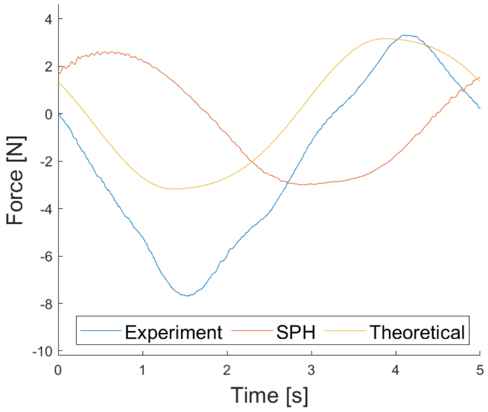

Figure D.32: r_d=125 mm, a=150 mm, f=0.2 Hz

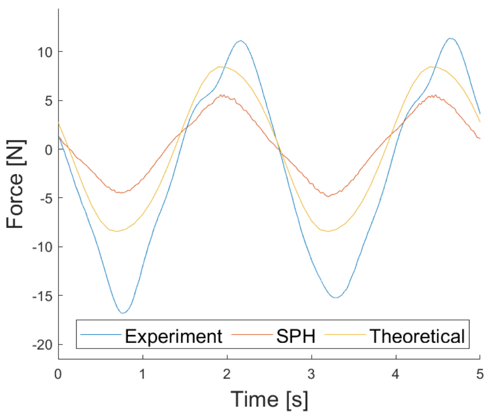

Figure D.33: r_d=125 mm, a=100 mm, f=0.4 Hz

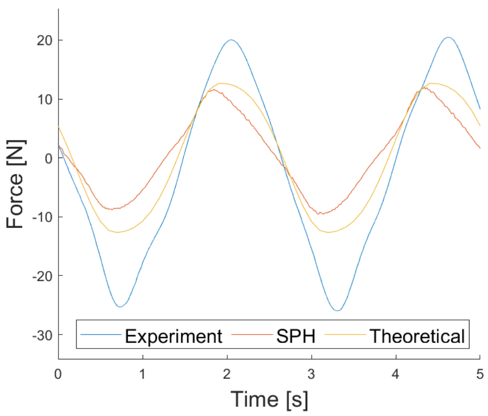

Figure D.34: r_d=125 mm, a=150 mm, f=0.4 Hz

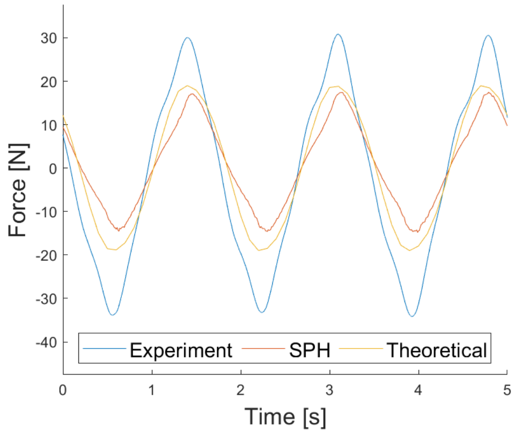

Figure D.35: r_d=125 mm, a=100 mm, f=0.6 Hz

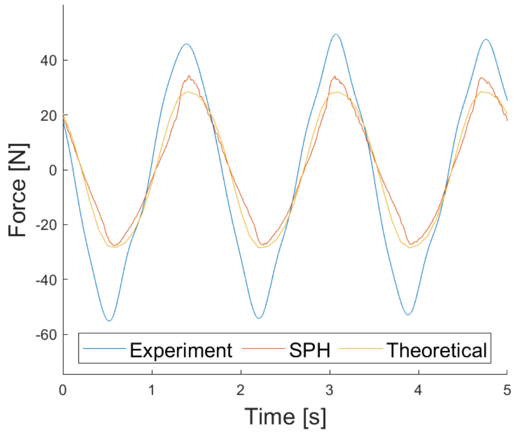

Figure D.36: r_d=125 mm, a=150 mm, f=0.6 Hz

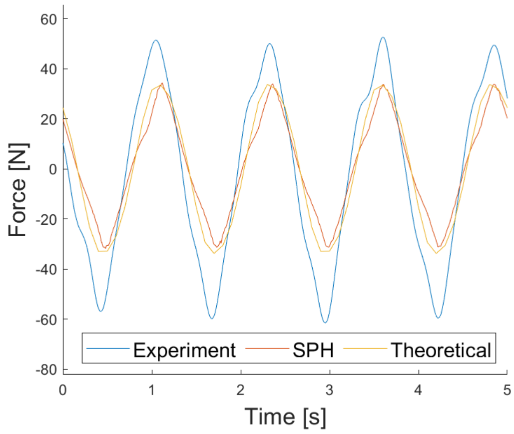

Figure D.37: r_d=125 mm, a=100 mm, f=0.8 Hz

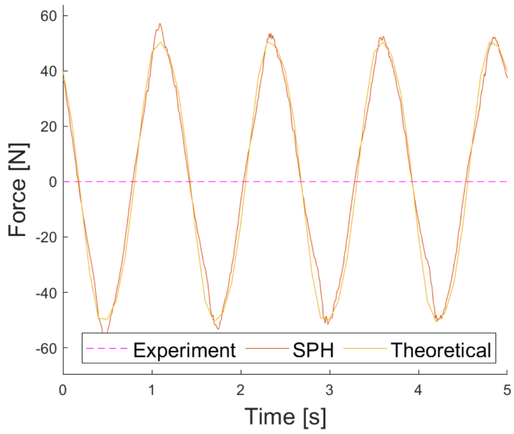

Figure D.38: r_d=125 mm, a=150 mm, f=0.8 Hz

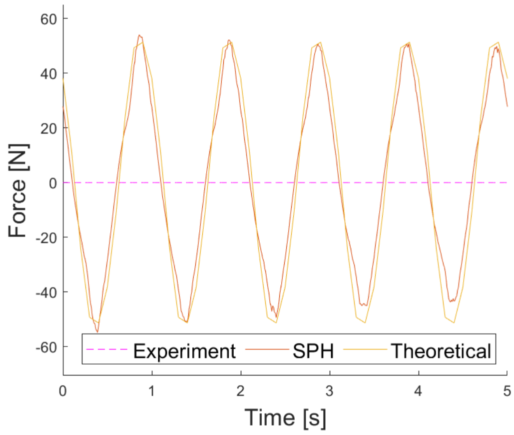

Figure D.39: r_d=125 mm, a=100 mm, f=1 Hz

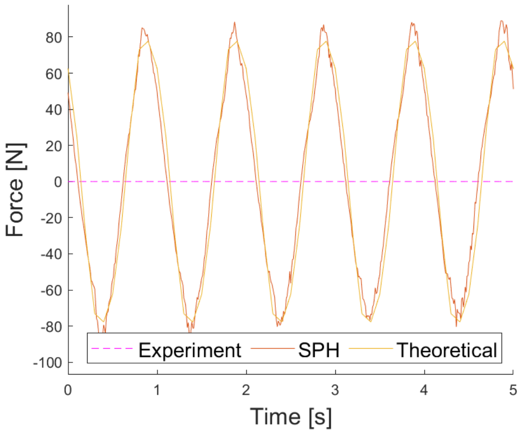

Figure D.40: r_d=125 mm, a=150 mm, f=1 Hz

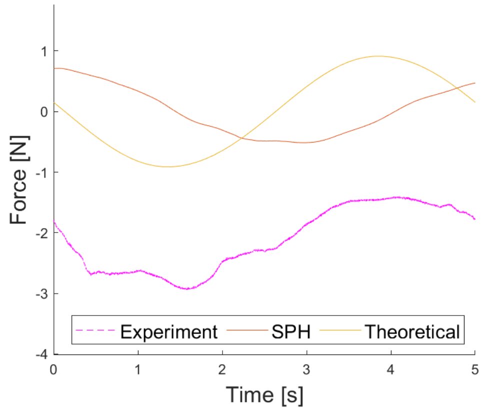

Figure D.41: r_d=150 mm, a=25 mm, f=0.2 Hz

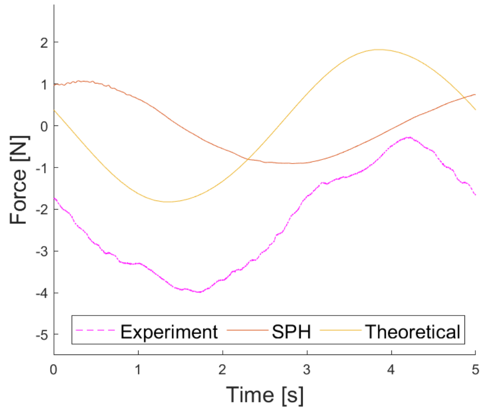

Figure D.42: r_d=150 mm, a=50 mm, f=0.2 Hz

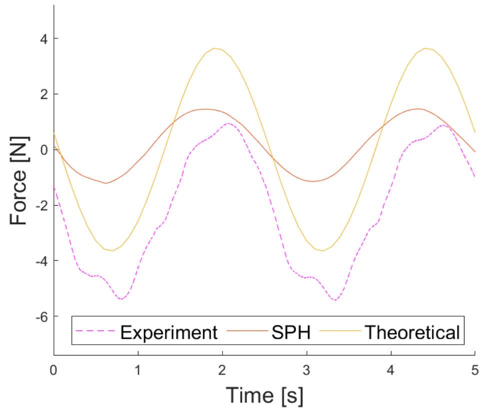

Figure D.43: r_d=150 mm, a=25 mm, f=0.4 Hz

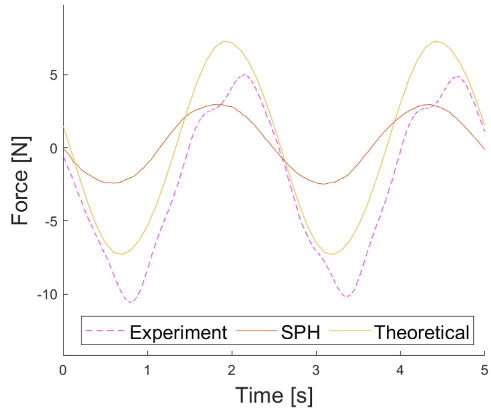

Figure D.44: r_d=150 mm, a=50 mm, f=0.4 Hz

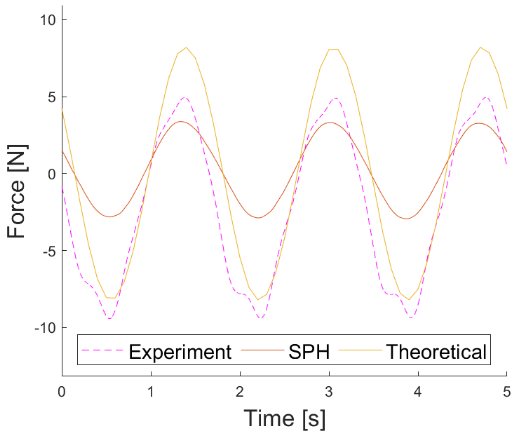

Figure D.45: r_d=150 mm, a=25 mm, f=0.6 Hz

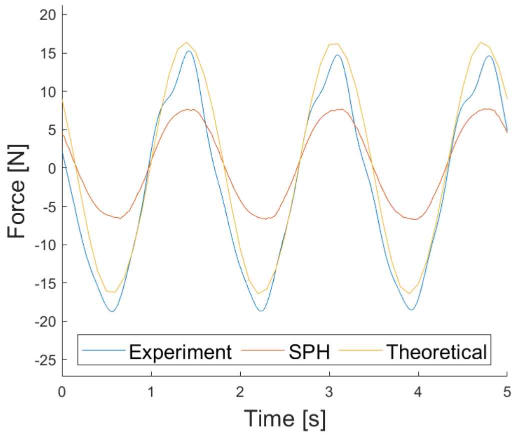

Figure D.46: r_d=150 mm, a=50 mm, f=0.6 Hz

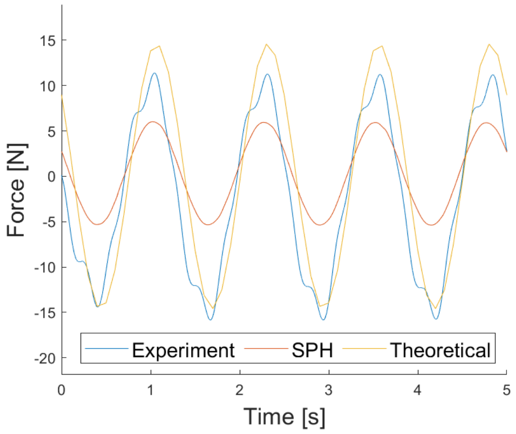

Figure D.47: r_d=150 mm, a=25 mm, f=0.8 Hz

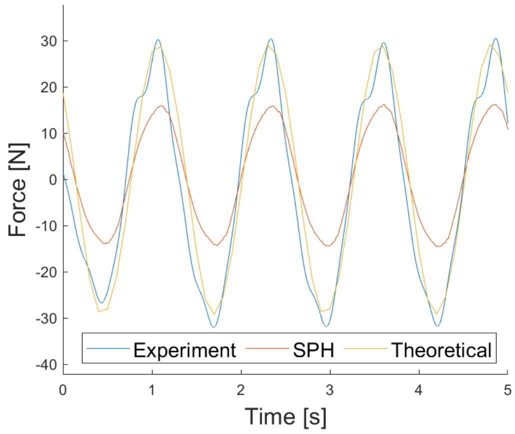

Figure D.48: r_d=150 mm, a=50 mm, f=0.8 Hz

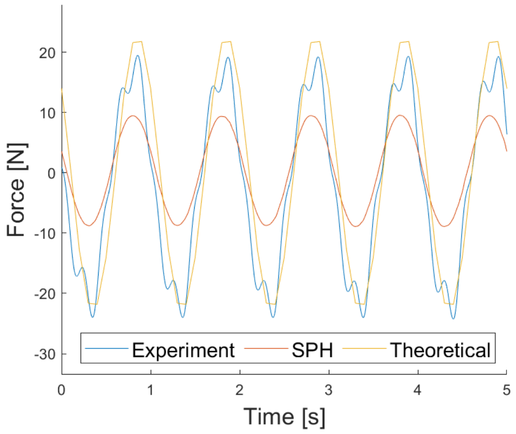

Figure D.49: r_d=150 mm, a=25 mm, f=1 Hz

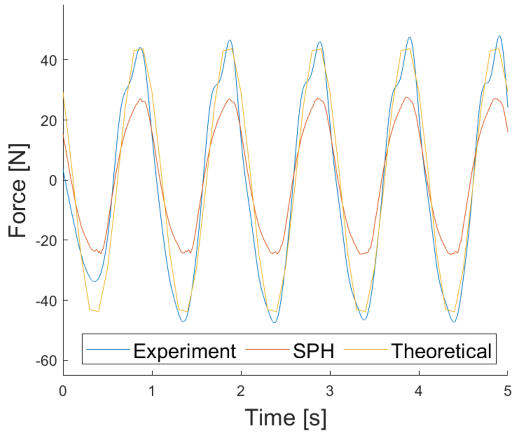

Figure D.50: r_d=150 mm, a=50 mm, f=1 Hz

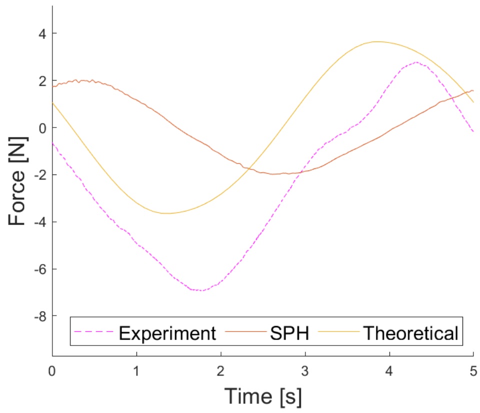

Figure D.51: r_d=150 mm, a=100 mm, f=0.2 Hz

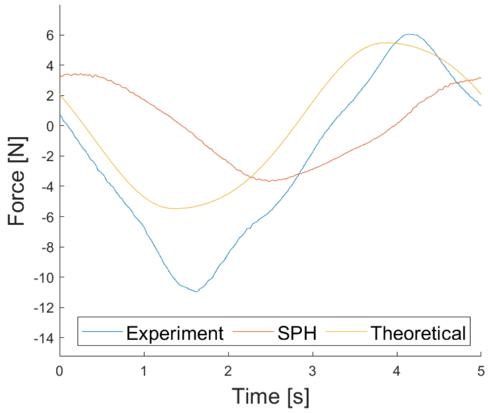

Figure D.52: r_d=150 mm, a=150 mm, f=0.2 Hz

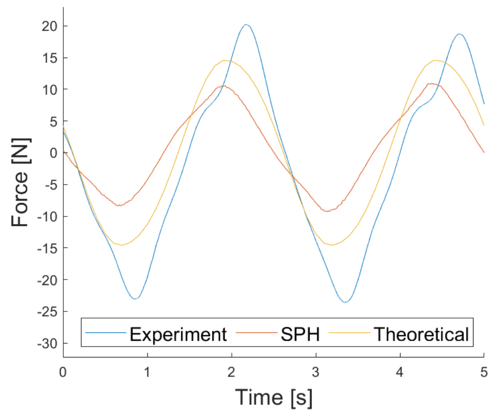

Figure D.53: r_d=150 mm, a=100 mm, f=0.4 Hz

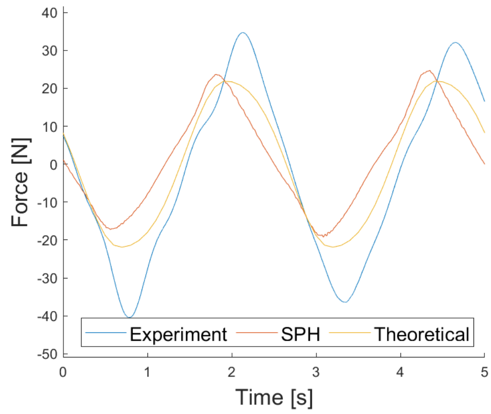

Figure D.54: r_d=150 mm, a=150 mm, f=0.4 Hz

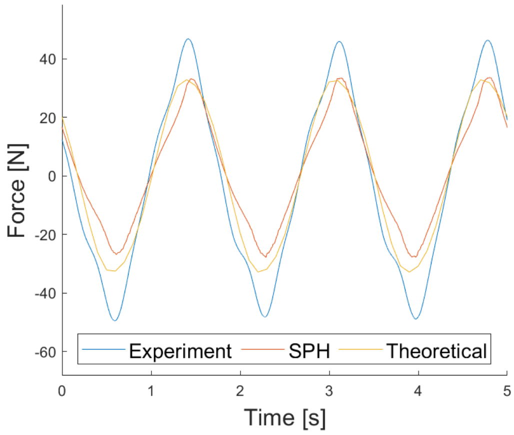

Figure D.55: r_d=150 mm, a=100 mm, f=0.6 Hz

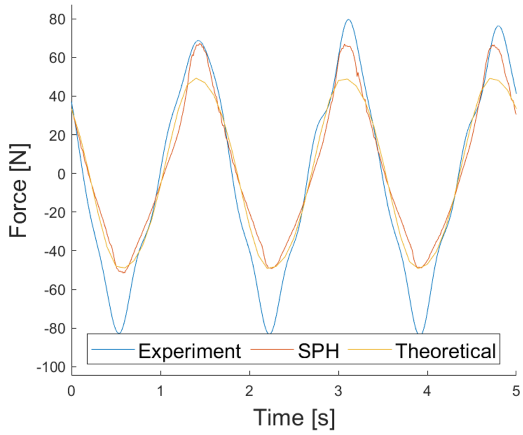

Figure D.56: r_d=150 mm, a=150 mm, f=0.6 Hz

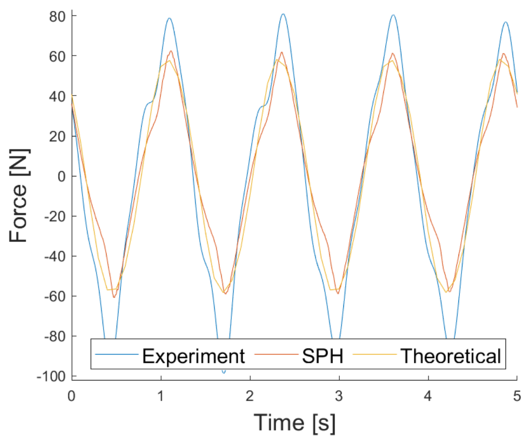

Figure D.57: r_d=150 mm, a=100 mm, f=0.8 Hz

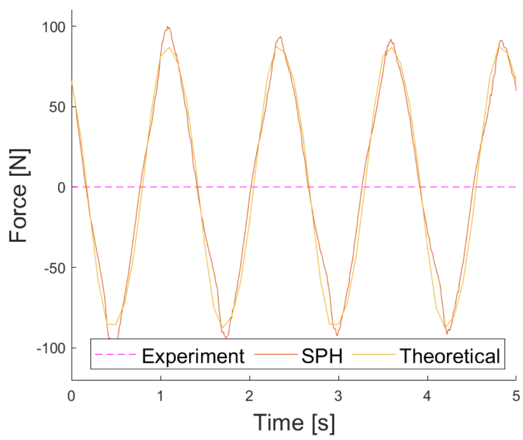

Figure D.58: r_d=150 mm, a=150 mm, f=0.8 Hz

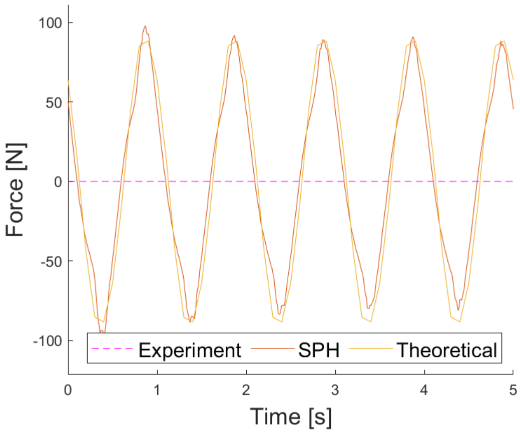

Figure D.59: r_d=150 mm, a=100 mm, f=1 Hz

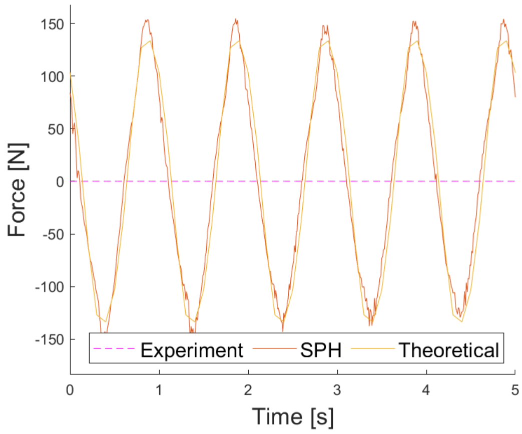

Figure D.60: r_d=150 mm, a=150 mm, f=1 Hz

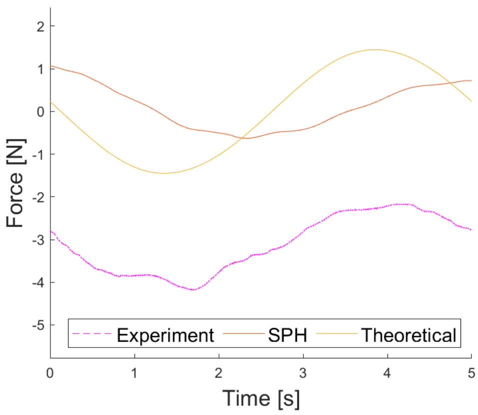

Figure D.61: r_d=175 mm, a=25 mm, f=0.2 Hz

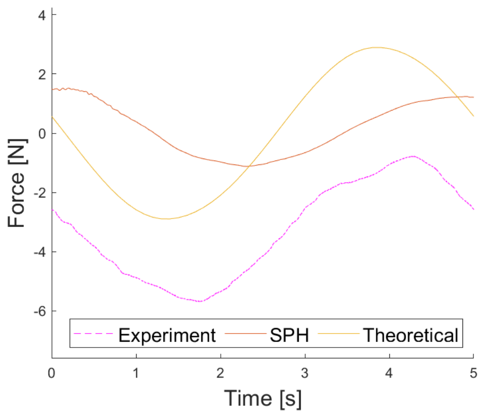

Figure D.62: r_d=175 mm, a=50 mm, f=0.2 Hz

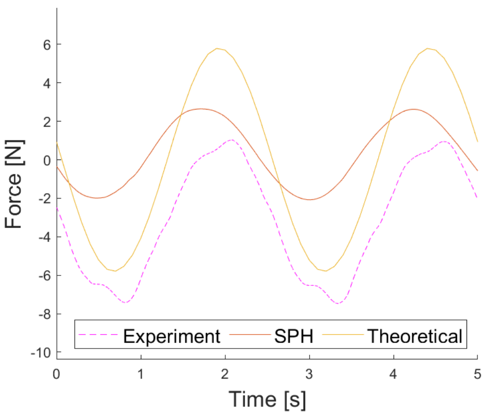

Figure D.63: r_d=175 mm, a=25 mm, f=0.4 Hz

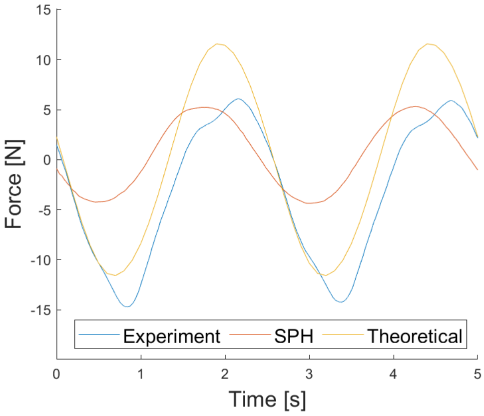

Figure D.64: r_d=175 mm, a=50 mm, f=0.4 Hz

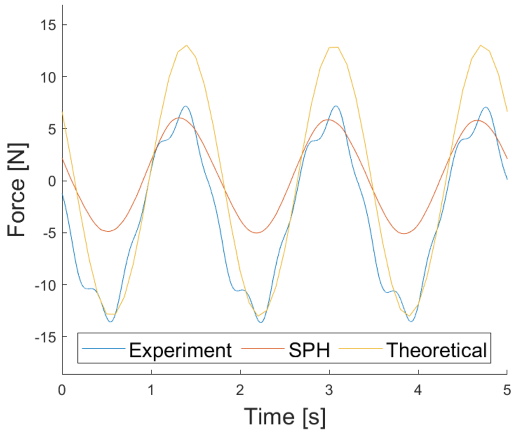

Figure D.65: r_d=175 mm, a=25 mm, f=0.6 Hz

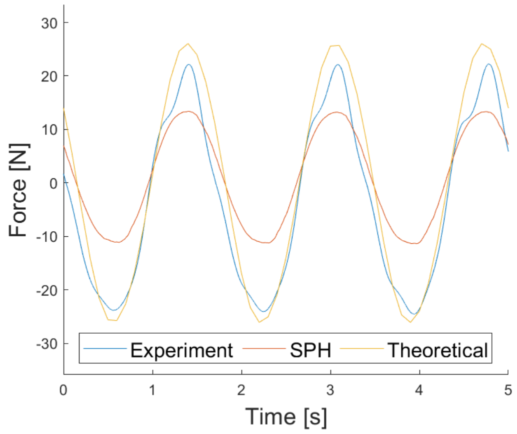

Figure D.66: r_d=175 mm, a=50 mm, f=0.6 Hz

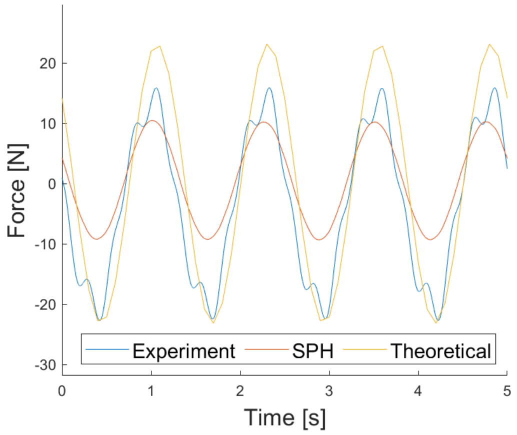

Figure D.67: r_d=175 mm, a=25 mm, f=0.8 Hz

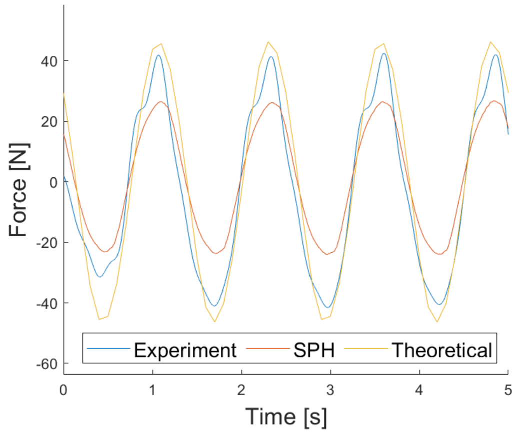

Figure D.68: r_d=175 mm, a=50 mm, f=0.8 Hz

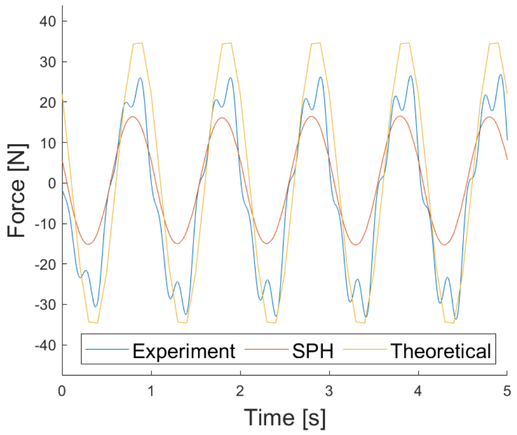

Figure D.69: r_d=175 mm, a=25 mm, f=1 Hz

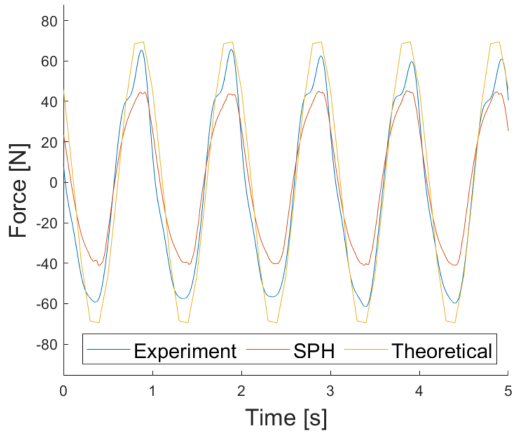

Figure D.70: r_d=175 mm, a=50 mm, f=1 Hz

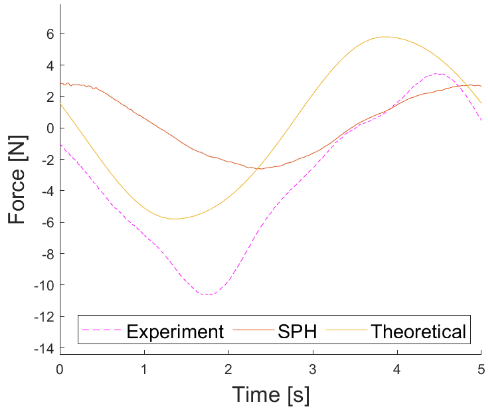

Figure D.71: r_d=175 mm, a=100 mm, f=0.2 Hz

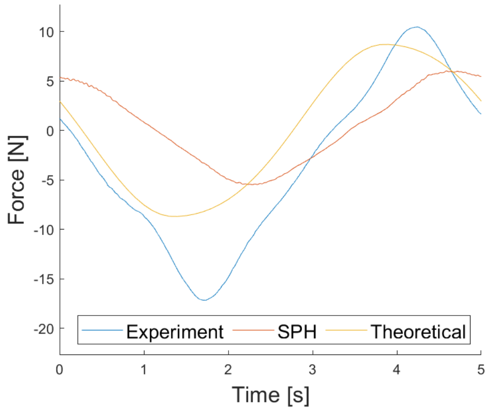

Figure D.72: r_d=175 mm, a=150 mm, f=0.2 Hz

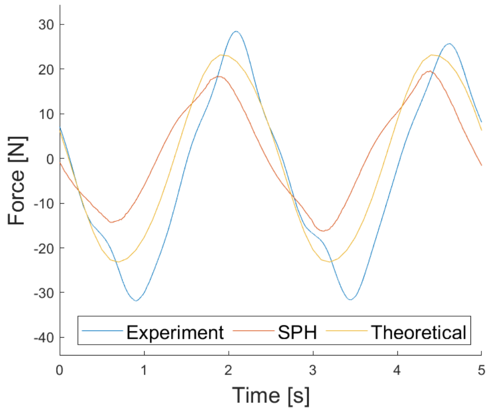

Figure D.73: r_d=175 mm, a=100 mm, f=0.4 Hz

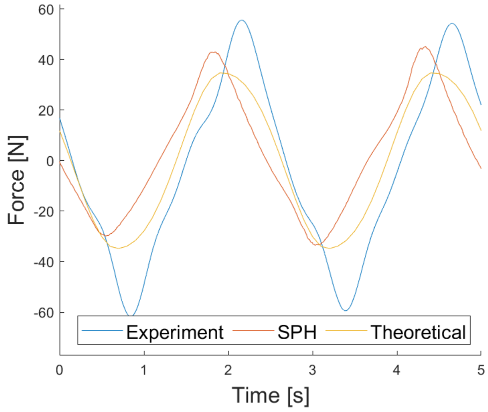

Figure D.74: r_d=175 mm, a=150 mm, f=0.4 Hz

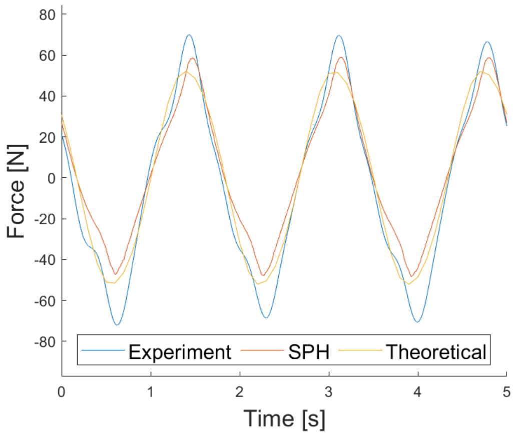

Figure D.75: r_d=175 mm, a=100 mm, f=0.6 Hz

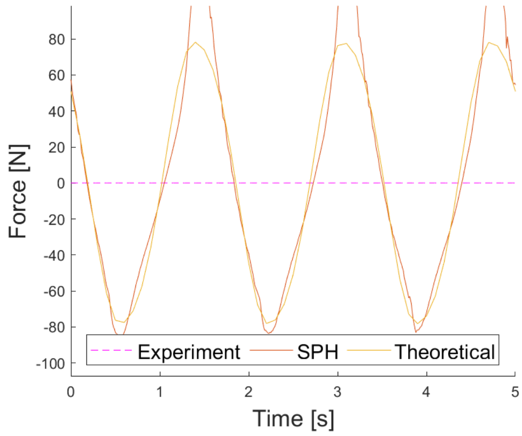

Figure D.76: r_d=175 mm, a=150 mm, f=0.6 Hz

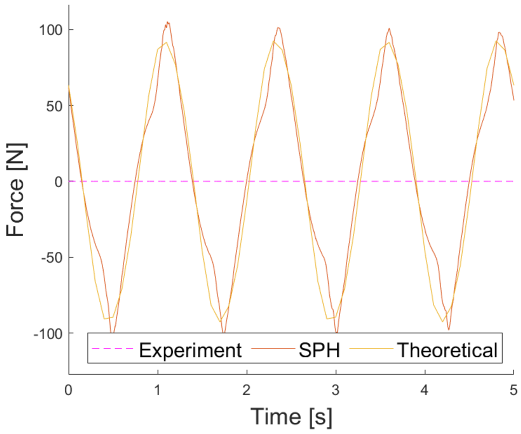

Figure D.77: r_d=175 mm, a=100 mm, f=0.8 Hz

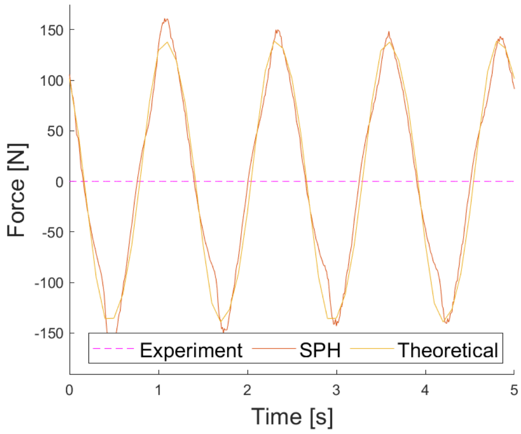

Figure D.78: r_d=175 mm, a=150 mm, f=0.8 Hz

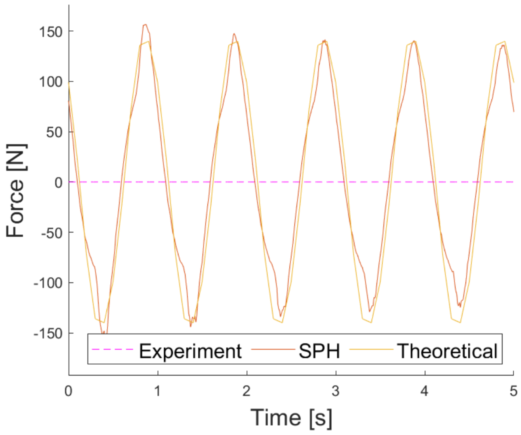

Figure D.79: r_d=175 mm, a=100 mm, f=1 Hz

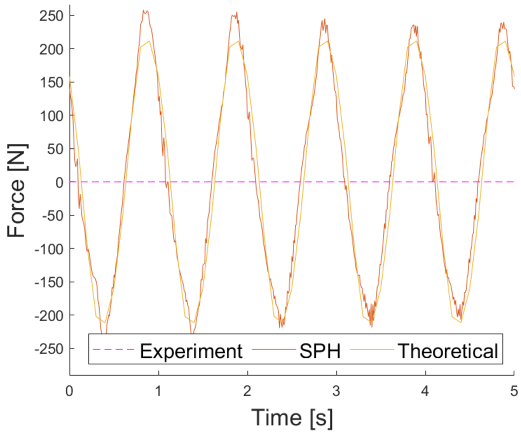

Figure D.80: r_d=175 mm, a=150 mm, f=1 Hz

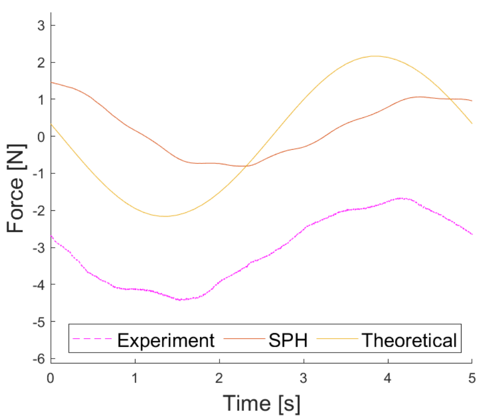

Figure D.81: r_d=200 mm, a=25 mm, f=0.2 Hz

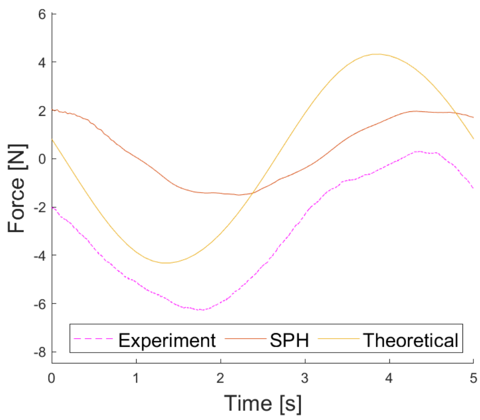

Figure D.82: r_d=200 mm, a=50 mm, f=0.2 Hz

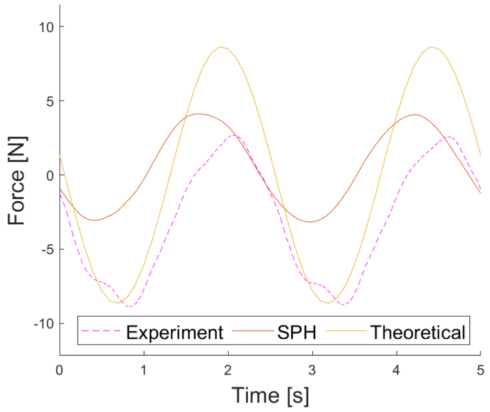

Figure D.83: r_d=200 mm, a=25 mm, f=0.4 Hz

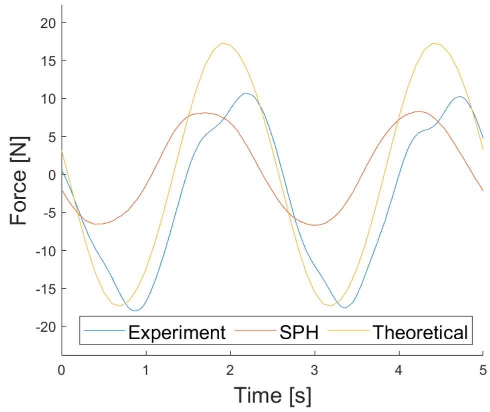

Figure D.84: r_d=200 mm, a=50 mm, f=0.4 Hz

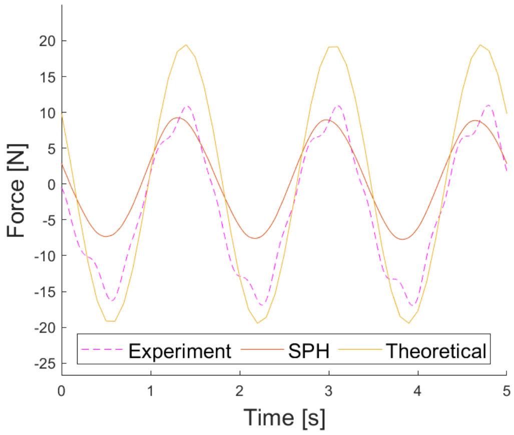

Figure D.85: r_d=200 mm, a=25 mm, f=0.6 Hz

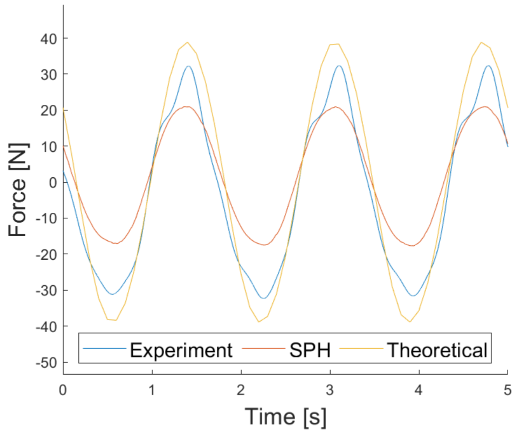

Figure D.86: r_d=200 mm, a=50 mm, f=0.6 Hz

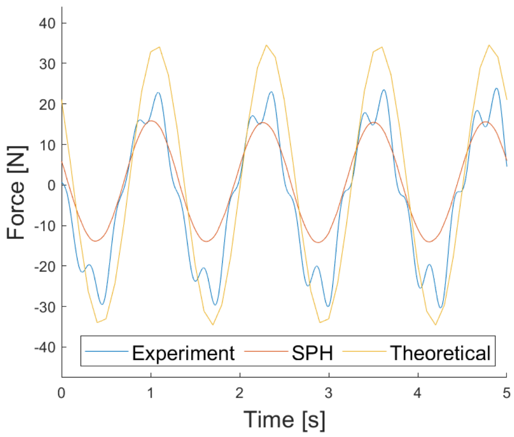

Figure D.87: r_d=200 mm, a=25 mm, f=0.8 Hz

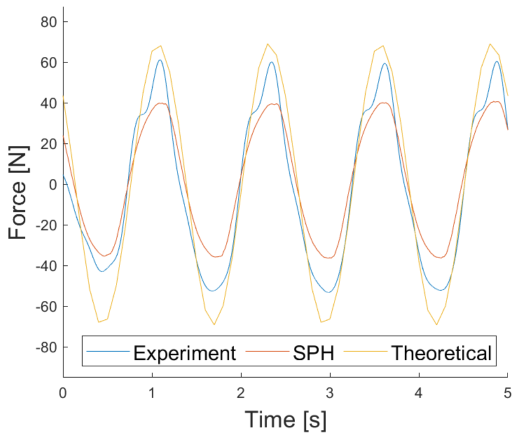

Figure D.88: r_d=200 mm, a=50 mm, f=0.8 Hz

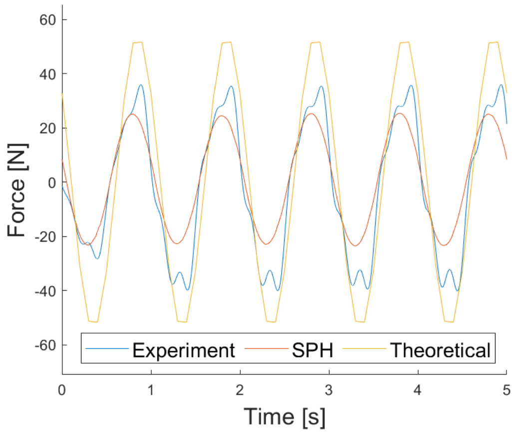

Figure D.89: r_d=200 mm, a=25 mm, f=1 Hz

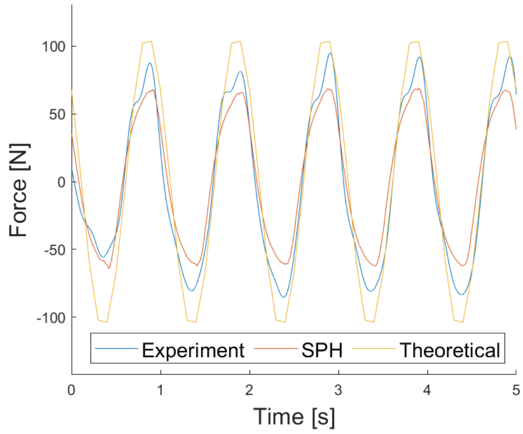

Figure D.90: r_d=200 mm, a=50 mm, f=1 Hz

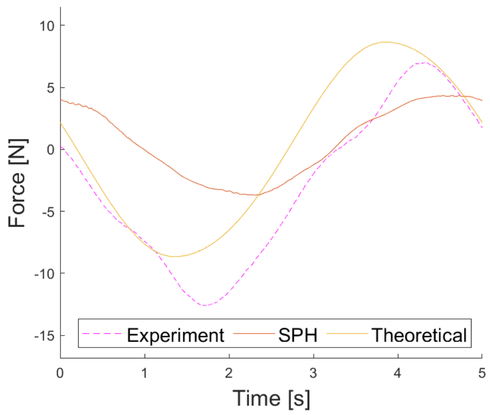

Figure D.91: r_d=200 mm, a=100 mm, f=0.2 Hz

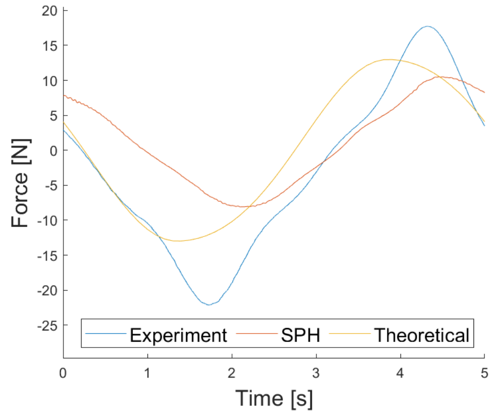

Figure D.92: r_d=200 mm, a=150 mm, f=0.2 Hz

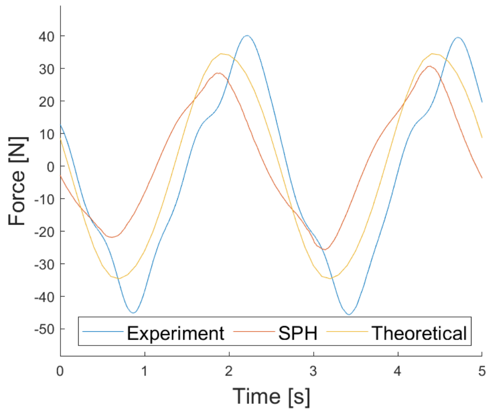

Figure D.93: r_d=200 mm, a=100 mm, f=0.4 Hz

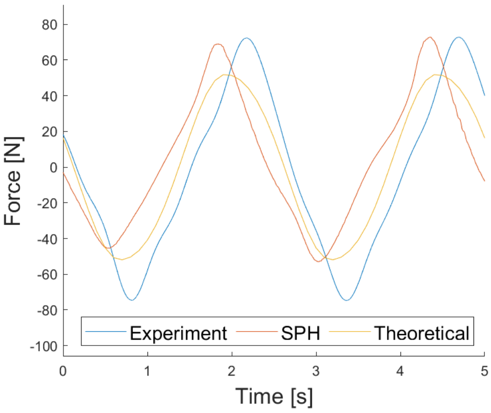

Figure D.94: r_d=200 mm, a=150 mm, f=0.4 Hz

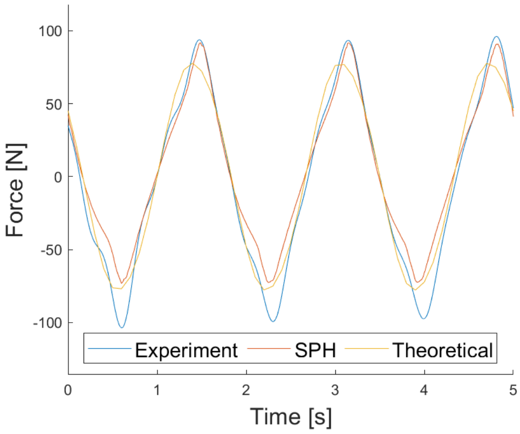

Figure D.95: r_d=200 mm, a=100 mm, f=0.6 Hz

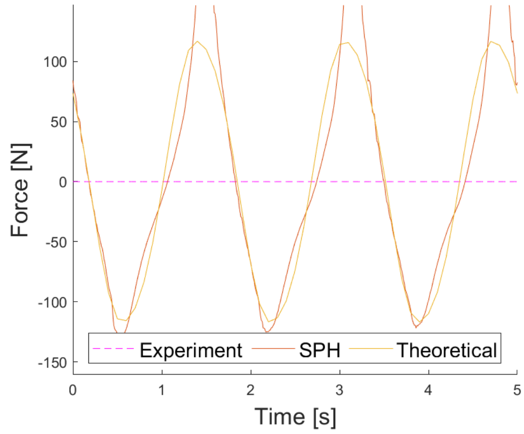

Figure D.96: r_d=200 mm, a=150 mm, f=0.6 Hz

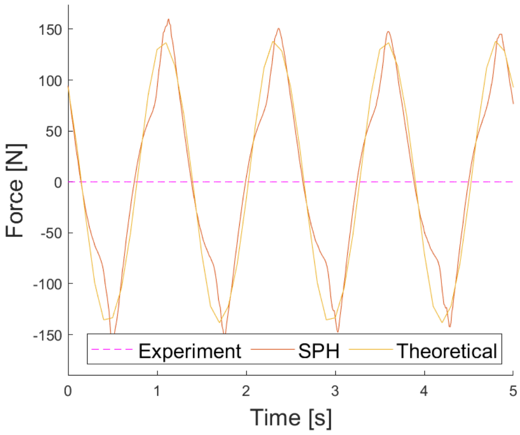

Figure D.97: r_d=200 mm, a=100 mm, f=0.8 Hz

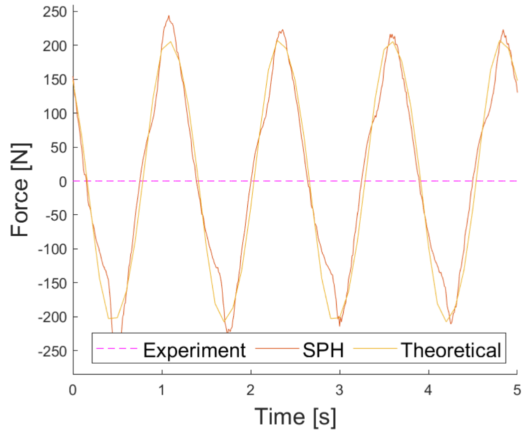

Figure D.98: r_d=200 mm, a=150 mm, f=0.8 Hz

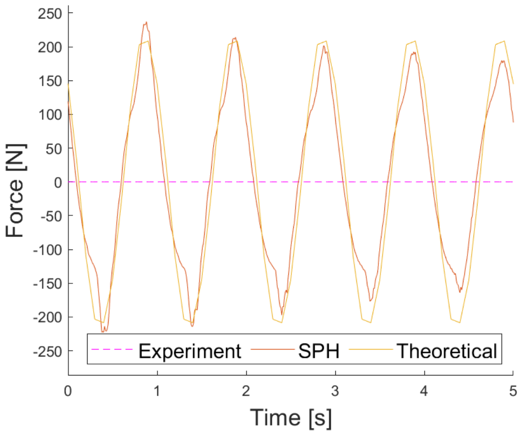

Figure D.99: r_d=200 mm, a=100 mm, f=1 Hz

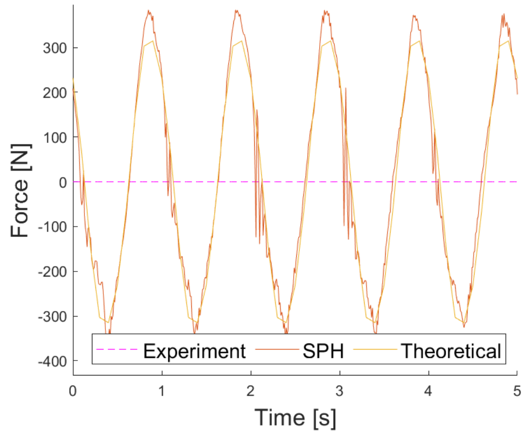

Figure D.100: r_d=200 mm, a=150 mm, f=1 Hz

D.2 Minimum draft

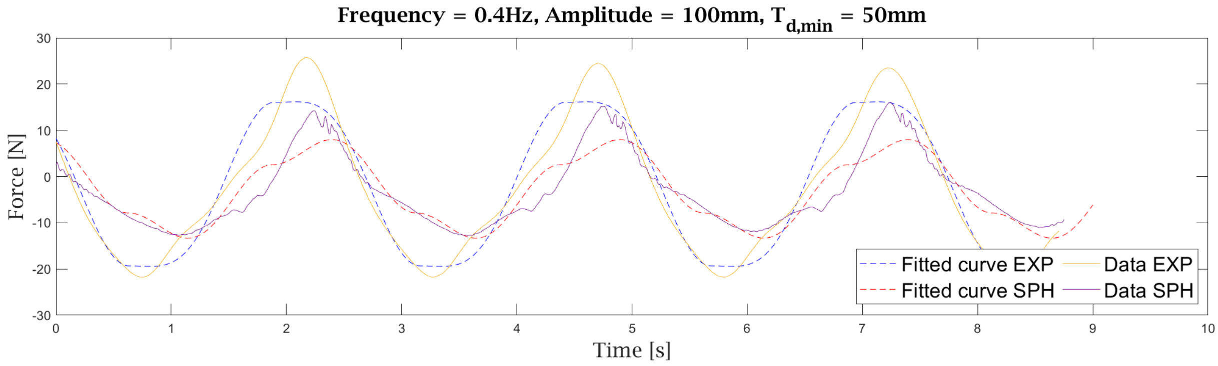

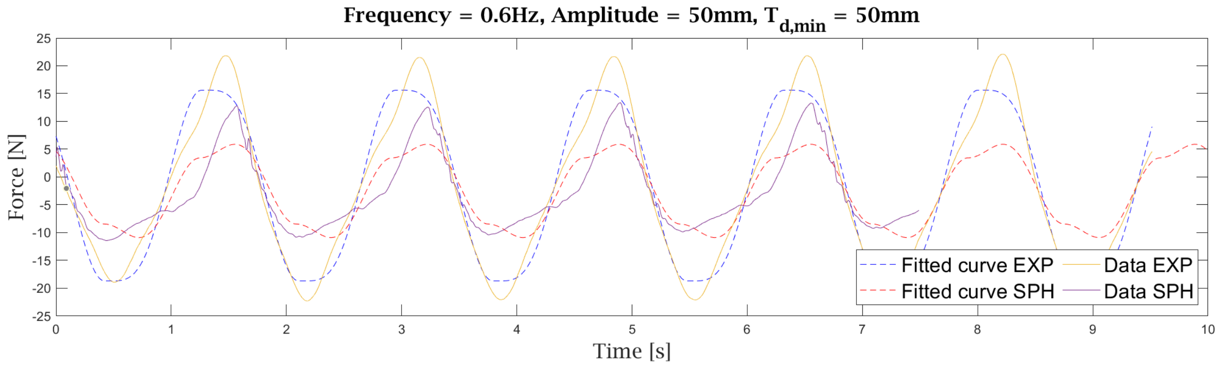

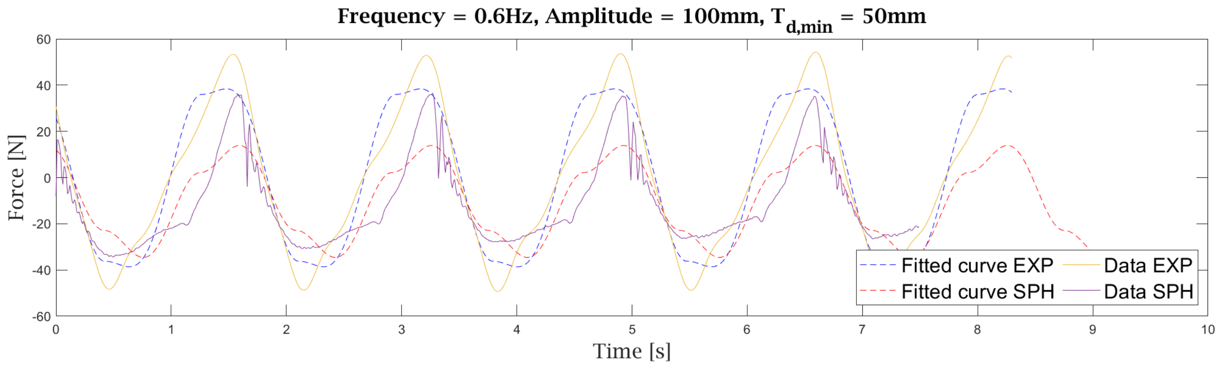

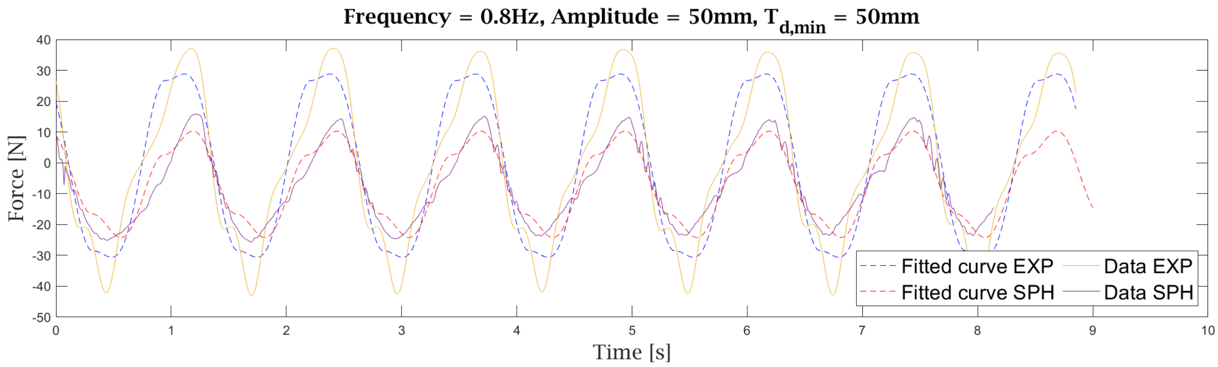

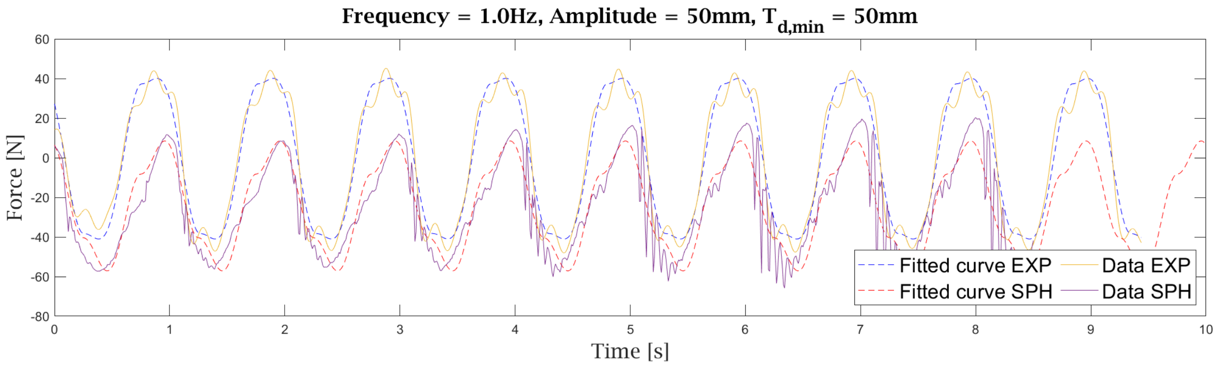
Frequency = 1.0Hz, Amplitude = 50mm, T d,min = 50mm
Force [N]
Time [s]
Fitted curve EXP
Data EXP
Fitted curve SPH
Data SPH

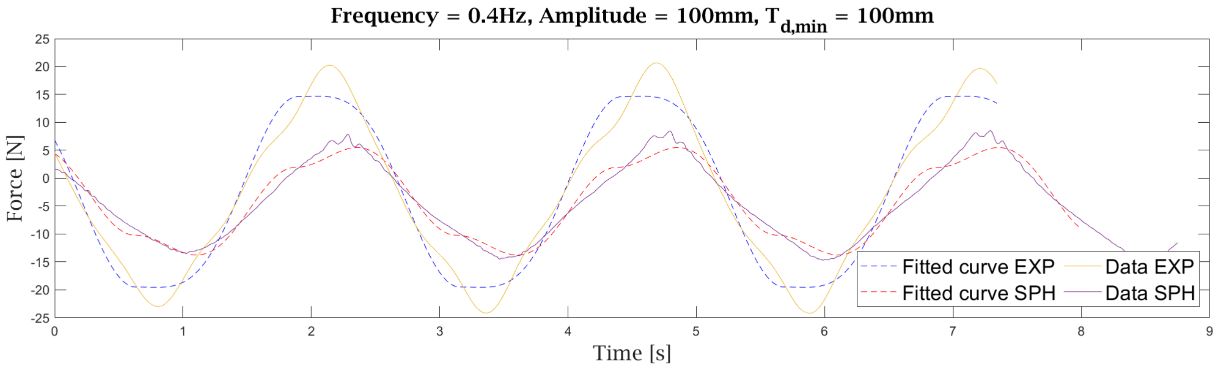
Frequency = 0.4Hz, Amplitude = 100mm, T d,min = 100mm
Force [N]
Time [s]
Fitted curve EXP
Data EXP
Fitted curve SPH
Data SPH

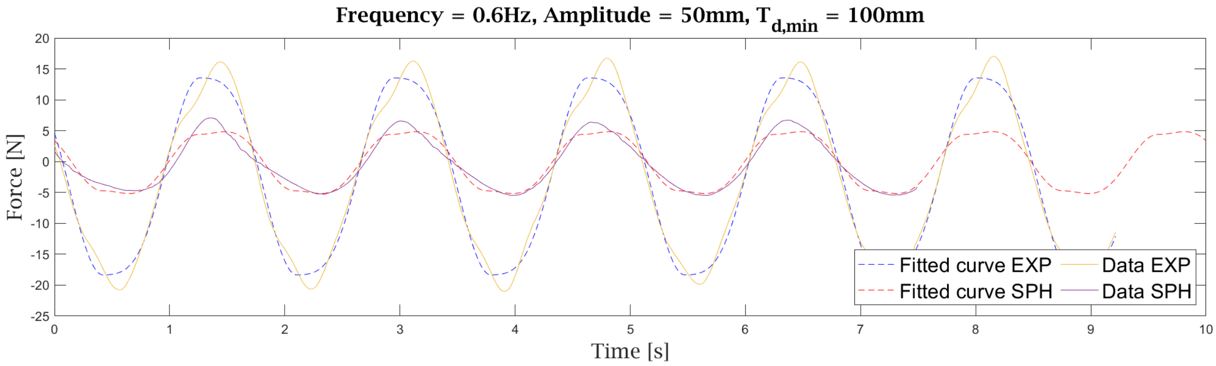
Frequency = 0.6Hz, Amplitude = 50mm, T d,min = 100mm
Force [N]
Time [s]
Fitted curve EXP
Data EXP
Fitted curve SPH
Data SPH

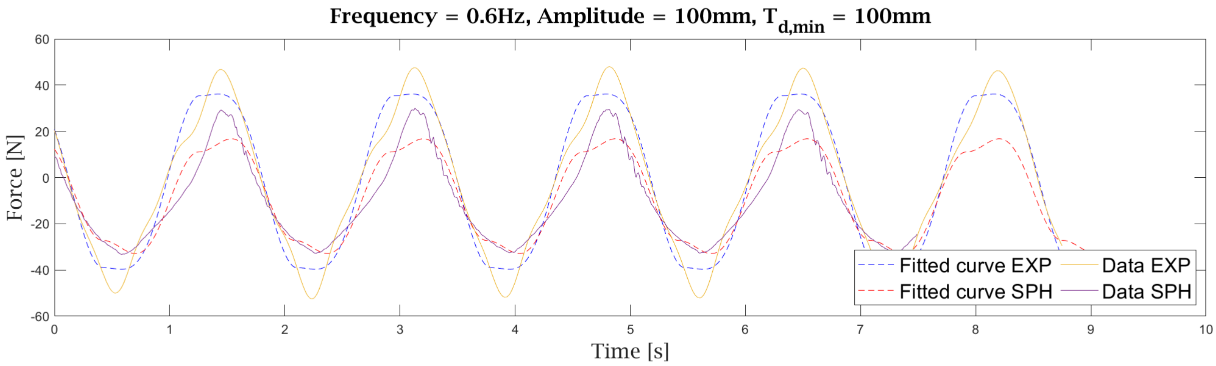
Frequency = 0.6Hz, Amplitude = 100mm, T d,min = 100mm
Force [N]
Time [s]
Fitted curve EXP
Data EXP
Fitted curve SPH
Data SPH

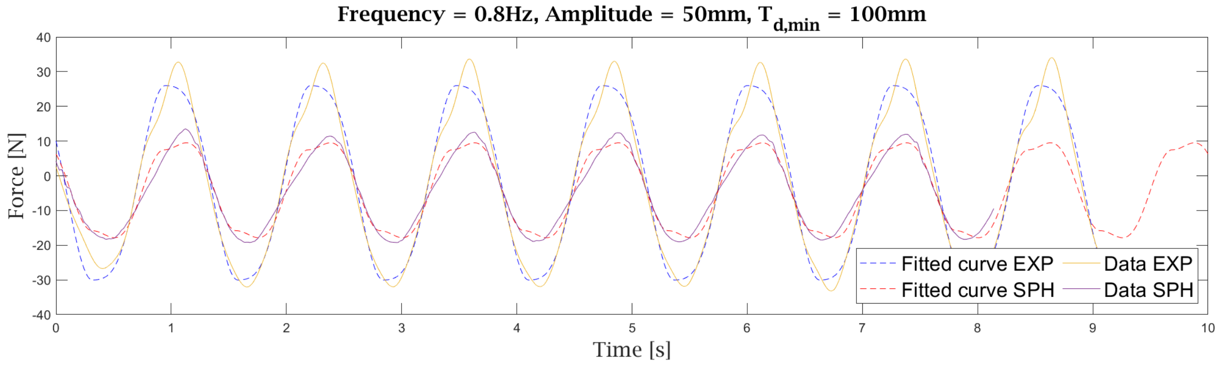
Frequency = 0.8Hz, Amplitude = 50mm, $T_{d,min}$ = 100mm
Force [N]
Time [s]
Fitted curve EXP
Data EXP
Fitted curve SPH
Data SPH

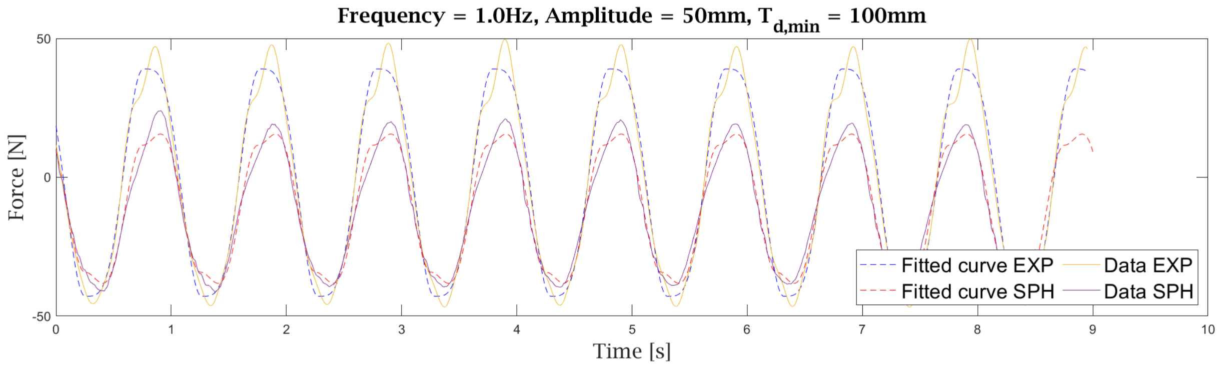
Frequency = 1.0Hz, Amplitude = 50mm, $T_{d,min}$ = 100mm
Force [N]
Time [s]
Fitted curve EXP
Data EXP
Fitted curve SPH
Data SPH

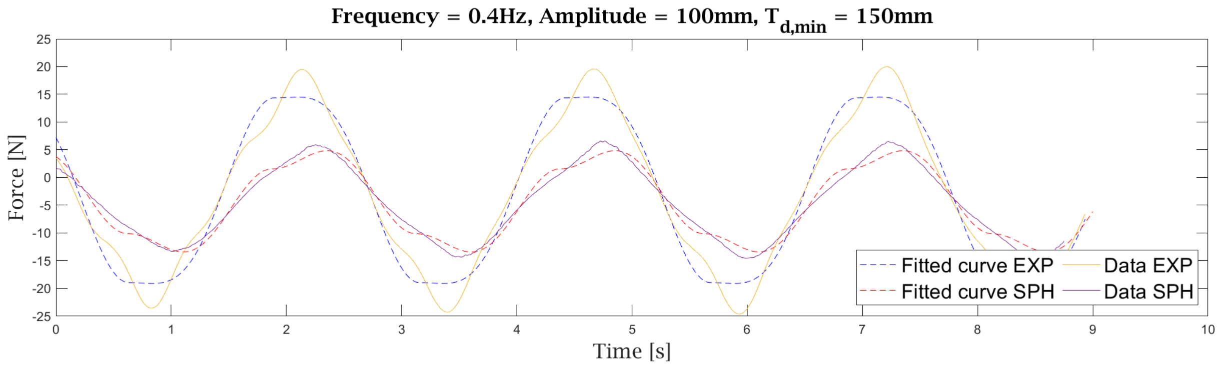
Frequency = 0.4Hz, Amplitude = 100mm, $T_{d,min}$ = 150mm
Force [N]
Time [s]
Fitted curve EXP
Data EXP
Fitted curve SPH
Data SPH

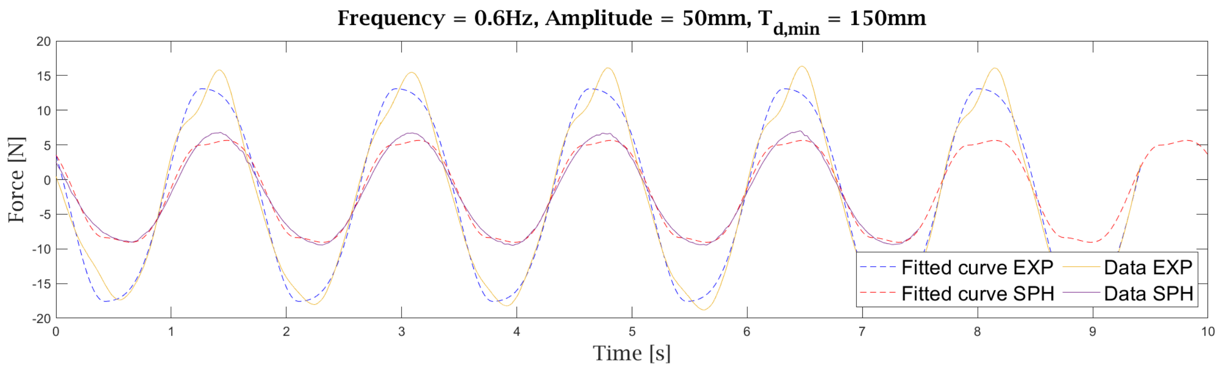
Frequency = 0.6Hz, Amplitude = 50mm, $T_{d,min}$ = 150mm
Force [N]
Time [s]
Fitted curve EXP
Data EXP
Fitted curve SPH
Data SPH

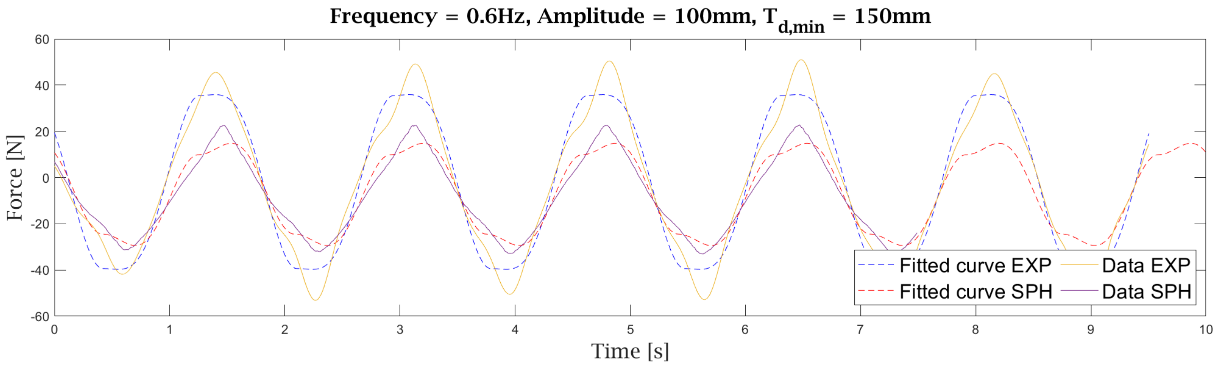
Frequency = 0.6Hz, Amplitude = 100mm, $T_{d,min}$ = 150mm
Force [N]
Time [s]
Fitted curve EXP
Data EXP
Fitted curve SPH
Data SPH

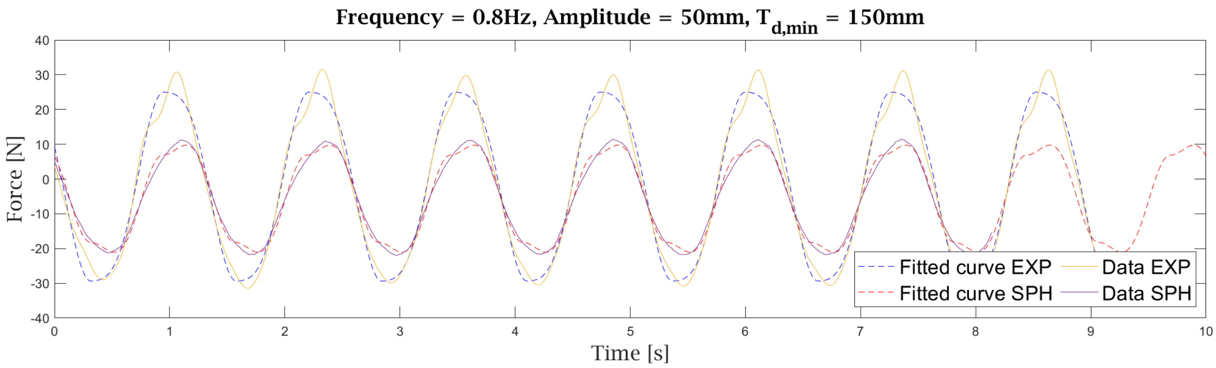
Frequency = 0.8Hz, Amplitude = 50mm, $T_{d,min}$ = 150mm
Force [N]
Time [s]
Fitted curve EXP
Data EXP
Fitted curve SPH
Data SPH

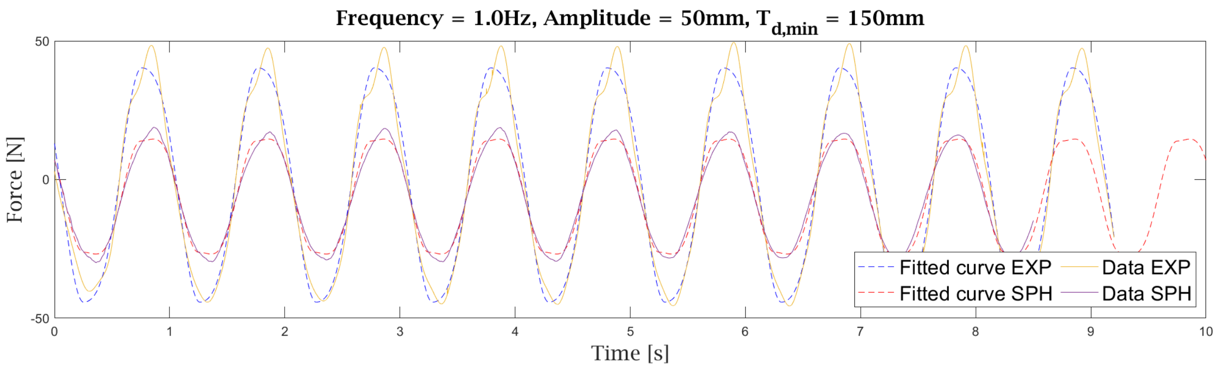
Frequency = 1.0Hz, Amplitude = 50mm, $T_{d,min}$ = 150mm
Force [N]
Time [s]
Fitted curve EXP
Data EXP
Fitted curve SPH
Data SPH